University of Catania

Department of Physics and Astronomy

QUANTUM TECHNOLOGIES WITH
SUPERCONDUCTING ARTIFICIAL ATOMS

by

Pietro Di Stefano

Supervisor: Prof. Giuseppe Falci

Referee: Prof. Luigi Amico

A thesis submitted for the degree of Doctor of
Philosophy

January 2017

ii

Acknowledgements

Abstract

In the present work, we explore possible routes to the future exploitation of quantum technologies in superconducting artificial atoms. The objectives of the thesis are twofold. On the one hand, we study advanced control of the quantum states of individual artificial atoms, tailored at robust and faithful quantum information processing in complex architectures and at the detection of the Ultra Strong Coupling regime. On the other hand, we study and propose a framework to experimentally establish quantum stochastic thermodynamics in circuit-QED.

In chapter 3, the implementation of a Lambda system in superconducting artificial atoms is discussed. Strategies for optimal design are investigated by means of optimal symmetry breaking and dynamical decoupling. Stimulated Raman Adiabatic Passage (STIRAP), an adiabatic population transfer technique in three-level system, is introduced and its transfer efficiency is shown to be $\sim 70\%$ in the Cooper Pair Box. Optimization strategies are also discussed.

In chapter 4, a novel technique for population transfer in a Lambda system is proposed, nicknamed chirped STIRAP (cSTIRAP), its key asset being the possibility of operating with an always on driving field. Robustness against parametric imperfections is assessed and specific regimes of failure due to energy level fluctuations are thoroughly examined.

A novel way to control superconducting qutrits in the Lambda system is introduced in chapter 5. It is shown that, by employing a two-photon pump, the spectrum of the devices is changed in a non-trivial way by AC Stark shifts, that can be then compensated by suitable modulation of the driving phases. A 2+1 photons STIRAP technique is introduced, with transfer efficiency $\simeq 97\%$ in last generation devices despite the presence of both low and high frequency noise.

In chapter 6, dynamical detection of the Ultra Strong Coupling (USC) regime is studied. It is shown that, by implementing a three-level Vee scheme with a flux qutrit, non classical effects and exotic light-matter interaction phenomena can be amplified and detected unambiguously.

A Circuit-QED implementation of a non-equilibrium thermodynamic experiment is finally proposed in chapter 7. A stochastic thermodynamics formalism is defined and work and heat are defined at the single quantum trajectory level. Numerical simulations are shown and the possibility to verify detailed fluctuation theorems is demonstrated. Moreover, the entropy production is defined as a witness of irreversibility and trajectory with a negative entropy production are shown, the mean entropy production being non-negative as required by the second law.

List of Publications

Published papers

- P.G. Di Stefano, E. Paladino, A. D'Arrigo, B. Spagnolo, G. Falci, Design of a Lambda configuration in artificial coherent nanostructures, *Rom. Jour. Phys.* 60:676-685, 2015.

- P.G. Di Stefano, E. Paladino, A. D'Arrigo, G. Falci, Population transfer in a Lambda system induced by detunings, *Phys. Rev. B* 91:224506 (2015)

- P.G. Di Stefano, E. Paladino, T.J. Pope, G. Falci, Coherent manipulation of highly noise-protected artificial atoms in the Lambda scheme, *Phys. Rev. A* 93:051801, 2016.

- G. Falci, P.G. Di Stefano, A. Ridolfo, A. D'Arrigo, G.S. Paraoanu, E. Paladino, Advanced control of superconducting architectures in the Lambda scheme, *Fortschr. Phys.*, 10.1002/prop201600077.

In preparation

- A. Ridolfo, P.G. Di Stefano, E. Paladino, G. Falci, Ultrastrong coupling probed by Coherent Population Transfer.

- P.G. Di Stefano, J.J. Alonso, E. Lutz, G. Falci, M. Paternostro, Non-equilibrium thermodynamics of continuously monitored quantum systems.

List of Figures

Contents

Chapter 1

Introduction

Quantum technologies have attracted much interest in the last few years, both in academia and in industry[5, 6, 7, 8], and the field is currently one of the most active in the physics community, producing large volumes of research[9]. The goal of quantum technology research is to demonstrate how harnessing genuinely quantum properties like quantum superposition, non-locality and squeezing can help to achieve certain tasks in a more efficient way. Below we give some of the numerous examples of how this is possible.

In quantum computation, quantum superposition and entanglement are employed to speed-up certain computation tasks. A universal quantum computer[10] is, in fact, capable of exponential improvements in the complexity class of certain problems. Famous examples are factorization of large numbers[11], database searching[12] and, more recently, machine learning algorithms[13, 14, 15]. In quantum simulation, the possibility of simulating efficiently a physical system of interest is studied. Quantum simulators were initially envisioned by Feynman[16]. Later works[17] demonstrated how a universal quantum computer can be used to efficiently simulate any system obeying quantum mechanics. This has applications, for example, to drug synthesis and quantum chemistry[18].

Quantum squeezing can be used to engineer finite temperature environments that promise to outperform Carnot engines[19]. Shortcuts to adiabaticity[20] allow a quantum engine to operate at full powers with an efficiency higher than the classical limit[21]. Spin squeezing can be employed to overcome the boundary imposed by Cramér Rao inequality for the uncertainty of the estimation of parameters, a result that gave rise to the field of quantum metrology[22].

Quantum technologies depend, from a theoretical perspective, on the quite straightforward requirement that the physical substrate onto which they are im-

plemented obeys the laws of quantum mechanics. In other words, they need a *quantum hardware*. Observing quantum behaviour, though, has proven to be an amazingly difficult challenge. This is due to the fact that a quantum system always interacts with a noisy environment that is responsible to the loss of its quantum properties by means of *decoherence*[23]. Advances in the field were possible only due to the fact that current technology allows us to isolate and control the quantum state of microscopic or mesoscopic systems that behave quantum mechanically. Many systems were, then, identified as a possible candidate to constitute the hardware substrate of future quantum technologies. Examples are Rydberg atoms in quantum optics[24], trapped ions[25], quantum dots[26], Nuclear Magnetic Resonance systems[27], NV centers[28], impurities in silicon[29] and superconducting artificial atoms[30].

In this thesis we will present a collection of research works related to quantum technologies in the context of superconducting artificial atoms. The latter have established in the past few years as one of the most promising frameworks for the future implementation of quantum computers. We will introduce the physics of superconducting artificial atoms in chapter 2, but, in a nutshell, they are nanoscopic devices built on a chip using common photo/electro-litographic techniques, based on superconducting materials[31, 32]. The unique properties of the superconducting phase and the Josephson junction allow for the design of devices, such as the Cooper Pair Box (see section 2.1.2) and the flux qudit (see section 2.1.3), that exhibit discrete[32] non-linear spectra and allow for the observation of several quantum effects like superposition[33] and entanglement[34]. The very fact that such devices are engineered allows for a great degree of tunability of their parameters[32], which can be achieved both at the design stage and on-chip via the use of electromagnetic knobs. Superconducting artificial are probably the most scalable technology among the ones listed above[35]. Moreover they enjoy large couplings with control fields[30] and to each other[36].

In circuit Quantum Electrodynamics (Circuit-QED) (see section 2.1.4), superconducting artificial atoms are coupled to electromagnetic resonator modes that allow for the control and measurement of their quantum state. Circuit-QED was proposed in 2004 by Blais et al.[30] as an architecture for quantum computation. Since then, several proposals have shown how the technology can be used to study, among the others, quantum simulation[37], thermodynamics[38] and beautiful quantum optics phenomena[39]. In the recent years, the possibility to successfully implement quantum error correction codes[40], a fundamental building block to build universal, scalable quantum computers[41], arose much
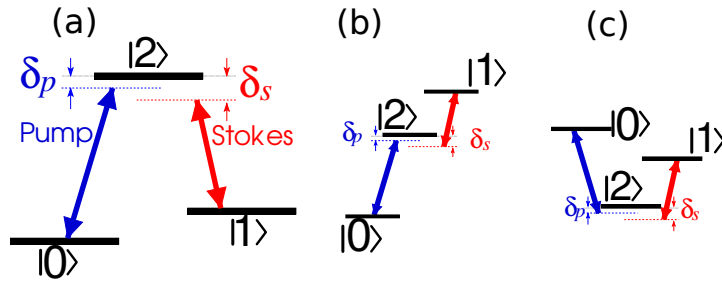
Figure 1.1: Driven three-level atoms configurations: (a) Lambda, (b) Ladder and (c) Vee schemes.

interest[42] and brought quantum computers outside the boundaries of academia.

In this theses, we will, in particular, focus on two main aspects. In the first part (chapters from 3 to 6) we study advanced quantum control techniques tailored at the manipulation of the quantum state of an artificial atom. In the second part (chapter 7) we will study the implementation of a non-equilibrium thermodynamics experiments to study irreversibility features of quantum physics at the microscopic level. Below we give an outline of the work together with its main motivation and a brief account of the current literature.

1.1 Advanced control of Quantum Systems

Complex architectures of superconducting artificial atoms are subject to fabrication imperfection. Moreover, superconducting circuits are embedded in a solid state environment that brings noise into the dynamics, both of Markovian[30] and non-Markovian[43, 44, 45, 46] nature (see section 2.2). These issues demand for control techniques that show some intrinsic robustness with respect to parameter fluctuations, such as, for example, adiabatic techniques. The latter have been shown to display a remarkable resilience to parameter variability and control pulses shaping[47], while, on the downside, being slow due to the very requirement of adiabaticity of the dynamics. This implies a greater sensitivity with respect to Markovian noise[48], although, as we shall see in chapter 5, remarkable efficiency can be obtained in present technology.

For the greater part of this thesis, we are going to focus on three-level artificial atoms (see Fig.1.1), in particular operated in the so called Lambda system, a way to drive a three-level atom with two external fields. In a nutshell, the Lambda scheme is more interesting than the other configurations of the drives (Ladder and Vee schemes) since it involves both absorption and emission of photons.

This property can be useful to achieve a number of tasks such as, among others, non-classical radiation generation[49, 50] in the microwave domain, quantum information transfer between distant, uncoupled nodes[51], holonomic quantum computation[52]. As we shall see in sections 2.1.2 and 2.1.3, though, identifying a Lambda system in superconducting artificial atoms poses a fundamental design problem, that is the trade-off between strength of the pump coupling [see Fig. 1.1(a)] and protection against noise.

This trade-off is thoroughly studied in chapter 3, where we study the implementation of a commonplace quantum optic technique to transfer population from state $|0\rangle$ to state $|1\rangle$ of a three-level atom known as Stimulated Raman Adiabatic Passage (STIRAP). STIRAP relies on quantum interference and adiabaticity to trap the system in a *dark state* that has no component along the excited state $|2\rangle$ in spite of how the fields trigger transitions in the Lambda configuration. STIRAP does so through the application of a Stokes and a pump field in a counterintuitive sequence, i.e. the Stokes preceding the pump and has been shown to have a remarkable resilience with respect to parametric fluctuations[53, 54, 47]. After reviewing STIRAP, in chapter 3 we study the application of STIRAP to the quantronium, i.e. a class of superconducting artificial atoms based on the Cooper Pair Box (see section 2.1.2). We study the transfer efficiency of STIRAP under the effect of Broad Band Colored Noise (BBCN), responsible of both markovian and non-markovian decoherence and address the optimization of STIRAP using two different strategies, namely optimal symmetry breaking and dynamical decoupling. We show how a $\sim 70\%$ efficiency can be obtained with the quantronium.

In chapter 4, we propose a novel technique for adiabatic population transfer in three-level atoms. The main difference with respect to STIRAP is in the knobs we used: while in STIRAP one is allowed to employ time modulation of the amplitude of the external fields, our technique, which we nicknamed *chirped* STIRAP or cSTIRAP, works on the constraint that of the fields is kept always-on. The desired population transfer is then attained by properly modulating the phases of the field, i.e. the detunings. The main motivation behind this idea is given by circuit-QED architectures. In circuit-QED, in fact, artificial atoms are coupled with resonator modes through capacitors with coupling constants that are hard or impossible to make time-dependent. The always-on field is, therefore, intended to mimic this coupling to achieve an effective interplay between the artificial atom and the non-classical state of the resonator[1] such as generation of Fock states of radiation[49, 50] or of mechanical motion[55, 56]. We show how,

---

[1]This is detailed in Ref. [57].

despite cSTIRAP relies on an approximate rather than exact dark state, it is remarkably resilient to parameter fluctuations and allows almost unit efficiency.

In chapter 5, we study yet another way to overcome the large coupling vs noise protection trade-off in the implementation of a Lambda system with artificial atoms. We propose how a Lambda system can be effectively implemented by resorting to a two-photon pump. Although this particular kind of control scheme produces, as we shall see, unwanted Stark shifts in the atomic spectrum, this drawback can be easily overcome by introducing phase modulation, which is doable in present day technology[58]. We simulate the 2+1 STIRAP protocol in two kind of artificial atoms, namely a transmon and a flux qutrit, using parameters borrowed from the literature and show that nearly unit efficiency can be attained in spite of both high and low frequency noise acting on the devices.

In chapter 6 we show how the Ultra Strong Coupling (USC) regime can be probed by STIRAP. In the USC regime, see section 2.1.4, the ground state of the resonator-artificial atom system has a two-photon component. Our proposal is to coherently amplify such a component to generate a two-photon Fock state in the cavity and it can be used to efficiently detect USC, as opposed to current techniques based on the detection of the Bloch-Siegert shift[4]. This dynamical technique will move one step beyond coherent control, besides complementing standard saturation spectroscopy techniques aimed at the detection of the Bloch-Siegert shift. We will discuss coherently amplified USC detection in state of the art quantum hardware, proposing that it could be observed in flux-type superconducting artificial atoms driven in the Vee scheme.

1.2 Non-equilibrium Thermodynamics at the Quantum Scale

Much effort has been put recently by the scientific community in the quest for a deeper understanding of the laws of thermodynamics at the quantum scale. Quantum thermodynamics is, in particular, characterized by the fact that is allows both thermal and quantum fluctuations[59, 60]. A fundamental question yet to be answered is how could irreversibility and the arrow of time arise from a time-symmetric theory[61]. Answering this question would resolve long standing puzzles as the thermalisation[62] of small systems. More importantly, understanding thermodynamic theory at the fundamental level could pave the way towards the design and construction of quantum heat engines[63].

A very important achievement has been the extension of seminal results of clas-

sical stochastic thermodynamics[64] to the quantum realm. Specifically, quantum versions fluctuation theorems[65, 66] have been derived allowing a description of non-equilibrium thermodynamics beyond the linear response theory. Fluctuation theorems relate non-equilibrium quantities such as work to equilibrium properties of the working media, such as the free energy difference. Very important examples are the Jarzynski equality, that relates the non-equilibrium average exponentiated work to the free energy difference thereby entailing the second law of thermodynamics for closed systems, and Crooks detailed fluctuation theorem. Central fluctuation theorems have also been proposed for different quantum maps[67, 68, 69] and the entropy production has been defined at the quantum level[70, 71].

In spite of tremendous theoretical effort, we currently have very few experiments[71]. This is because the verification of fluctuation theorems requires the use of projective measurements, that are experimentally demanding. In chapter 7 we study the verification of fluctuation theorems for a continuously monitored superconducting artificial atom. Continuously monitoring, as opposed to projective measurements, is easier to implement in circuit-QED architecture. In particular, we show how detailed fluctuation theorems can be verified and the entropy production, as a witness of irreversibility, can be properly defined and measured. Interestingly, we will show that along particular quantum trajectories it is possible to observe *negative* values for the entropy production, the mean entropy production always being non-negative as required by the second law.

Chapter 2

Superconducting Artificial Atoms: Basic Concepts

In this chapter we will briefly describe the physics of superconducting artificial atoms. Such devices are made of superconducting materials printed in solid state chips making use of state of the art photo/electro-litographic technology[31, 32]. The name artificial atoms is due to the fact that they exhibit quantum properties such as discrete, non-linear spectra in the microwave $\sim 1 \div 10 \text{GHz}$ range and coherence. The fact that superconducting artificial atoms can be engineered and whose properties can be tuned both at project stage and on-chip via electromagnetic signals, makes them very promising candidates for the exploitation of future quantum technologies.

2.1 Superconducting circuits

A superconducting circuit can be modelled as an electrical circuit in the lumped elements approximation. Assuming that, below the superconducting critical temperature the resistance of the circuit is zero, its components will be reactive elements, i.e. capacitors and inductors, and Josephson junctions. The Josephson junction[72] is a superconductor-insulator-superconductor junction where the thickness of the insulator layer is $\sim$ nm. Its voltage-current characteristic is given by the Josephson equations. The current produced by the Cooper pairs tunnelling through the junction is called *Josephson current*. If we call V the voltage across the junction and I the Josephson current we have:

$$V(t) = \frac{\hbar}{2e} \frac{\partial \phi(t)}{\partial t}; \quad I(t) = I_c \sin\phi(t) \tag{2.1}$$

Where I_c is the *critical current* and $\phi(t)$ is the difference of the Ginzburg-Landau wavefunction between the two superconducting leads of the junction. Defining the magnetic flux of the junction as $\Phi(t) := \Phi_0 \, \phi(t)/2\pi$, $\Phi_0 := h/2e$ being the quantum of magnetic flux, we see that the Josephson junction has a current-flux characteristic, that qualifies it as a non-linear inductor. The energy of the Josephson junction can be written as:

$$U_J(t) = \int_{-\infty}^{t} dt' \, V(t)I(t) = E_J(1 - \cos \phi(t)) \tag{2.2}$$

Where we defined the Josephson energy $E_J := \hbar/2eI_c$. Since the Josephson junction is a metal-insulator-metal junction, every physical realization of the latter has a parallel parasitic capacitance.

2.1.1   Lagrangian formulation of circuit theory and canonical quantization

A lumped-elements circuit can be formally described as a graph made of a set of nodes and a set of branches, each branch containing a lumped reactive element. The Lagrangian theory of electrical theories is conveniently expressed in terms of node fluxes and charges.

Formally, the Lagrangian of the system is a function node fluxes and their derivatives, i.e. $L = L(\boldsymbol{\Phi}, \dot{\boldsymbol{\Phi}})$. In particular, as we detail in appendix A, it is found to be the difference between the electrostatic energy stored in the capacitors and the magnetic energy in the inductors. The variables canonically conjugate to the nodes fluxes, i.e. the *generalized momenta*, are $\boldsymbol{q} := \partial/\partial\dot{\boldsymbol{\Phi}} \, L(\boldsymbol{\Phi}, \dot{\boldsymbol{\Phi}})$. The Hamiltonian of the circuit is found by Legendre transforming $H(\boldsymbol{\Phi}, \boldsymbol{q}) = \dot{\boldsymbol{\Phi}} \cdot \boldsymbol{q} - L(\boldsymbol{\Phi}, \dot{\boldsymbol{\Phi}})$. The quantum Hamiltonian is found by replacing generalized coordinates and momenta with their operatorial counterparts, i.e. $\boldsymbol{\Phi} \to \hat{\boldsymbol{\Phi}}$ and $\boldsymbol{q} \to \hat{\boldsymbol{q}}$, and imposing the canonical conjugation relations $[\hat{\Phi}_i, \hat{q}_j] = \delta_{ij}\hbar i$. Below we going to describe two types of superconducting artificial atoms, namely the Cooper pair box and the flux qudit. Their circuit schematics are shown in Fig.2.1 and 2.5. From now on, unless otherwise specified, we will work in $\hbar$ units by imposing $\hbar = 1$.
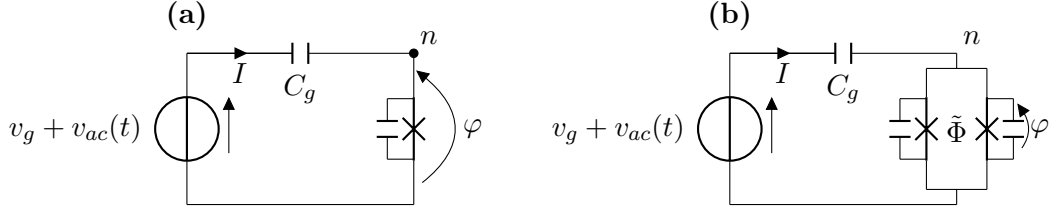
Figure 2.1: Circuit schematics for the Cooper pair box. (a) Single and (b) double junction architectures. $\tilde{\Phi}$ here is the external magnetic flux applied to the SQUID loop

2.1.2 The Cooper Pair Box

The Cooper pair box is a device composed by a superconducting loop broken by a Josephson junction and a capacitance [see Fig.2.1(a)]. In most implementations, the single junction is substituted by a parallel of two identical junctions with Josephson energy E_J, i.e. a SQUID loop. The SQUID is equivalent to a single tunable junction with Josephson energy $E_{J|eq} = E_J \cos \tilde{\Phi}/\Phi_0$ [see Fig. 2.1(b)] and twice the capacitance of the single junctions. The two architectures of Fig. 2.1 can, therefore, be formally treated on the same footing and we will refer to the single junction one for simplicity.

The superconducting region or *island* between the capacitance and the junction was, in the early implementations of such devices, used to store single cooper pairs whose presence or absence was encoded as a logical state. The circuit has a single node in correspondence with the island, hence it's Hamiltonian is given by

$$H_{CPB} = 4E_C(\hat{n} - q_g)^2 - E_J \cos \hat{\phi} \tag{2.3}$$

where we used the number of Cooper pairs in the island $\hat{n} := \hat{q}/2e$ and the phase difference across the junction $\hat{\phi} := 2e\hat{\Phi}$. Moreover we defined the Charging energy relative to the total capacitance $E_C := C_{\text{tot}}v_g/2e$, with $C_{\text{tot}} := C + C_g$ and the residual charge $q_g = C_{\text{tot}}v_g/2e$. The Cooper pair number operator has clearly a discrete spectrum, hence we can define its eigenstates by $\hat{n} := \sum_k k |k\rangle \langle k|$. The canonical conjugation relation $[\hat{\phi}, \hat{n}] = i$ implies that[73] we can regard the phase as a generator of translations in the number space, i.e. $e^{-i\hat{\phi}} |n\rangle = |n+1\rangle$. Writing the Hamiltonian in the discrete basis of the number operator yields

$$H_{CPB} = 4E_C \sum_n (n - q_g)^2 |n\rangle \langle n| - E_J \sum_n (|n\rangle \langle n+1| + |n+1\rangle \langle n|) \tag{2.4}$$

Written in this form, H_{CPB} is easily tractable and amenable to numerical diagonalization.

Control of the device is attained through superimposition of a small AC signal $\mathcal{A}(t)$ to the bias q_g. In general, quantum control can be formalized as a coupling to the external field through an electrical dipole-like operator $\mathcal{Q}$ of the system. The general Hamiltonian for a driven artificial atom is therefore

$$H = H_0 + \mathcal{Q}\,\mathcal{A}(t) \tag{2.5}$$

where H_0 is the bare Hamiltonian. By expanding Eq. 2.3 and dropping non operator terms we get the expression for the driven Hamiltonian of the Cooper pair box where $\mathcal{Q} = -8E_C\hat{n}$.

The properties Hamiltonian of the Cooper pair box can be drastically changed by tuning values of q_g and the ratio E_J/E_C. Semi-integer values of the residual charge q_g are particularly interesting. Since $H_{CPB}(q_g)$ is periodic with period one, we will only consider the $[0,1]$ interval. The particular choice $q_g = 0.5$ is referred to in the literature as *symmetry point* or *sweet spot*. At the symmetry point, a parity symmetry to set in; in particular, $H_{CPB}(q_g = 0.5)$ is symmetric with respect to the charge-parity operator $\mathcal{P}_n = \sum_m |1 - m\rangle\langle m|$. This implies that eigenstates $|\phi_n\rangle$ of H_{CPB} will have a definite parity symmetry $\mathcal{P}_n |\phi_j\rangle = (-1)^j |\phi_j\rangle$. Since the dipole-like operator $\mathcal{Q}$ has an odd symmetry with respect to $\mathcal{P}_n$, it won't couple states with the same parity, i.e.

$$\mathcal{Q}_{ij} := \langle\phi_i|\mathcal{Q}|\phi_j\rangle \propto 1 - (-1)^{i+j} \tag{2.6}$$

We plot the behaviour of $\mathcal{Q}_{ij}$ vs q_g in Fig. 2.1.2 (a), where we definitely see how $\mathcal{Q}_{02}$ vanishes at the sweet spot. This means that the transition between the ground and the second excited state cannot be addressed, hence the impossibility of designing a Lambda system at the symmetry point. We address this issue in chapters 3 and 5.

If, on the one hand, biasing the CPB at the sweet spot limits available control, on the other it enforces protection against charge noise. Fig. 2.1.2 (b) shows the spectrum of the CPB against q_g. It is seen that the sweet spot is a stationary point for the energy levels. This, in turn, means that variations in energy due to small, unwanted fluctuations δq_g of q_g caused by *charge noise* only add quadratically in δq_g. This is why charge noise, the dominant source of noise in the CPB[32, 48], is suppressed at the sweet spot. We are going to address this point in greater details in chapter 3.
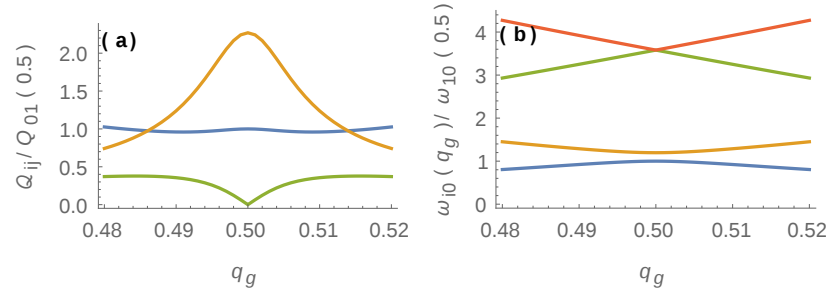
Figure 2.2: Behaviour of the CPB vs q_g. Simulations have been carried out by cutting the number of charge states to $n_{max} = 100$. (a) Couplings $\mathcal{Q}_{01}$ (blue), $\mathcal{Q}_{12}$ (orange) and $\mathcal{Q}_{02}$ (green) vs q_g in units of $\mathcal{Q}$ evaluated at the sweet spot. (b) Spectrum of the device emphasizing the parity symmetry at the sweet spot.
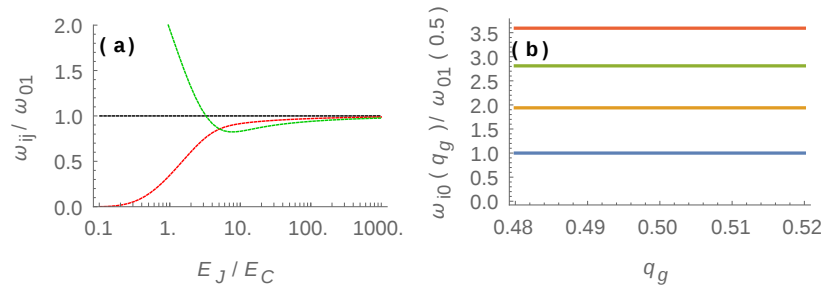
Figure 2.3: (a) Bohr frequencies ω_{01} (black), ω_{12} (red) and ω_{23} (green) of the CPB vs E_J/E_C. (b) Spectrum of the transmon ($E_J/E_C = 50$) emphasizing the harmonicity of the device.

The ratio E_J/E_C can be tuned, up to a certain limit, electromagnetically by applying an electromagnetic field to the SQUID loop of Fig. 2.1(b). This enables, for example, tasks such as time-dependent modulation of detunings (see chapters 4, 5, 7) between the artificial atom and external fields. More importantly, hardware engineering of the the E_J/E_C has led, over the year, to drastically different implementations of the CPB ranging from the *charge qubit* ($E_J/E_C \ll$ 1), where the first eigenstates of the Hamiltonian are almost parallel with charge eigenstates, to the *quantronium* ($E_J/E_C \sim 1$) and the *transmon* ($E_J/E_C \gg 1$). The reduction of the charging energy in the transmon is achieved by using a big shunt capacitor C_g[74]. This has two main effects: on the one hand, charge noise is drastically reduced by reducing E_C; on the other hand reducing the ratio of the kinetic ($\sim E_C$) to the potential ($\sim E_J$) has the unwanted effect of reducing the anharmonicity of the spectrum of the CPB. This can be seen by an analogy. A particle moving with a small kinetic energy in a cosine shaped potential will "see" value of the potential only in the proximity of a minimum, where the cosine potential is quasi-harmonic. In Fig. 2.1.2 (a) we plot the spectrum of the CPB vs E_J/E_C. In particular, defining ϵ_j as the j-th eigenenergy, we plot the splittings $\omega_{01}, \omega_{12}, \omega_{13}$ (see caption) , where we defined the Bohr frequencies $\omega_{ij} := \epsilon_j - \epsilon_i$. In fig. 2.1.2 the spectrum of a transmon with $E_J/E_C = 50$ is plotted is vs q_g.

As a consequence of the quasi-harmonicity of the spectrum, selectively addressing specific transition in the transmon is tricky and can be done only if the coupling with the control field is small enough[74]. A consequence of this is that gate times in the transmon are usually longer than in the charge or the flux qubit. We will see a consequence of this in chapter 5. On the other hand, though, reduction of the charging energy dramatically reduces the detrimental influence of charge noise, making the transmon a much more reliable quantum device and one of the most promising candidates for future large scales quantum computers[3, 75] implementing fault tolerant hardware by quantum error correction[40, 42]. Decoherence times in state of the art transmons are $\sim 100\mu$s[3], incommensurably bigger than the values earliest implementations of the CPB (~ 100ns). Since the transmon effectively approximates an harmonic oscillator with increasing E_J/E_C values, as well dipole operator $\mathcal{Q} \propto n$ will approximate the momentum quadrature at large E_J/E_C. In turn this means that $\mathcal{Q}$ will become more and more close to a ladder-climbing operator, with non ladder matrix elements such as $\mathcal{Q}_{02}$ vanishing as E_J/E_C increases. We show this behavior in Fig. 2.1.2.
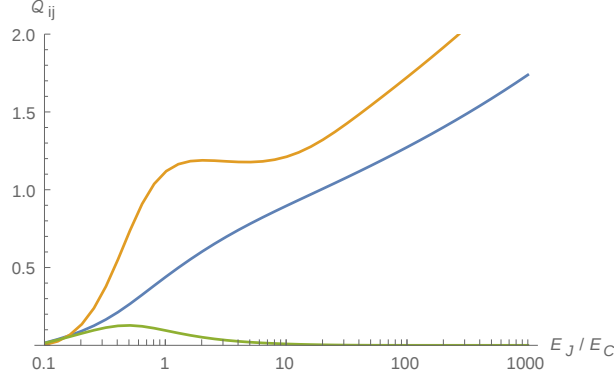
Figure 2.4: Couplings $\mathcal{Q}_{01}$ (blue), $\mathcal{Q}_{12}$ (orange) and $\mathcal{Q}_{02}$ (green) for a CPB with $q_g = 0.48$ in arbitrary units. The plot shows how the $\mathcal{Q}_{02}$ coupling is effectively suppressed in the transmon regime $E_J/E_C \gg 1$.
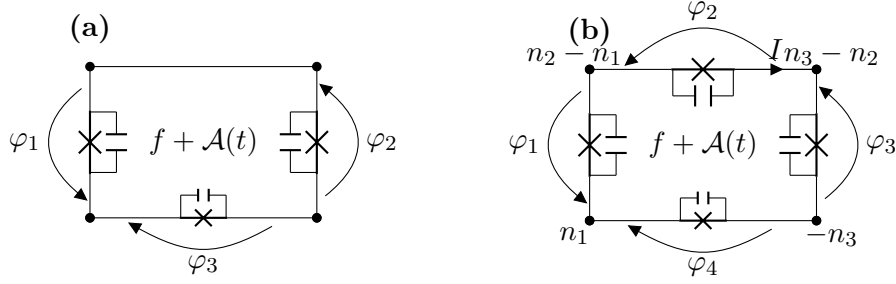
Figure 2.5: Circuit schematics for the persistent current flux qubit. (a) Three junctions architecture and (b) four junctions architecture.

2.1.3 The Flux qubit

Schematics of the flux qudit are shown in fig. 2.5. We will in particular refer to the so called *persistent current* flux qubit, introduced in Refs.[76, 77]. It is made of a loop of either three [Fig. 2.5 (a)] or four [Fig. 2.5] Josephson junctions[2, 78], one of which is smaller than the others by a factor α. Although this implementation was originally introduced in the three junctions version, we will from now on refer to the four junctions loop since it has proved to be much more resilient with respect to low-frequency noise[2].

The Hamiltonian of the device can be written in terms of the node variables as outlined at the beginning of the section, but we prefer here to pass to the *branch* variables [See Fig. 2.5(b)] via a canonical transformation that yields the
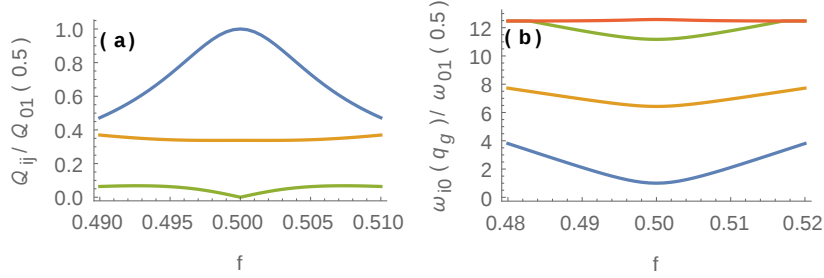
Figure 2.6: Behaviour of the flux qubit against the reduced flux f. (a) Couplings $\mathcal{Q}_{01}$ (blue), $\mathcal{Q}_12$ (orange) and $\mathcal{Q}_{02}$ (green) vs f in units of $\mathcal{Q}$ evaluated at the sweet spot. (b) Spectrum of the device emphasizing the parity symmetry at the sweet spot.

Hamiltonian

$$H_F = - E_J \sum_j^3 \cos \hat{\varphi}_j - \alpha E_J \cos \Big\{ \sum_j^3 \hat{\varphi}_j - 2\pi[f + \mathcal{A}(t)] \Big\} +$$
$$4\frac{E_C}{1+3\alpha} \Big[(1+2\alpha) \sum_j^3 \hat{n}_i^2 - 2\alpha \sum_{i \neq j}^3 \hat{n}_i \hat{n}_j \Big]$$
(2.7)

where the charging energy is given by $E_C := e^2/2C$ and we used the reduced flux $f := \Phi_b/\Phi_0$ [see Fig. 2.5(b)]. Control is performed by superimposing to the external flux bias f an AC signal $\mathcal{A}(t)$. By first order expansion of Eq. (2.7) we see that the dipole-like operator for the flux qubit [see Eq.(2.5)] is $\mathcal{Q} = 2\pi\alpha E_J \sin\left(\sum_j^3 \hat{\varphi}_j - 2\pi f \right) = 2\pi E_J \hat{I}/I_c$, where we defined the loop current operator $\hat{I}$.

In analogy with the CPB case, the flux qubit has a sweet spot at $f = 0.5$. At the sweet spot, the system enjoys a symmetry with respect to the parity operator $\mathcal{P}_\varphi \; : \; \mathcal{P}_\varphi |\varphi\rangle = |-\varphi\rangle$, where we defined the vector $\varphi := (\varphi_1, \varphi_2, \varphi_3)$. As a consequence, eigenfunctions $|n\rangle$ of H_0 can be chosen with a definite symmetry, i.e. $\psi_n(-\varphi) = (-1)^n \psi_n(\varphi)$, where n labels eigenenergies in increasing order, implying the selection rule Eq. (2.6) for the odd-parity coupling operator $\mathcal{Q}$ [see Fig. 2.1.3(a)].

Biasing the device at the sweet spot also implies enforcing protection with respect to fluctuations of the magnetic flux. Since flux noise is the dominant source of noise, flux qudits are usually biased at the symmetry point.
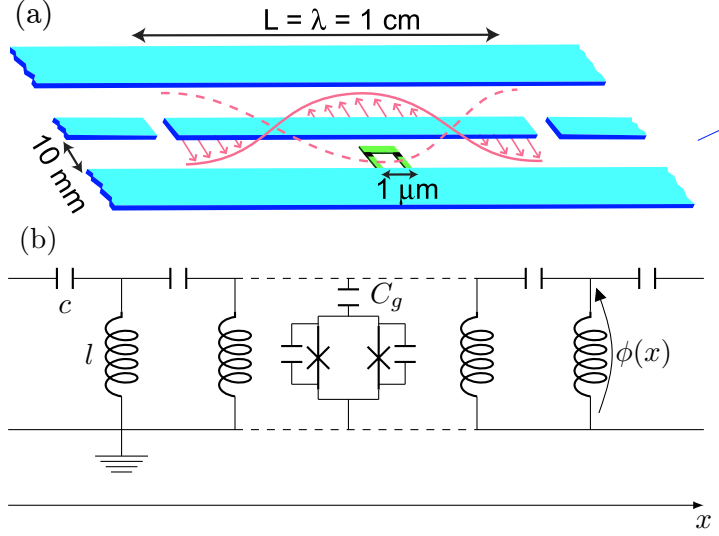
Figure 2.7: Circuit QED architecture. (a) Cartoon of a 1D Circuit-QED printed circuit. The stripline resonator is coupled capacitively to che Cooper Pair Box. (b) Circuit scheme of the Circuit-QED scheme. The resonator is modelled as a transmission line of capacitance and inductance per unit length c and l respectively. The CPB is usually placed in the middle ($x = L/2$), where the mode $k = 2$ has an antinode.

2.1.4 Circuit QED: control and measurement

Circuit Quantum Electrodynamics (Circuit-QED) was introduced in Ref. [30] as a scalable architecture for quantum computation involving superconducting qubits (especially of the CPB family) and microwave transmission line [see Fig. 2.7(a)] or a 3D cavity. The latter has the function of enabling control, quantum non-demolition measurement and to serve as a quantum bus for effectively couple[79] and entangle[80, 51, 81] multiple qubits.

The quantum Hamiltonian of the transmission line is derived below, where we will see how it can be treated as a collection of harmonic modes. We assume the architecture is effectively 1D (see Fig. 2.7) and has length L and neglect, for the time being, the presence of the CPB. Calling c the unit length capacitance and l the unit length inductance [Fig. 2.7(b)] and using the methods of appendix A, we write the classical Lagrangian of the system in term of the magnetic flux field $\phi(x, t)$ as

$$\mathcal{L}_R(\phi, \partial_\mu \phi) = \frac{1}{2} \int_{-\frac{L}{2}}^{\frac{L}{2}} dx \, \left[c(\dot{\phi}^2) - \frac{1}{l}(\frac{\partial}{\partial x}\phi)^2 \right] \qquad (2.8)$$

whose Euler-Lagrange equation is a wave equation with velocity $v = \sqrt{1/lc}$. Due

to charge neutrality[30], the boundary conditions will be $\phi(-L/2, t) = \phi(L/2, t)$. We can then write a solution in the form

$$\phi(x,t) = \sqrt{2} \sum_{k \text{ odd}} \phi_k(t) \cos\left(\frac{k\pi x}{L}\right) + \sqrt{2} \sum_{k \text{ even}} \phi_k(t) \sin\left(\frac{k\pi x}{L}\right) \qquad (2.9)$$

substituting which in Eq. (2.8) gives

$$\mathcal{L}_R = \frac{1}{2} L \sum_k \left[c\, (\dot{\phi}_k)^2 - \frac{1}{l}\, \left(\phi_k \frac{\pi k}{L}\right)^2 \right] \qquad (2.10)$$

By introducing the variable canonically conjugated to ϕ_k as $q_k = c\, L/2\, \dot{\phi}_k$ we may write the Hamiltonian of the resonator as

$$H_R = \frac{1}{2C_{eq}} \sum q_k^2 + \frac{1}{2L_{eq}} \sum_k (\pi k)^2\, \phi_k^2 \qquad (2.11)$$

where we defined the equivalent inductance $L_{eq} := l\, L$ and capacitance $C_{eq} := c\, L$. The quantum Hamiltonian is found by substituting the canonically conjugated variables with quantum operators satisfying the canonical commutation relations $[\hat{\phi}_k, \hat{q}_{k'}] = i\delta_{kk'}$, $[\hat{\phi}_k, \hat{\phi}_{k'}] = [\hat{q}_k, \hat{q}_{k'}] = 0$. By defining the bosonic operators[1]

$$a_k := \sqrt{\frac{\pi k l}{2\hbar c}} \left(\hat{\phi}_k + i\frac{c}{\pi k l}\hat{q}_k \right) \qquad (2.12)$$

and writing the canonically conjugated operators as $\hat{\phi}_k = \sqrt{\frac{c}{2\pi k l}}(a_k + a_k^\dagger)$ and $\hat{q}_k = -i\sqrt{\frac{c}{2\pi k l}}(a_k - a_k^\dagger)$ we can write the Hamiltonian as a collection of harmonic modes, i.e.

$$H_R = \sum_k \omega_k \left(a_k^\dagger a_k + \frac{1}{2} \right) \qquad (2.13)$$

where the mode frequencies are $\omega_k := k\pi v/L$. Voltage in the resonator can be written as

$$V(x) := v\frac{\partial\phi(x)}{\partial_x} =$$

$$= -\sum_{k \text{ odd}} \sqrt{\frac{\omega_k}{C_{eq}}} \cos\left(\frac{k\pi x}{L}\right)(a_k + a_k^\dagger) + \qquad (2.14)$$

$$+ \sum_{k \text{ even}} \sqrt{\frac{\omega_k}{C_{eq}}} \sin\left(\frac{k\pi x}{L}\right)(a_k + a_k^\dagger)$$

---

[1]Notice that here and from now on, when dealing with operators, we will drop the hat symbol whenever we think it does not generate confusion.

In the Circuit-QED implementation, voltage couples to the cooper pair box through the gate capacitance C_g as described in section 2.1.2. The Bias parameter q_g can be set by superimposing a DC voltage. The superconducting artificial atom and the resonator are designed in such a way that only one mode of the resonator couples with the relevant transition frequencies of the artificial atom. One usually [30] chooses the $k = 2$ mode and, in order to maximize the coupling, the artificial atom is usually built at the center of the resonator ($x = L/2$), where the voltage has an antinode $V(0) = V_{\text{rms}}(a + a^\dagger)$, where we defined $V_{\text{rms}} := \sqrt{\frac{\hbar\omega_c}{C_{eq}}}$, $a := a_2$ and $\omega_c := \omega_2$. Performing the single mode approximation, the Hamiltonian for the undriven circuit QED system reads

$$H = H_R + H_{CPB} + H_{Int} \qquad (2.15)$$

where the interaction Hamiltonian is given by

$$H_{Int} := V_{\text{rms}}(a + a^\dagger) \qquad (2.16)$$

We will now assume that the cavity mode is only coupled to the $0 \rightarrow 1$ transition of the artificial atom, i.e. the cavity frequency is $\omega_c \simeq \omega_{01}$. At the sweet spot $q_g = 0.5$, the dipole operator can be then approximated as $\mathcal{Q} = \mathcal{Q}_{01} |\phi_0\rangle \langle\phi_1| + \text{h.c.}$, where we used the eigenstates $|\phi_k\rangle$ of the CPB labelled in ascending order with respect to their energy.

$$H_{Int} = g \, (a + a^\dagger) \, (\sigma_+ + \sigma_-) \qquad (2.17)$$

where we used the atomic ladder operators $\sigma_+ = |\phi_1\rangle \langle\phi_0|$ and $\sigma_- := \sigma_+^\dagger$, and the coupling constant $g := \mathcal{Q}_{01} V_{\text{rms}}$. We will also assume that the resonator is driven by an external single tone AC field at frequency $\omega \sim \omega_c, \omega_{01}$, that can be written as a displacement term as follows

$$H = H_R + H_{CPB} + H_{Int} + \epsilon(t) \, (e^{i\omega t}a^\dagger + e^{-i\omega t}a) \qquad (2.18)$$

where we performed the Rotating Wave Approximation (RWA) by dropping the counterrotating terms of the external field[82] and defined the external field amplitude $\epsilon(t)$. We notice that, given the linearity of the Hamiltonian, extensions to cases with multi-tone external fields (as in the case of the Stimulated Raman Adiabatic Passage, see section 3.2) and/or with the resonator mode coupled to more than one transition are straightforward, but we won't account for them for

simplicity.

Real world resonators are imperfect and leak photons through input and output ports at rate κ. The circuit QED is said to be in the *strong coupling regime* whenever $g \gg \kappa$, which means that we can find time scales in which quantum effects dominate the dynamics. Below we will outline important properties of the Circuit-QED architecture. In particular, we will consider the interaction between microwave photons and the artificial atom as the external field is turned off, resulting either in the Jaynes Cummings model for small values of g or in the Ultra Strong coupling regime in the presence of a large g. We will then consider the case of a driven cavity and see how tuning the external field to match the resonator frequency ω_c leads to an efficient, quantum non-demolition measurement scheme for the artificial atom, while matching it to the atomic Bohr frequency $\omega_0 := \omega_{01}$ effectively leads to quantum control of the atomic state in the *qubit* subspace $\mathrm{span}\{|\phi_0\rangle, |\phi_1\rangle\}$.

Atom-Photon interaction in Circuit QED

When $\epsilon(t) = 0$, the only states involved in the dynamics of the systems are those in the qubit space of the atomic Hilbert space. By defining the Pauli matrices $\sigma_z := |\phi_0\rangle \langle\phi_0| - |\phi_1\rangle \langle\phi_1|$ and $\sigma_x := |\phi_0\rangle \langle\phi_1| + |\phi_1\rangle \langle\phi_0|$, the Hamiltonian of the Circuit-QED system can be rewritten as:

$$H = \omega_c a^\dagger a + \frac{1}{2}\omega_0 \sigma_z + g(a + a^\dagger)\sigma_x \qquad (2.19)$$

which is known as the Rabi Hamiltonian. It is insightful to look at the rotating frame Hamiltonian defined by $H_{rf} = U_{rf} H U_{rf}^\dagger - i\dot{U}_{rf} U_{rf}^\dagger$, where the unitary operator $U_{rf} := \mathrm{e}^{-i\omega_c(a^\dagger a + 1/2\sigma_z)t}$ has been defined. Its expression is

$$H_{rf} = \frac{1}{2}\Delta\sigma_z + g(a\sigma_+ + a^\dagger\sigma_-) + g(a\sigma_+ \mathrm{e}^{-2i\omega_c t} + a\sigma_- \mathrm{e}^{2i\omega_c t}) \qquad (2.20)$$

where we used the atom - resonator detuning $\Delta := \omega_0 - \omega_c$. The last term of Eq. 2.20 has components oscillating with frequencies $\pm 2\omega_c$, i.e. counterrotating terms. Neglecting them amounts to perform the RWA with respect to the resonator field. This is possible in the regime $|\Delta|, |g| \ll \omega_c, \omega_0$. Applying the RWA and going back to the laboratory frame we get the Jaynes and Cummings (JC) Hamiltonian

$$H = \omega_c a^\dagger a + \frac{1}{2}\omega_{01}\sigma_z + g(a\sigma_+ + a^\dagger\sigma_-) \qquad (2.21)$$

In order to point out some important properties of the JC model, we define as $|n\rangle$ the eigenstates of the resonator mode with n excitations and decompose the resonator operators as $a = \sum_n \sqrt{n} |n-1\rangle \langle n|$. In the eigenbasis of the uncoupled atom and resonator, the JC Hamiltonian in the laboratory frame can thus be written as

$$
\begin{aligned}
H = & \sum_{n=0}^{\infty} (n+1)\omega_c(|\phi_0, n+1\rangle \langle\phi_0, n+1| + |\phi_1, n\rangle \langle\phi_1, n|) \\
& + \frac{\Delta}{2}(|\phi_0, n+1\rangle \langle\phi_0, n+1| - |\phi_1, n\rangle \langle\phi_1, n|) \\
& + g\sqrt{n+1}(|\phi_0, n+1\rangle \langle\phi_1, n| + |\phi_1, n\rangle \langle\phi_0, n+1|) = \sum_n \Pi_n H \Pi_n
\end{aligned}
\tag{2.22}
$$

Where we defined the projectors

$$
\Pi_0 := |\phi_0, 0\rangle \langle\phi_0, 0|, \quad \Pi_n := |\phi_0, n\rangle \langle\phi_0, n| + |\phi_1, n-1\rangle \langle\phi_1, n-1|, n > 0 \tag{2.23}
$$

that project, respectively, the Hamiltonian onto the ground state $|\phi_0, 0\rangle$ and onto the subspaces $\text{span}\{|\phi_0, n\rangle, |\phi_1, n-1\rangle\}$ of $n > 0$ total excitations, i.e. the sum of both atomic and photonic excitations. The Jaynes and Cummings Hamiltonian is block diagonal with respect to such subspaces, thus conserving the total number of excitations. Eigenvalues of the JC model are easily computed as

$$
E_0 = 0; \quad E_n^{\pm} = n\omega_c + \frac{\Delta \pm \sqrt{ng^2 + \Delta}}{2}, n > 0 \tag{2.24}
$$

In Circuit-QED the dispersive regime $|\Delta/g| \ll 1$ is particularly interesting. In this regime it can be shown[30], e.g. by applying Average Hamiltonian Theory (see appendix B), that the Jaynes and Cummings Hamiltonian can be approximated as

$$
H = \omega_c a^{\dagger}a + \omega_0 \sigma_z + \chi a^{\dagger}a\sigma_z \tag{2.25}
$$

where $\chi := g^2/\Delta$. We notice that the last term can be read as a shift on the frequency of the resonator *conditional* on the qubit state. This is, as we shall see later in this section, the mechanism used to measure the qubit state.

The Ultra Strong Coupling Regime

The RWA does not hold any more as g approaches the cavity frequency ω_c. In this last case, the full Rabi Hamiltonian of Eq.(2.19) and the regime $\omega_c \sim g$ is called Ultra Strong Coupling (USC) regime. The full Rabi Hamiltonian does
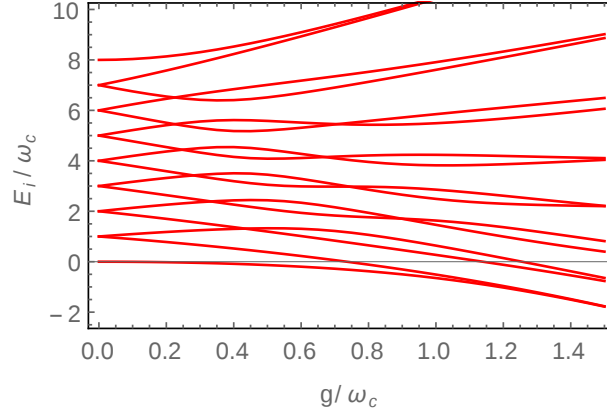
Figure 2.8: Spectrum of the Cavity-Atom system vs the coupling constant g.

not conserve the number of excitations, but only their parity. An important consequence is that the ground state of the system acquires a component on the $n = 2$ excitation manifold. In the resonant regime ($\Delta = 0$), up to the second order in g/ω_c, the ground state $|\phi\rangle_0$ and its energy become

$$|\Phi_0\rangle = |0,g\rangle - \frac{2g\omega_c}{4\omega_c - 2g^2}|1,e\rangle + \frac{g^2}{4\omega_c - 2g^2}|2,g\rangle \; ; E_0 = -\frac{g^2\omega_c}{2\omega_c^2 - g^2} \qquad (2.26)$$

Above, E_0 is the Bloch-Siegert shift, a distinctive feature of RWA breaking and USC. In Fig.2.1.4 we plot the spectrum of the Circuit-QED system vs the coupling constant g. We see how dropping the RWA has a dramatic effect in the spectrum. The linear behaviour of the spectrum for increasing g is, in fact, broken by the appearance of the Bloch-Siegert shift. We will to consider an application to USC in chapter 6.

Control in circuit QED

We are now going to address how control of the state of the artificial atom can be addressed in the dispersive regime of the Circuit-QED implementation. We will consider a two-level atom coupled to a mode of a resonator driven at a frequency $\omega \simeq \omega_0$. Extension to a multi-level atom driven by a multi-tone field is then straightforward due to linearity. We will thus consider the JC Hamiltonian of Eq.2.21 and supplement it with driving, i.e.

$$H = \omega_c a^\dagger a + \frac{1}{2}\omega_0\sigma_z + g(a\sigma_+ + a^\dagger\sigma_-) + \epsilon(t)(a^\dagger e^{-i\omega t} + a e^{i\omega t}) \qquad (2.27)$$

To see how this Hamiltonian effectively implements σ_x control for the atom, we apply the unitary transformation $U = e^{\frac{g}{\Delta}(a\sigma_+ - a^\dagger\sigma_-)}$ and retain terms up to order 1 in g/Δ to get[30], in the rotating frame defined by U_{rf},

$$H_{rf} \simeq \frac{1}{2}\left\{\omega_0 + \left[2\chi\left(a^\dagger a + \frac{1}{2}\right)\right] - \omega\right\}\sigma_z + \frac{\Omega(t)}{2}\sigma_x + \Delta_r a^\dagger a + \epsilon(a + a^\dagger) \quad (2.28)$$

where we defined the Rabi frequency $\Omega(t) := 2g\epsilon(t)/\Delta$ and the external field - resonator detuning $\Delta_r := (\omega_c - \omega)$. For $|\epsilon/\Delta_r| \ll 1$ the quantum field in the resonator is effectively decoupled from the dynamics. We can therefore assume that the resonator will lay in a zero photon state and derive the following Hamiltonian for the atom alone

$$H = \frac{\delta}{2}\sigma_z + \frac{\Omega(t)}{2}\sigma_x \quad (2.29)$$

with the external field - atom detuning defined as $\delta := \omega_0 - \omega$. We have shown how control along σ_x and σ_z can be achieved[2]. Control in the σ_y direction can be achieved by controlling the phase of ϵ, here assumed real for simplicity.

Measurement in Circuit-QED

We are now going to outline the measurement technique most widely used in Circuit-QED. It is attained by pumping the resonator with a field at frequency $\omega \simeq \omega_c$. Such a field has the effect of injecting into the resonator photons that get entangled with the artificial atom. Therefore, the field leaking from the resonator at rate κ will carry information about the artificial atom state. Measuring such leaking field can be easily done, for example through the homodyne scheme.

In a rotating frame defined by $U_{rf} = e^{-i\omega\hat{a}^\dagger\hat{a}t}$ the Hamiltonian of the system is

$$H_{rf} = \omega_0\ \sigma_z + \Delta_r\hat{a}^\dagger\hat{a} + \epsilon_d(t)(\hat{a} + \hat{a}^\dagger) + \chi\hat{a}^\dagger\hat{a}\sigma_z \quad (2.30)$$

where we used the dispersive approximation of Eq. 2.25. Including the effect of cavity damping, the dynamics of the density matrix of the Circuit-QED system $\rho(t)$ is described by the master equation

$$\dot{\rho}(t) = -i[H_{rf}, \rho(t)] + \kappa\mathcal{D}[a]\rho(t) \quad (2.31)$$

where κ is the cavity photon loss rate and the dissipator superoperator has the

---

[2]Control along σ_z can be made time-dependent either via modulating the Bohr frequency of the device by changing the E_J/E_C ratio through the application of an external magnetic field, or via chirping of the external field

standard form

$$\mathcal{D}[\hat{A}]\hat{B} = \hat{A}\hat{B}\hat{A}^\dagger - \frac{1}{2}\{\hat{A}^\dagger\hat{A}, \hat{B}\} \tag{2.32}$$

The solution to Eq. (2.31), provided a coherent state[82] of the resonator, e.g. the ground state, has been prepared at time $t = 0$, has form

$$\rho(t) = \sum_{i,j\in\{0,1\}} \left(c_{ij}(t)\,|\phi_i\rangle\langle\phi_j| \otimes |\alpha_i(t)\rangle\langle\alpha_j(t)|\right) \tag{2.33}$$

where $|\alpha_k\rangle$ are coherent states for the field, that is eigenstates of the annihilation operator such that $a\,|\alpha_k\rangle = \alpha_k\,|\alpha_k\rangle$. The equations of motion for the amplitudes c_{ij} and α_k are given by

$$\begin{aligned}
c_{ii}(t) &= c_{ii}(0) \\
c_{ij}(t) &= c_{ij}(0)\frac{\mathrm{e}^{-i2\chi\int_0^t ds\ \alpha_i(s)\alpha_j^*(s)}}{\langle\alpha_j(t)\rangle\,\alpha_i(t)}, \quad i \neq j \\
\dot{\alpha}_0(t) &= -i\epsilon(t) - [i(\Delta_r + \chi) + \kappa]\alpha_0(t) \\
\dot{\alpha}_1(t) &= -i\epsilon(t) - [i(\Delta_r - \chi) + \kappa]\alpha_1(t)
\end{aligned} \tag{2.34}$$

Tracing over qubit degrees of freedom, we are left with the field state $\rho_f = c_{00}(0)\,|\alpha_0(t)\rangle\langle\alpha_0(t)| + c_{11}(0)\,|\alpha_1(t)\rangle\langle\alpha_1(t)|$. Information on the qubit state is, therefore, translated into the resonator degrees of freedom. The distinguishability of α_0 and α_1 gives the strength of the measurement[83]. The steady state value of the two amplitudes, assuming constant ϵ, is

$$\alpha_j(t \gg \kappa^{-1}) = -i\,\frac{\epsilon}{i(\Delta_r + (-1)^j\chi) + \kappa} \tag{2.35}$$

Assuming, now, $\Delta_r = 0$ and $\kappa \gg \chi$ we have

$$\begin{aligned}
\mathrm{Im}\{\alpha_0\} = \mathrm{Im}\{\alpha_1\} &= -\frac{\epsilon}{\kappa} \\
\mathrm{Re}\{\alpha_0\} = -\mathrm{Re}\{\alpha_1\} &= -\frac{\chi\epsilon}{\kappa^2}
\end{aligned} \tag{2.36}$$

Meaning that, in this case, information on the qubit is encoded in the in-phase quadrature, thereby continuous homodyne measurement of $X := (\hat{a} + \hat{a}^\dagger)/\sqrt{2}$ is insightful. In Fig.2.1.4 we graphically show the conditional phase shift of the field quadratures in the phase space. In section 2.2.1 we will extend the measurement theory in Circuit-QED to account for continuous measurement and quantum trajectories.
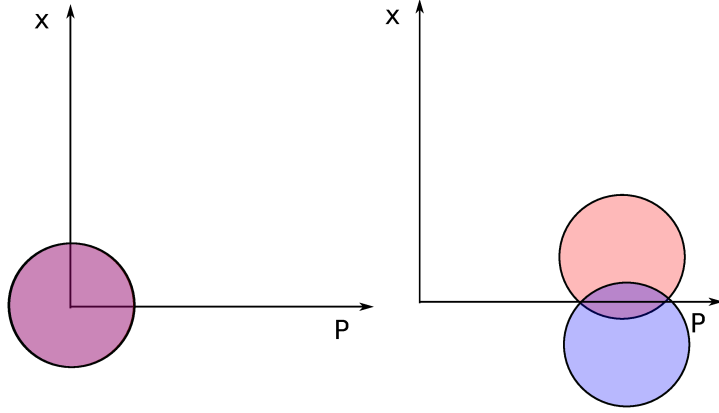
Figure 2.9: Pictorial representation of the Q function of the $|\alpha_0\rangle$ (blue) and $|\alpha_1\rangle$ (red) states in the phase space. The quadrature in the axis are $X = \frac{a+a^\dagger}{\sqrt{2}}$ and $P = -i\frac{a-a^\dagger}{\sqrt{2}}$. Immediately after switching on of the external field (left panel), the state of the resonator field does not distinguish between the two atomic states. After a certain amount of time (right panel), separation in the in-phase quadrature X allows to infer the state of the atom by measurements on the field.

2.2 Decoherence and noise

In the following chapters, we will often consider the dynamics of artificial atoms in an open quantum systems setting[84, 85]. We will therefore assume a large environment coupled to the atomic system and causing it to decohere. Different noise sources act on the devices, but independently on their nature they produces essentially two distinct classes of effects[45, 43]. Environmental modes with frequencies comparable to Bohr or Rabi frequencies act as sources of Markovian quantum noise, whose leading low-temperature effects are spontaneous decay, the associated secular dephasing and field-induced absorption [48, 86]. At lower frequencies, noise in the solid state is non-Markovian and exhibits a $1/f^\alpha$ behavior. The leading effect is pure dephasing, analogous to inhomogeneous broadening produced by a classical noise source, and it is effectively described by a stochastic external drive with the desired spectral features [45, 43].

According to this picture, we describe Markovian quantum noise by a dissipator $\mathcal{L}_D$ term in a Lindblad Master Equation

$$\dot{\rho}_f(t|\tilde{\mathbf{x}}) = -i[H(\tilde{\mathbf{x}}(t)), \rho_f(t|\tilde{\mathbf{x}})] + \mathcal{L}_D\rho_f(t|\tilde{\mathbf{x}}) \qquad (2.37)$$

where we also account for the effect of non-Markovian noise by allowing the parametric dependence on the classical stochastic processes $\{\tilde{\mathbf{x}}(t)\}$. Under reasonable

conditions, these latter can be thought to affect only the system Hamiltonian H. The full noisy dynamics is obtained by averaging over the classical stochastic processes, i.e.

$$\rho(t) = \int \mathcal{D}\tilde{\mathbf{x}}(t) \, P[\tilde{\mathbf{x}}(t)] \, \rho(t|\tilde{\mathbf{x}}) \tag{2.38}$$

An important simplification comes from the fact that low-frequency noise has a $\sim 1/f^\alpha$ behavior. This means that, given a protocol of duration T, most often the relevant part of its power spectrum will contain frequencies $\ll 1/T$. As a consequence, the effects of low-frequency noise can be seen as quasistatic fluctuations of the energy levels $\Delta\epsilon_i$ and of the dipole matrix elements $\Delta\mathcal{Q}_{ij}$ of the device. The path integral Eq.(2.38) can therefore be evaluated in the Static Path Approximation(SPA) [45, 43], reducing to an ordinary integration over random variables $\tilde{\mathbf{x}}$, that is

$$\rho(t) = \int d\tilde{x} \, P[\tilde{\mathbf{x}}] \, \rho(t|\tilde{\mathbf{x}}) \tag{2.39}$$

where $P(\tilde{\mathbf{x}})$ is the multivariate probability distribution of the noise parameters $\tilde{\mathbf{x}}$. As a consequence of the central limit theorem, this latter is moreover a normal distribution if we assume that they are due to many uncorrelated microscopic sources. This means that the covariance matrix, or equivalently the variances of the $\tilde{x}_i$ and their correlations, uniquely identify their full statistics. Such quantities can be easily extracted by experiments by measuring the non-secular dephasing (see section 5.A).

2.2.1 Quantum trajectory theory for continuously monitored artificial atoms

Our goal is now to describe the conditional evolution of the Circuit-QED system when the field leaking out of the cavity is continuously measured. For the sake of simplicity, we will only consider a two-level artificial atom, i.e. a qubit. If we neglect decoherence for the qubit, which, as it will be argued in chapter 7, can be done with present technology implementations, the total dynamics of the system is described by the Master Equation

$$\dot{\rho}(t) = -i[H, \rho(t)] + \kappa\mathcal{D}[a]\rho(t) \tag{2.40}$$

where the Hamiltonian H is in general driven by both a control field at frequency $\omega \simeq \omega_0$ and a measurement field at frequency $\omega_d = \omega_c$. In the dispersive approx-

imation, such Hamiltonian is given by

$$H = \omega_0\ \sigma_z + \omega_c \hat{a}^\dagger \hat{a} + \chi \hat{a}^\dagger \hat{a} \sigma_z + \frac{\Omega(t)}{2}(\sigma_- \mathrm{e}^{i\omega t} + \sigma_+ \mathrm{e}^{-i\omega t})$$
$$+ \epsilon_d(t)(\hat{a}\mathrm{e}^{i\omega_d t} + \hat{a}^\dagger \mathrm{e}^{-i\omega_d t}) \tag{2.41}$$

In Eq.(2.40) we also used the photon leak rate κ and the dissipator $\mathcal{D}$ given in Eq. (2.32).

We can think of Eq.(2.40) as the dynamical equation that describes the evolution of the compound qubit and cavity system when we average over all possible *quantum trajectories*[87]. A quantum trajectory is the stochastic evolution of a system coupled to an environment in which quantum measurements are performed on the environment. The observer can, in this way, keep track of the information leaking from the system into the environment. Since, in quantum mechanics, the measurements process is stochastic in nature and inevitably brings back-action into the system, averaging over quantum trajectories will lead to an evolution that is different from the closed, unitary one. This is in striking contrast with classical physics. Dissipation in the Master Equation (2.40), hence decoherence, can be explained in this framework as *unread* measurements performed on the environment. In the Circuit-QED scenario, the if we were able to continuously measure the field leaking from the cavity, we could single out individual quantum trajectories.

Different measurements strategies lead to different quantum trajectories. In turn, the choice a particular measurement protocol leads to a different *unravelling* choice for the Master Equation (2.40). An unravelling choice is described by a stochastic Master Equation that generally preserves the purity of the state and is dependent on a stochastic process reflecting the non deterministic nature of quantum measurement. Averaging with respect to such a process gives again the unconditional evolution described by Eq. (2.40).

In Circuit-QED, it is possible to observe single quantum trajectories of an artificial atom through homodyne measurement of the resonator field. Quantum trajectory theory of homodyne measurements has first been described by Wiseman and Millburnin Ref. [88], and it has been extended to circuit-QED by Gambetta et al. [89]. In the homodyne scheme, illustrated in Fig.2.10, the leaking field is mixed with a strong local oscillator through a beam splitter. The field of the Local oscillator can be thought as a classical coherent state of amplitude $\gamma/\sqrt{1-\eta}$, where η is the transmittance coefficient of the beam splitter. In the
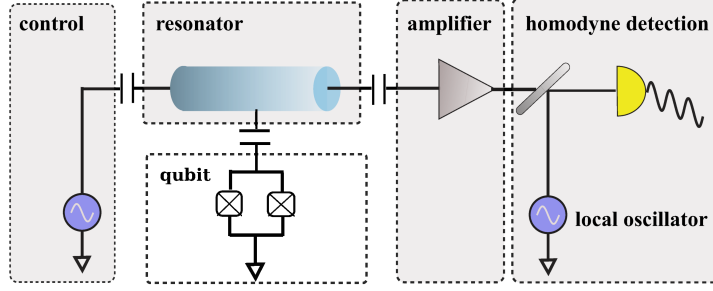
Figure 2.10: Homodyne measurement scheme in circuit-QED.

presence of an almost perfectly transmittive beam splitter, the output field is

$$\hat{o} = \hat{a} + \gamma \qquad (2.42)$$

and the output photon number is therefore given by

$$\hat{n}_o = \hat{o}^\dagger \hat{o} = |\gamma|^2 + \gamma \hat{a}^\dagger + \gamma^* \hat{a} + \hat{a}^\dagger \hat{a} \simeq |\gamma|^2 + \sqrt{2}|\gamma|\hat{X}_\phi \qquad (2.43)$$

where ϕ is the phase of γ. Apart from a constant contribution given by $|\gamma|^2$, the output photon number is therefore given by the quadrature $\hat{X}_\phi := (\hat{a}e^{-i\phi} + \hat{a}^\dagger e^{i\phi})/\sqrt{2}$. The stochastic master equation describing homodyne quantum trajectories is given by

$$\dot{\rho}(t) = -i[H, \rho(t)] + \kappa \mathcal{D}[a]\rho(t) + \kappa \xi(t)\mathcal{H}[a]\rho(t) \qquad (2.44)$$

where $\xi(t)$ is a gaussian white noise term with

$$\begin{aligned} \mathrm{E}[\xi(t)] &= 0 \\ \mathrm{E}[\xi(t)\xi(t')] &= \delta(t - t') \end{aligned} \qquad (2.45)$$

and the non linear superoperator $\mathcal{H}$ is given by

$$\mathcal{H}[\mathcal{A}]\mathcal{B} = AB + BA^\dagger - \mathrm{Tr}[AB + BA^\dagger]B \qquad (2.46)$$

In order to apply important results from the quantum thermodynamics community, we will rephrase the evolution given by Eq. (2.44) in the language of Positive Operator Valued Measurements (POVM) operator, i.e. collections of operators $\{L_x\}$ defining a generalized measurement[90]. The measurement theory formalism is also useful in devising efficient numerical methods[91] for simulations

of quantum trajectories of artificial atoms. In the homodyne scheme, the number of photons at the output port of the beam splitter is continuously observed. We can think of this process as a continuous projective[90] measurement of the output photon number n_o. It is more convenient, though, to work with the output photocurrent $I_h(t)$ instead, defined as the number of output photons per unit time, given by[87]

$$I_h(t) = \sqrt{k}\langle X_0 \rangle + \xi \tag{2.47}$$

To the leading order in dt, the infinitesimal, conditional evolution of the density operator can then be written as

$$\rho(t + dt) = \frac{L_{I_h}(\mathbb{1} - iH)\rho(t)(\mathbb{1} + iH)L_{I_h}^\dagger}{\mathrm{Tr}[L_{I_h}(\mathbb{1} - iH)\rho(t)(\mathbb{1} + iH)L_{I_h}^\dagger]} \tag{2.48}$$

where we introduced the measurement operators $L_{I_h} := [\mathbb{1} - 1/2\kappa a^\dagger a + \kappa I_h(t)dt]p_o(I)$, with $p_o(I_h) := \sqrt{dt/2\pi}\exp[-1/2dtI_h{}^2]$ being the *ostensible*[87] probability density for I_h. In Eq. 2.48) unitary evolution and evolution due to measurement in the infinitesimal time interval dt are factorized. The process can be interpreted as follows. At time t the system is in the state $\rho(t)$. It is then infinitesimally evolved through the time evolution operator $U(t) \simeq \mathbb{1} - iH(t)$. The sample $I_h(t)$ is obtained from the measurement - assumed instantaneous - of the output photocurrent. The action of the POVM operators L_I reflects quantum *back-action*, i.e. it relates to the disturbance that quantum measurements inevitably induce onto a quantum system.

The probability of sampling the photocurrent $I_h(t)$ at time t given the state $\rho(t)$ is given by.

$$p(I_h(t)|\rho(t)) = \mathrm{Tr}[L_{I_h}(\mathbb{1} - iH)\rho(t)(\mathbb{1} + iH)L_I^\dagger] \tag{2.49}$$

Now, the *ostensible* standard deviation of I_h is $dt^{-1/2}$. We make the *Ansatz* that it will also be the standard deviation of the actual distribution and, following Ref. [87], define a quantity $S := I_h\sqrt{dt} \sim 1$. Therefore we have

$$p(S) = \sqrt{\frac{1}{2\pi}}\exp(-S^2/2)[1 + S\langle X_0 \rangle\sqrt{dt} + \mathcal{O}(dt)] \tag{2.50}$$

That, up to the leading order, is equivalent to

$$p(I_h) = p_o(I_h - \langle X_0 \rangle) \tag{2.51}$$

Eqs. (2.48) and (2.51) completely define the quantum trajectory theory for continuous homodyne measurements. Discarding measurement results $I_h(t)$ is equivalent to averaging over every possible result for J, performing which gives

$$\bar{\rho}(t+dt) := \int dJ L_J \rho(t) L_J^\dagger = \rho(t) - i[\hat{H}, \rho(t)]dt + \mathcal{D}[\hat{c}]\rho(t)dt \qquad (2.52)$$

which is, as expected, identical to the unconditional Master Equation (2.31).

Quantum trajectory theory for the qubit alone

The conditional dynamics of the qubit alone when the latter is subject to continuous homodyne measurements can be found by tracing over the field degrees of freedom. Since, in general, the qubit and the resonator get entangled, their reduced states are not pure. Under certain conditions, though, the entanglement is negligible and the conditional dynamics of the qubit alone can be considered. This has been sudied in Ref. [89], where a Stochastic Master Equation (SME) for the qubit alone was found. The conditions to be met in order to neglect the entanglement between resonator and qubit are $\chi \ll \kappa$, $\Omega \ll \kappa$ and $\bar{n} \ll 1$, where $\bar{n} \simeq |\alpha_0|^2 \simeq |\alpha_1|^2 \simeq |\epsilon/\kappa|^2$ is the mean number of photons in the cavity[83]. We shall recast the SME of Ref. [89] in the form of Bloch equations in the basis of the bare qubit Hamiltonian $H_0 := 1/2\,\omega_0\sigma_z$. In the present section, in order to simplify the notation, we shall refer to the qubit's state as ρ and to its Hamiltonian as H. In the rotating frame, the driven Hamiltonian for the qubit is therefore $H = 1/2\,\delta\sigma_z + \Omega(t)\sigma_x$ and the Bloch equations read:

$$\begin{aligned}
\dot{\rho}_{00}(t) = -\dot{\rho}_{11}(t) &= -2H_{01}Im\{\rho_{01}\} \\
&\quad + 2\sqrt{\Gamma_d}\rho_{00}\rho_{11}(I_h - \sqrt{\Gamma_d}\langle\sigma_z\rangle) \\
\dot{\rho}_{01} = \dot{\rho}_{01}^* &= iH_{00}\rho_{01} + iH_{01}(\rho_00 - \rho_{11}) \\
&\quad - \sqrt{\Gamma_d}(\rho_{00} - \rho_{11})(I_h - \sqrt{\Gamma_d}\langle\sigma_z\rangle) - \frac{\Gamma_d}{2}\rho_{01}
\end{aligned} \qquad (2.53)$$

With such a choice for the phase of the local oscillator, the full-spectrum homodyne current can be written as $I_h = \sqrt{\Gamma_d}\langle\sigma_z\rangle + \xi(t)$.

We are going to use this result in section 7.A, where we will derive the model we employed to produce results and simulations of chapter 7.

Chapter 3

Design of a Lambda system in superconducting artificial atoms

The implementation of a three-level Lambda System in artificial atoms would allow to perform advanced control tasks typical of quantum optics in the solid state realm, with photons in the μm/mm range. However, hardware constraints put an obstacle since protection from decoherence is often conflicting with efficient coupling to external fields. We address the problem of performing conventional STImulated Raman Adiabatic Passage (STIRAP) in the presence of low-frequency noise. We propose two strategies to defeat decoherence, based on "optimal symmetry breaking" and dynamical decoupling. We suggest how to apply to the different implementations of superconducting artificial atoms, stressing the key role of non-Markovianity.[1]

3.1 Introduction

In recent years several experiments have demonstrated multilevel coherence in superconducting artificial atoms, as the observation of the Autler-Townes (AT) [92, 93] effect, of electromagnetically induced transparency (EIT) [94], besides evidences of three-state superpositions [95] and coherent population trapping (CPT) [96]. Further exploiting coherence in such systems would be important in principle and moreover allow important applications in solid-state quantum integrated coherent architectures. So far all the experiments in these systems (except the one

---

[1]The content of this chapter is adjusted, with minor modifications, from P.G. Di Stefano, E. Paladino, A. D'Arrigo, B. Spagnolo and G. Falci, Design of a Lambda configuration in artificial coherent nanostructures, Rom. Jour. Phys. 60:676-685, 2015.

of Ref. [96]) have been performed driving by ac-fields in *ladder* configuration [see Fig. 3.1(a)]. In this chapter we address the design of a *Lambda* configuration in three-level artificial atoms which would allow to implement tasks [97, 49, 56] where two-photon absorption *and* emission are invoved at once. In spite of several theoretical proposals [98, 80, 99, 48, 100], this goal is still experimentally unsettled, mainly because protection from low-frequency noise requires to enforce exact or approximate symmetries of the Hamiltonian, which on the other hand imply selection rules cancelling the pump coupling [98, 56, 48] [see Fig. 3.1(a)].

Our second goal of is to elucidate the central role of non-Markovian noise in producing three-level decoherence for the class of phenomena based on CPT. We focus on a protocol called STIRAP [47, 101], described in Sec. 3.2, which involves several basic coherent effects and allows striking applications in integrated atom-cavity systems. Therefore its demonstration would be a benchmark for multilevel advanced control in artificial atoms. In Sec. 3.3 we introduce an effective model for noise and argue that dephasing in the "trapped subspace" span$\{|0\rangle, |1\rangle\}$ (see Fig. 3.1a) plays the major role. We show that implementation of STIRAP in Lambda configuration is possible within present technology. In Sec. 3.4 we propose two strategies to defeat dephasing, namely the search for optimal symmetry breaking conditions, and selective dynamical decoupling of noise sources achieved by operating on a specific external control. Both strategies leverage on the fact that dephasing in the solid state is due to broad band colored noise (BBCN), which is inherently non-Markovian. As a consequence BBCN impacts on dephasing in a way specific of correlations of the induced fluctuations of the device bandstructure. Finally in Sec.6.5 we conclude and discuss some further perspective.

3.2   Coherent population transfer in three-level atoms

STIRAP is an advanced control technique for $M > 2$-level systems, allowing complete population transfer between two states $|0\rangle$ and $|1\rangle$, even in absence of a direct coupling, via one or more intermediate states which are *never* populated. In three-level systems the indirect linkage is provided by the typical configurations of two ac-fields shown in Fig. 3.1(a). The pump field at $\omega_p \approx |E_2 - E_0|$, where E_i is the energy of state $|i\rangle$, triggers transitions $|0\rangle \leftrightarrow |2\rangle$ whereas the Stokes, $\omega_s \approx |E_2 - E_1|$, triggers $|1\rangle \leftrightarrow |2\rangle$ ones. The standard Hamiltonian in the rotating wave approximation (RWA) in a rotating frame referred to the "bare" basis
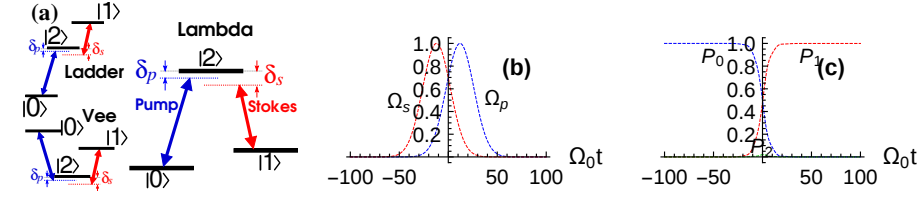
Figure 3.1: (a) Three-level system driven with AC fields in Λ configuration (in the insets the Ladder and the Vee configurations). (b) Gaussian pulses in the counterintuitive sequence (here $\Omega_0 T = 20, \tau = 0.6\,T$). (c) Population histories $P_i(t) = |\langle i|\psi(t)\rangle|^2$ for ideal STIRAP ($\delta = 0$) and for $\delta_p = -0.2\,\Omega_0$, $\kappa = 1$.

$\{|0\rangle, |1\rangle, |2\rangle\}$ is given by the matrix

$$H = \begin{bmatrix} 0 & 0 & \frac{1}{2}\Omega_p^*(t) \\ 0 & \delta(t) & \frac{1}{2}\Omega_s^*(t) \\ \frac{1}{2}\Omega_p(t) & \frac{1}{2}\Omega_s(t) & \delta_p(t) \end{bmatrix} \tag{3.1}$$

where the Rabi frequencies $\Omega_k(t)$ for $k = p, s$ are related to the amplitudes of the pump and Stokes fields, δ_k are the single-photon detunings and $\delta = \delta_p - \delta_s$ is the two-photon detuning. We will mostly refer to the Lambda configurations where $\delta_p(t) := E_2 - E_0 - \omega_p$ and $\delta_s(t) := E_2 - E_1 - \omega_s$. At two-photon resonance, $\delta = 0$, the Hamiltonian (3.1) has an instantaneous eigenvector with null eigenvalue, $\epsilon_0 = 0$, given by

$$|D\rangle = \frac{\Omega_s |0\rangle - \Omega_p |1\rangle}{\sqrt{\Omega_s^2 + \Omega_p^2}} \tag{3.2}$$

which is called the "dark state" since state $|2\rangle$ is not populated, despite of the transitions triggered by the fields. In ideal STIRAP ($\delta = 0$), adiabatic pulses $\Omega_k(t)$ are shined in the *counterintuitive* sequence, i.e. the Stokes preceding the pump as in Fig. 3.1(b). We will make use of Gaussian pulses

$$\Omega_p = \kappa_p \Omega_0 \, e^{-[(t+\tau)/T]^2} \qquad \Omega_s = \kappa_s \Omega_0 \, e^{-[(t-\tau)/T]^2} \tag{3.3}$$

with $\tau \sim T$. Here Ω_0 is a frequency scale and $\kappa_k \sim 1$ are constants which will be taken equal to 1 when not otherwise specified. In this way the dark state $|D(t)\rangle$ performs the desired $|0\rangle \to |1\rangle$ evolution, yielding complete population transfer, while $|2\rangle$ is never populated [Fig. 3.1(c)].

Adiabaticity in ideal STIRAP [47, 101] requires that $\Omega_0 T > 10$. Since it involves in a clever sequence several coherent phenomena [101] (AT effect, EIT and adiabatic passage), STIRAP is very efficient, faithful and stable apart for
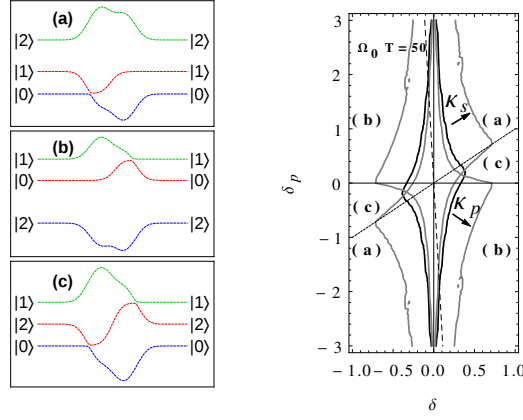
Figure 3.2: Left panel: typical Landau-Zener (LZ) patterns as a function of time of instantaneous eigenvalues for nonzero detunings. Three different patterns may occurr according to the value of δ_p/δ (see Sec.3.4). Right panel: efficiency diagram of STIRAP vs detunings. The curves enclose regions corresponding to efficiency larger than 90%. The black line is obtained for $\kappa_p = \kappa_s$ and shows that the protocol is much more sensitive to deviations of δ rather than of δ_p. Gray lines are the efficiencies when $\kappa_p = 2\kappa_s$ and $\kappa_s = 2\kappa_p$ (see Sec. 3.4). Intercepts of such curves with lines $\delta_p/\delta = a$ define the two-photon linewidths $\delta_{\frac{1}{2}}$ as a function of all the parameters but δ. The dashed line shows the example of the Cooper pair box for $q_g = 0.48$ and $J = 1$.

a crucial sensitivity to δ (see Fig. 3.2 right panel). Indeed for $\delta \neq 0$ no exact dark state exists providing the adiabatic connection $|0\rangle \rightarrow |1\rangle$. Still population transfer may take place by *non-ideal STIRAP*, via non-adiabatic Landau-Zener (LZ) transitions between adiabatic states (see Fig. 3.2 left panel), a mechanism crucial for the applications in artificial atoms (Sec.3.4).

In artificial atoms the Hamiltonian reads [43, 99] $H = H_0(\mathbf{q}) + [\mathcal{A}_p(t)\cos(\omega_p t) + \mathcal{A}_s(t)\cos(\omega_s t)]\mathcal{Q}$, where the device H_0 depends on tunable parameters $\mathbf{q}$. The field couples to the system dipole-like operator $\mathcal{Q}$ (see Sec. 2.1.2) and the envelopes $\mathcal{A}_k(t), k = p, s$ are slowly varying with respect to Rabi frequencies. Under suitable conditions, H can be truncated to three levels. Performing the RWA and transforming to a doubly rotating frame, we get the form (3.1), where $\Omega_p(t) = \mathcal{A}_p(t)\,\mathcal{Q}_{20}$ and $\Omega_s(t) = \mathcal{A}_s(t)\,\mathcal{Q}_{21}$.

3.3 Effective model for solid-state noise

As discussed in Sec. 2.2, noise in solid-state devices has large low-frequency components with a $1/f^\alpha$ spectrum, and high frequency component, either white or

ohmic. Assuming for simplicity a single noise source inducing fluctuations of the parameter q_g, we can describe this BBCN by the phenomenological Hamiltonian [43] $H = H_0(q_g + x(t)) + \mathcal{A}(t)\mathcal{Q} + H_{env}$. Here $x(t)$ is a classical stochastic process accounting for low-frequency noise, whereas H_{env} describes an environment coupled to the system, responsible for Markovian quantum noise. The effect of low-frequency noise is obtained by averaging over the stochastic process the density matrix $\rho^f(t|q_g + x(t))$, accounting for fast noise in a background stochastic field

$$\rho(t) = \int \mathcal{D}x(t) \, P[x(t)] \, \rho^f(t|q_g + x(t)) \tag{3.4}$$

Leading effects are estimated by evaluating the integral in the "quasistatic" or static path approximation (SPA), i.e. by substituting $x(t)$ with a random variable x with distribution $p(x)$ and calculating $\rho^f(t|q_g + x)$ by a Markovian master equation (see Sec. 2.2).

Notice that H_0, its eigenenergies $E_i(q_g)$ and the matrix elements $\mathcal{Q}_{ij}$ entering $\Omega_{ij}(q_g)$ depend on q_g. As detailed in Sec. 2.1.2, a proper choice of q_g may enforce symmetries of H, which protect the system against dephasing due to fluctuations of $E_i(q_g)$, but at the same time suppress some $\mathcal{Q}_{ij}$. Non-Markovian noise determines fluctuations of the entries of the Hamiltonian (3.1), namely $\delta_k(q_g+x) = \Delta E_k(q_g+x) - \omega_k$ and $\Omega_k(q_g+x) = \mathcal{A}_k(t)\,\mathcal{Q}_k(q_g+x)$, where $\Delta E_k(q_g+x)$ and $\mathcal{Q}_k(q_g + x)$ are the relevant energy splittings and "dipole" matrix elements. This is a key issue for all our subsequent analysis about design and optimization of Lambda systems. For instance, it is clear that for a Lambda configuration at nominal resonance, i.e. if external fields are resonant at the nominal bias q_g, fluctuations in the "trapped subspace" translate in stray $\delta \neq 0$ which are the most detrimental for STIRAP. It is convenient to expand detunings and Rabi frequencies. For instance at nominal resonance and for small enough fluctuations, imposing $E_0 = 0$ we have

$$\delta(x) = A_1(\mathbf{q})x + \frac{1}{2}B_1(\mathbf{q})x^2 \quad ; \quad \delta_p(x) = \Delta E_2 = A_2(\mathbf{q})x + \frac{1}{2}B_2(\mathbf{q})x^2 \tag{3.5}$$

where $A_i(\mathbf{q}) = \partial E_i(\mathbf{q})/\partial q_g$ and $B_i(\mathbf{q}) = \partial^2 E_i(\mathbf{q})/\partial q_g^2$. We notice that all such fluctuations are correlated via the bandstructure of the device, since they originate from the same random variable x.

We apply these ideas to the important case study of the Cooper pair box (CPB), that we described in sec.2.1.2. Here we conveniently give the Hamiltonian

in units of the Charging Energy E_C, i.e.

$$H_0(q_g, J) = \sum_n (q_g - n)^2 \left| \phi_n \right\rangle \left\langle \phi_n \right| - \frac{J}{2} (\left| \phi_{n+1} \right\rangle \left\langle \phi_n \right| + h.c.). \qquad (3.6)$$

where we defined $J := E_J/E_C$ and we used $\hat{n} := \sum_n n \left| \phi_n \right\rangle \left\langle \phi_n \right|$ as the number of extra Cooper pairs in a metallic island. The parameter J is, therefore, the relative strength of the Josepson tunnelling changing $n \to n \pm 1$. According to its value several different implementations of superconducting qubits from "charge qubits" to "transmons" [33, 102, 103, 104, 74] have been demonstrated. The other parameter q_g can be tuned by an external voltage. The CPB is operated by an ac gate voltage which is coupled to the charge, $\mathcal{Q} \propto \hat{n}$, playing the role of the system operator.

The Hamiltonian $H_0(q_g, J) = \sum_i E_i \left| i \right\rangle \left\langle i \right|$ is symmetric for charge parity transformations at half-integer and integer q_g. Here the selection rule $n_{ij} := \left\langle i \right| \hat{n} \left| j \right\rangle = [1 - (-1)^{i+j}] n_{ij}$ holds, preventing pump coupling. On the other hand working at $q_g = 1/2$ guarantees the maximal protection from charge noise because of the suppression of $A_i(\mathbf{q})$ in Eq.(3.5). Larger values of $J \gg 1$ suppress asymmetries at $q_g \neq 1/2$, ensuring protection in a larger region of the space of parameters, where however the pump coupling is suppressed [48].

The numerically calculated [48] efficiency of STIRAP (Fig. 3.3a) shows that a Lambda configuration allowing population transfer $\sim 80\%$ is achievable in a CPB with $J = 1$ by operating at a symmetry breaking bias $q_g \neq 1/2$, despite of the reduced protection from low-frequency noise. In this regime, $q_g \lesssim 0.49$, only linear fluctuation of detunings matter, i.e. linear terms in Eqs.(3.5) are considered. We used $\Omega_0 T = 15$ to guarantee good adiabaticity, with figures of noise and couplings consistent with measurements of the decoherence in the qubit of Ref. [1]. In this regime, Markovian emission [47, 101] or absorption [48] channels are not effective, whereas spontaneous decay in the trapped subspace, characterized by T_1, is tolerably small. Instead near $q_g = 1/2$ pump coupling is small and it would require $T \gg T_1$, thereby decay suppresses the efficiency.

3.4   Strategies of protection against noise

We now analize the tradeoff between efficient coupling and decoherence when parity symmetry is broken. Our analysis leverages on the results of last section, that the main mechanism of efficiency loss (besides lack of adiabaticity) are low-frequency fluctuations of energy levels. As discussed in Sec.3.3, these correspond
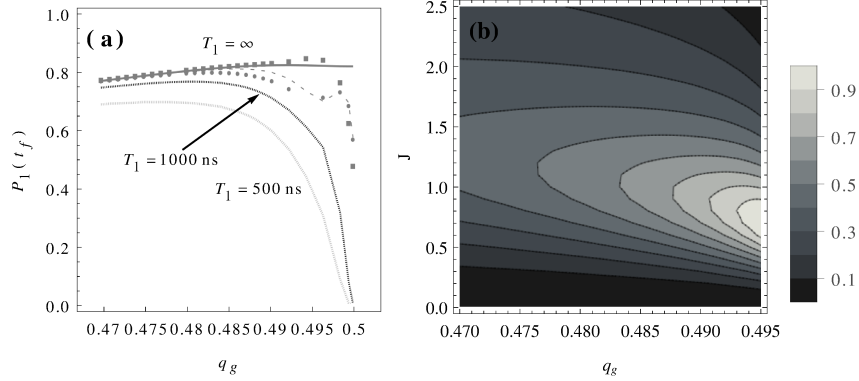
Figure 3.3: (a) Efficiency of STIRAP in the CPB for $J = 1$, showing the effect of low-frequency noise alone and with additional Markovian noise. Field amplitudes, corresponding to Rabi oscillations $\Omega_R/2\pi = 600$MHz in the Quantronium qubit [1] operated at the symmetry point, yield a sufficiently large pump frequency $\Omega_0 \simeq \Omega_R n_{02}(q_g)/n_{01}(0.5)$ for values of q_g which slightly break the symmetry. Here we consider linear fluctuations of detunings (thick solid line), while adding their quadratic fluctuations (squares) and fluctuations of Ω_k in linear (dashed line) and quadratic approximation (dots) has no effect. Markovian noise determines a smaller further reduction of the efficiency (thin gray lines). We used a variance $\sigma_x = 0.004$ of $p(x)$ and $T_1 = 500, 1000$ ns (see Sec. 5.A). (b) Figure of merit Eq.(3.7) for design and optimal symmetry breaking against low-frequency charge noise in the CPB. We consider the region where charge noise is linear since closer to the symmetry point $q_g = 1/2$, STIRAP is suppressed by spontaneous decay.

to fluctuations of detunings and can be represented on the diagram of Fig. 3.2 by a curve. For vanishing nominal detunings it has parametric equations (3.5) and passes the origin for $x = 0$. Notice that in general in artificial atoms fluctuations of detunings produced by a specific noise source show specific correlations. In the linear noise regime $\delta_p/\delta = a$, where $a = A_2(\mathbf{q})/A_1(\mathbf{q})$, thereby the signs of the derivatives $A_i(\mathbf{q})$ of the bandstructure determine whether detunings are correlated (e.g. critical current noise in flux qubits) or anticorrelated (e.g. charge noise in the CPB) [43]. It has been shown [99] that according to such correlations, three different kind of LZ patterns may occurr. They are shown in Fig. 3.2 (left panel) and labelled with (a) for $\delta_p/\delta > 1$, (b) for $\delta_p/\delta < 0$ and (c) for $0 \leq \delta_p/\delta < 1$. The efficiency dependence on parameters turns out to be different in the three cases, this being the key to classify effects of low-frequency noise and the specific strategies to suppress them.

Since *both* couplings and fluctuations depend on the solution of the eigenproblem of $H_0(\mathbf{q})$, we may seek for an "optimal" set of values $\mathbf{q}$ such that the

symmetry breaking yields enough pump coupling still keeping decoherence tolerable. Referring to Fig. 3.2 we formulate this condition by defining a *two-photon linewidth* [54] $\delta_{\frac{1}{2}}$, as the interval of δ where coherent transfer is appreciable, for any fixed combination of the other parameters (see Fig. 3.2). For efficient STIRAP low-frequency noise must induce fluctuations of δ with small enough variance, $\sigma_\delta \approx \sqrt{A_1^2 \sigma_x^2 + \frac{1}{2} B_1^2 \sigma_x^4} \lesssim \delta_{1/2}$.

The linewidth can be estimated by evaluating the impact of unwanted transitions between adiabatic states. In this way Vitanov et al. [54] found the scaling law $\delta_{\frac{1}{2}} \simeq d(\tau)\Omega_0\sqrt{\kappa_p^2 + \kappa_s^2}$ valid for $\delta_p = 0$, and roughly holding on the lines $\delta_p/\delta = a$ in the region (c) of Fig. 3.2 left. In the same way one can derive that $\delta_{\frac{1}{2}} \approx d'(\tau, \kappa)\Omega_0 \kappa_p$ in the region (b) of anticorrelated detunings [48], whereas $\delta_{\frac{1}{2}} \approx d''(\tau, \kappa)\Omega_0 \kappa_s$ in the region (a) of correlated detunings. The dependence on $\kappa := \kappa_s/\kappa_p$ in the prefactors turns out to be weak.

In the case of CPB, since A_1 and A_2 have different sign, charge noise determines anticorrelated fluctuations of detunings, and good transfer efficiencies are achieved for large values of the ratio

$$\frac{\delta_{\frac{1}{2}}}{\sigma_\delta} \propto \frac{\kappa_p \Omega_0}{\sigma_\delta} \approx \frac{2\, n_{02}(J, q_g)}{\sqrt{A_1^2(J, q_g)\sigma_x^2 + \frac{1}{2} B_1^2(J, q_g)\sigma_x^4}}. \tag{3.7}$$

This is a figure of merit for STIRAP efficiency (see Fig. 3.3b) which can be used for seeking optimization of both the design of the device and the symmetry breaking of the Hamiltonian modulated on-chip by the bias q_g.

The above analysis also suggests that effects of charge noise in a CPB can be minimized by increasing κ_p only. This is a specific way of decoupling dynamically noise sources, responsible for anticorrelated (δ, δ_p) fluctuations. Indeed it is clear from Fig. 3.2(b) that increasing κ_p the efficiency grows in the region (b), suppressing anticorrelated fluctuations of detunings. This happens because non ideal STIRAP occurs via LZ tunneling along the pattern (b) in Fig. 3.2, being suppressed for increasing δ when the avoided crossing builds on, and being restored if the gap shrinks due to a larger Ω_p.

This analysis can be extended to the main different designs of superconducting artificial atoms, and to each specific low-frequency noise source. These latter are classified according to the (δ, δ_p) correlations they determine. For instance flux noise in flux qubits yields anticorrelated (δ, δ_p), as for charge noise in the CPB, and increasing Ω_p yields dynamical decoupling. Instead critical current noise in CPB and flux qubit determine correlated (δ, δ_p) fluctuations, requiring larger Ω_s.

We address the issue of detuning correlations in further detail in Sec. 5.A. In phase qubits both critical current and bias current noise yield correlated (δ, δ_p) fluctuations dynamically suppressed by a large Ω_s.

In real superconducting artificial atoms, where more than one noise source is present, the two strategies can be combined. Protection from noise producing anticorrelated (δ, δ_p) fluctuations can be achieved by the optimal symmetry breaking strategy, since dynamical decoupling is limited by the insufficient coupling Ω_p. Protection from noise producing correlated (δ, δ_p) fluctuations can then be obtained increasing Ω_s, which is not limited by selection rules.

It is easy to extend this analysis to artificial atoms driven in different field configurations. For instance for population transfer in the Ladder scheme(Fig. 3.1) scheme one associates δ (δ_p) with the second (first) excited state, which allows to identify the relevant correlations between detunings.

3.5 Implications of non-Markovianity

The picture of the last section relies on the non-Markovianity of BBCN. We remind that low-frequency noise is the main source of dephasing in artificial atoms. BBCN explains distinctive experimental observations in qubits [43, 1, 2, 105]. Moreover design of low-decoherence qubits relies on protection from non-Markovian noise. Both optimal tuning [106, 107] and dynamical decoupling [108, 109] have been exploited for entangled states. We generalize these ideas to protection of three-level coherence, obtaining a rich scenario.

It is important to point out the different impact on STIRAP of non-Markovian dephasing, as discussed in this chapter, and Markovian pure dephasing as described by the standard Master Equation approach. This latter problem has been studied in Ref. [110], including only the dephasing rates $\tilde{\gamma}_{ij}$. For large enough $\Omega_0 T$ populations at the end of the protocol were found to be

$$\rho_{11}(\infty) = \frac{1}{3} + \frac{2}{3} \mathrm{e}^{-3\tilde{\gamma_0}_1 T^2/8\tau} \quad ; \quad \rho_{00}(\infty) = \rho_{22}(\infty) = \frac{1}{3} - \frac{1}{3}\mathrm{e}^{-3\tilde{\gamma_0}_1 T^2/8\tau} \quad (3.8)$$

i.e. dephasing determines efficiency losses which do not depend on the peak Rabi frequencies. Therefore Markovian dephasing cannot at all accout for the scenario presented in Sec. 3.4.

In Fig. 3.4 we plot the final populations of the bare states comparing Markovian (ρ_{ii}) and non-Markovian (P_i) pure dephasing, in the entire relevant range of Ω_0. Noise produces in both cases the same qubit dephasing time T_2, which is
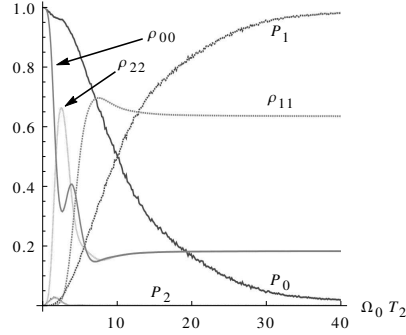
Figure 3.4: Final populations of STIRAP with Markovian (ρ_{ii}) and non Markovian (P_i) noise. The former is the solution of a Master Equation with rate $\tilde{\gamma}_{10} = 1/T_2$, leading to exponential decay of qubit coherences. The non-Markovian noise is simulated taking a distribution of detunings corresponding to $\sigma_x = \sqrt{2}/(A_1 T_2)$, leading to Gaussian decay with the same T_2.

relatively large. When Ω_0 is large, while for non-Markovian noise P_1 is completely recovered, for Markovian noise it saturates to a smaller value given by Eq.(3.8). For small Ω_0 the protocol fails in both cases, due to insufficient adiabaticity.

3.6   Conclusions

In this chapter we discussed effects of BBCN noise in three level artificial atoms. In particular we studied the tradeoff between protection from low-frequency noise, enforced by symmetries of the Hamiltonian, and the implied selection rules which are the main obstacle to the implementation of a Lambda scheme. Being based on two-photon absorption *and* emission, the Lambda scheme allows performing tasks as transduction of photons in the μm/mm range. We have studied STIRAP since it is a benchmark advanced protocol. It is also the basis of other protocols from preparation of superpositions [101] to transfer of wavepackets and manipulation of photons, with still unexplored potentialities for quantum information and quantum control.

We have shown that model for BBCN noise decoherence in the "trapped subspace" span$\{|0\rangle, |1\rangle\}$ plays a major role, a conclusion which holds for all Lambda, Ladder and Vee schemes. Strategies to defeat noise in qubits can then be generalized to three-level systems. We presented two strategies, namely optimal symmetry breaking and continuous dynamical decoupling, which can be integrated to minimize the effects of anticorrelated and correlated parametric fluctuations of the artificial atom bandstructure. Relying on non-Markovianity of BBCN, our

results suggest that features of the scenario of STIRAP with BBCN, as the predictions on the peculiar dependence on control knobs described in Sec. 3.4, could be used to probe aspects of non-Markovianity of the solid-state evironment.

Finally, we mention that artificial atoms allow for new unconventional schemes to manipulate a Lambda system, bypassing hardware constraints and allowing to perform STIRAP at protected symmetry points and with always-on fields (see chapter 4. The strategies to defeat noise presented here could be successfully applied also in these cases.

Chapter 4

Population transfer in a Lambda system induced by detunings

In this chapter we propose a new protocol to achieve coherent population transfer between two states in a three-level atom by using two ac fields. It is based on the physics of Stimulated Raman Adiabatic Passage (STIRAP), but it is implemented with the constraint of a reduced control, namely one of the fields cannot be switched off. A combination of frequency chirps is used with resonant fields, allowing to achieve approximate destructive interference, despite of the fact that an exact dark state does not exist. This new chirped STIRAP protocol is tailored for applications to artificial atoms, where architectures with several elementary units can be strongly coupled but where the possibility of switching on and off such couplings is often very limited. Demonstration of this protocol would be a benchmark for the implementation of a class of multilevel advanced control procedures for quantum computation and microwave quantum photonics in artificial atoms.[1]

4.1 Introduction

Preparation of a quantum system in a well defined state is an essential task in many branches of modern physics ranging from atomic and molecular physics [101] to quantum computation [90]. Techniques for transferring population from a ground state $|0\rangle$ to a state $|1\rangle$ employ either Rabi cycling or adiabatic passage

---

[1]The content of this chapter is adjusted, with minor modifications, from P.G. Di Stefano, E. Paladino, A. D'Arrigo, G. Falci, Population transfer in a Lambda system induced by detunings, *Phys. Rev. B* 91:224506, 2015.

(AP) [54]. Amongst these latter STIRAP (see Sec. 3.2) is a three-level atom scheme where selective and faithful population transfer is achieved by operating with two resonant driving fields in Lambda configuration [47, 54]. The advantage over Rabi cycling is the dramatic reduction of sensitivity to fluctuations of the parameters, at the expenses of a longer duration of the adiabatic protocol. In more complex architectures semiclassical driving fields are substituted by harmonic modes of a strongly coupled cavity, and tasks as preparation of photons with controlled amplitude, frequency and polarization [111, 49] can be performed by vacuum-stimulated Raman AP (vSTIRAP).

In the last few years multilevel coherence in solid-state systems, from mesoscopic devices [100] to atomic-like impurity states [112], has been a fertile subject of investigation. Several theoretical proposals [113, 98, 56, 55, 80, 99, 48] and experiments [92, 114, 93, 96] have dealt with multilevel coherence in artificial atoms. As we detailed in Sections 2.1.2, 2.1.3 and 3.3, distinctive features of such systems is the effectiveness of parity selection rules [98, 55, 48] which together with the presence of strong $1/f$ noise [45, 43], impose constraints on the available control. Therefore new protocols for manipulating the coherent dynamics must be tailored for such systems. Their design requires that large couplings allowing for efficient control are combined with protection from noise [48].

In this chapter we present a new protocol to achieve coherent population transfer between the two lowest excited states of a three-level atom by using two ac fields. The key difference with standard STIRAP, where ac fields must be switched on and off in a counterintuitive sequence [47], is that one of the fields is kept always-on, its amplitude being constant during the protocol. Operating with an always-on field require phase modulation, and for this reason we call the protocol cSTIRAP (chirped STIRAP). Sweeping the frequency of a single classical driving field across the resonance is a standard way to switch on and off Rabi oscillations, thereby one may think to rephrase STIRAP accordingly, but this is not the case. Indeed coherent population requires destructive interference of the two fields [115]. This is guaranteed by cSTIRAP, which thereby solves a nontrivial control problem, its experimental demonstration in artificial atoms being by itself an important proof of principle of advanced three-level control. Even more interestingly, cSTIRAP could apply to architectures where "artificial atoms" are coupled to quantized modes, electromagnetic or nanomechanical, where strong coupling is achieved by non-switchable hardware elements keeping the interaction always-on. The protocol we propose possesses certain advantageous distinctive characteristics: (i) it works with reduced available control, as an always-on field,

(ii) it operates with nearly resonant fields, reducing the operation time; (iii) it may rely on better techniques to control the phase of microwave circuits, (iv) it is cyclic.

The chapter is organized as follows. In Sec.4.2 we introduce the model Hamiltonian and briefly review standard implementations of coherent population transfer in two and three-level atoms. In Sec. 4.3 we illustrate the new protocol discussing in Sec. 4.4 the robustness against parametric fluctuations and in Sec. 4.5 decoherence effects. Finally, in Sec.4.6, along with the conclusions, we will discuss the comparison of cSTIRAP with other protocols for population transfer operated by frequency chirps.

4.2 Coherent population transfer in Lambda atoms

In two-level systems coherent population transfer $|0\rangle \rightarrow |1\rangle$ by AP is performed by shining a direct coupling field whose detuning is swept through the resonance at the Bohr frequency of the transition. Common examples are Rapid AP (RAP) or Stark Chirped RAP (SCRAP) [101].

In three-level, as discussed in the previous chapter, systems population transfer may be achieved in absence of direct coupling, via a third *linkage* state $|2\rangle$, coupled to $|0\rangle$ and $|1\rangle$ by a pump field at frequency $\omega_p \simeq E_2 - E_0$ and a Stokes field at $\omega_s \simeq E_2 - E_1$, respectively. In particular the *Lambda configuration* depicted in the top inset of Fig. 4.1 will be considered in this chapter. Since $|2\rangle$ is usually short-lived, one of the goals of coherent techniques is to use $|2\rangle$ but *never populate it*. This is achieved in a very efficient and elegant way relying on destructive interference [115]. The Hamiltonian in the rotating wave approximation, in the basis of the bare states $\{|0\rangle, |1\rangle, |2\rangle\}$ and in the rotating frame has been given in Eq.(3.1). As detailed in the Sec. 3.2, conventional STIRAP relies on the two-photon resonance, $\delta(t) = 0$, at which such a Hamiltonian admits an exact dark state $|D\rangle$ with zero eigenvalue $\epsilon_0 = 0$, given by Eq. (3.2).

Another three-level technique, Raman Chirped Adiabatic Passage (RCAP) [116], uses instead phase modulation. Population transfer is achieved by two far off-resonance chirped laser pulse sweeping through resonance (see Sec. 4.6). Unlike conventional STIRAP, two-photon resonance is not kept during the whole process, causing a transient population of state $|2\rangle$ to appear. The latter in principle can be made small by accurate tuning of parameters.

4.3   Coherent population transfer with an always-on field

In this section we will address the problem of achieving $|0\rangle \to |1\rangle$ population transfer subject to two constraints, namely (a) keeping the population of $|2\rangle$ small and (b) operating with a reduced control, in particular with one of the fields, for instance the Stokes one, kept always on, $\Omega_s(t) =: \Omega_0 \neq 0$. Naively one could suppose that sweeping the detuning $\delta_s(t)$ could allow to effectively switch on and off Ω_s, allowing again for conventional STIRAP. However this is not the case because coherent population transfer requires that the two-photon resonance condition, $\delta = 0$, is kept while sweeping $\delta_s(t)$, to ensure destructive interference. In what follows we will seek for a solution allowing to achieve complete population transfer by properly shaping the detunings.

First of all when one of the fields is always on, the Hamiltonian (3.1) for $t \to \pm\infty$ is not diagonal in the bare state basis. In order to approximate asymptotically the desired target state $|1\rangle$, necessarily at the end of the protocol we must have $\delta_s \gg \Omega_0$. If we take detunings shaped as shown in Fig.4.1, which are given by

$$\delta_s(t) = \frac{1}{2} h_\delta \Omega_0 \left[\tanh\left(\frac{t-\tau}{\tau_{ch}}\right) + \tanh\left(\frac{t+\tau}{\tau_{ch}}\right) \right]$$

$$\delta_p(t) = \kappa_\delta \delta_s(t) \tag{4.1}$$

the desired asymptotics is ensured by $h_\delta \gg 1$, i.e. the protocol must start and end with "far detuned" lasers. The modulation (4.1) has the important characteristics that at least for part of the protocol $\delta(t) = 0$ (Fig. 4.1). During this phase a Stokes-induced Autler-Townes (AT) splitting opens. Although an exact adiabatic dark state is not available for population transfer, we will argue later that keeping $\delta \approx 0$ allows to minimize the transient population of $|2\rangle$.

The population transfer mechanism is better understood studying the evolution of the instantaneous eigenvalues and eigenvectors of the "Stokes" Hamiltonian, obtained setting to zero the pump field in Eq.(3.1)

$$H_s(t) = \begin{bmatrix} 0 & 0 & 0 \\ 0 & \delta(t) & \frac{1}{2}\Omega_0 \\ 0 & \frac{1}{2}\Omega_0 & \delta_p(t) \end{bmatrix} \tag{4.2}$$

Here the Rabi frequency has been taken real with no loss of generality. The Stokes Hamiltonian acts non-trivially only on the $\{|1\rangle, |2\rangle\}$ subspace, yielding
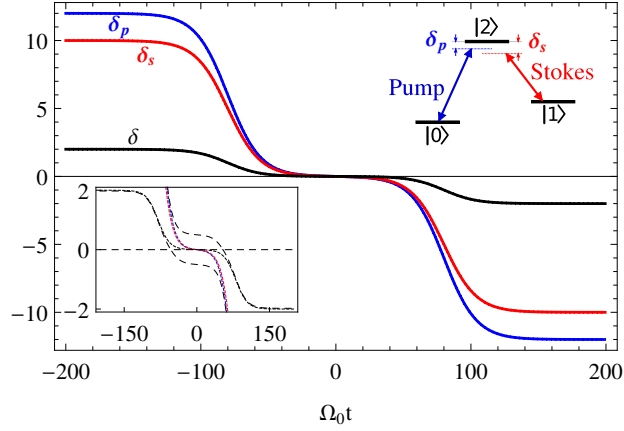
Figure 4.1: Main figure: single (coloured lines) and two-photon (dotted line) detunings in Ω_0 units. Top inset: Three level Lambda system. Bottom inset: Zoom of the single and two-photon detunings (solid lines), plotted together with the Stokes eigenvalues (dashed lines) of Eq. (4.4) showing the appearance of a dynamical Stokes-induced AT, which is switched on and off by modulation of δ_s.

the asymptotic states

$$
\begin{aligned}
|s_+(-\infty)\rangle &\simeq |2\rangle \to |s_+(+\infty)\rangle \simeq |1\rangle \\
|s_-(-\infty)\rangle &\simeq |1\rangle \to |s_-(+\infty)\rangle \simeq |2\rangle
\end{aligned}
\tag{4.3}
$$

The "Stokes eigenvalues" display the presence of the AT splitting during the protocol (Fig. 4.1, bottom inset)

$$
s_0 = 0, \quad s_\pm = \delta + \frac{\delta_s \pm \sqrt{\delta_s^2 + \Omega_0^2}}{2}
\tag{4.4}
$$

During this AT phase δ_s is swept across the resonance swapping $|1\rangle \leftrightarrow |2\rangle$.

Using detunings Eq.(4.1) with $\kappa_\delta > 1$ the pattern of split instantaneous eigenvalues $s_\pm(t)$ is crossed twice by the eigenvalue $s_0 = 0$, as shown in Fig. 4.2(a). Crossings occur at times $\pm t_c$ when $s_\pm(t) = 0$, i.e. $4\delta(t_c)\delta_p(t_c) = \Omega_0^2$. In these conditions the system prepared in $|\psi(-\infty)\rangle = |0\rangle$ remains of course in this state, passing through the crossing. Population transfer is achieved by applying a pump pulse with finite area reaching its peak value close to the second crossing, $t = t_c$. For instance, employing a a Gaussian pulse, we have

$$
\Omega_p(t) = \kappa \, \Omega_0 e^{-\left(\frac{t-t_c}{T}\right)^2}
\tag{4.5}
$$

The behavior is understood in terms of the instantaneous eigenenergies of the
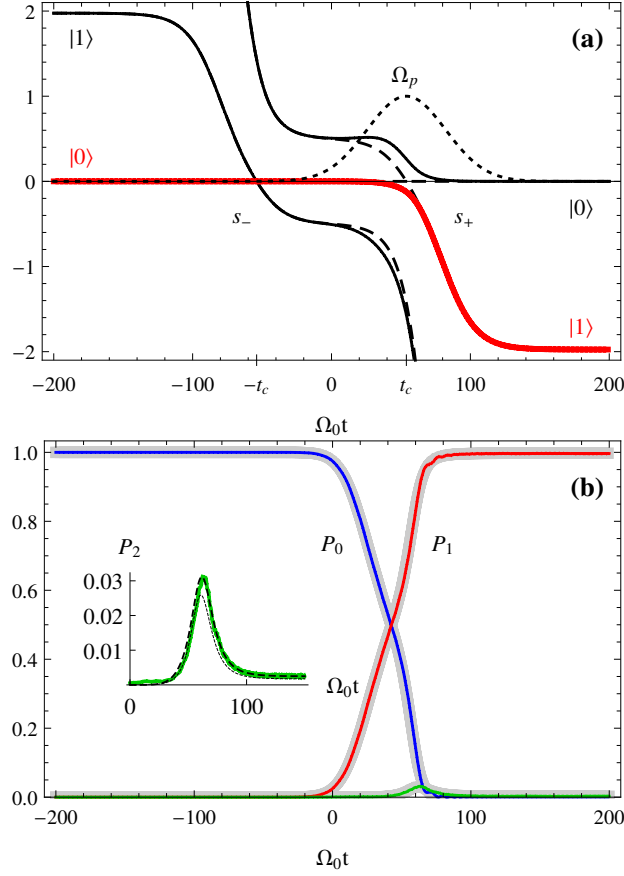
Figure 4.2: (a) Eigenvalues of the Stokes Hamiltonian of Eq. (4.2) (dashed lines) and of the full Hamiltonian of Eq. (3.1) (solid lines) in Ω_0 units. The red thick line is the instantaneous energy of the system adiabatically driven from $|0\rangle$ to $|s_+\rangle \simeq |1\rangle$ through the opening of the avoided crossing generated by the pump pulse (dotted line) at time $t = t_c$. (b) Population histories (red, blue and green lines) from the numerical solution of the Schrödinger equation, for $\Omega_s(t) = \Omega_0$, $\Omega_0 T = 40$, $h_\delta = 10$, $\kappa_\delta = 1.2$ and $\kappa = 1$, $\tau_{ch} = 0.6T$, showing complete population transfer by cSTIRAP. For these parameters the adiabatic approximation (gray curves) fully agrees with the exact solution. Inset: the exact population P_2 of the excited state (green solid line) is small at any time of the protocol, as can be estimated by Eq.(4.6) (thin line). The dashed line refers to the approximation of Eq. (4.13).

full Hamiltonian Eq. (3.1). In particular the pump pulse lifts the degeneracy between s_0 and s_+ turning their crossing into an avoided crossing [Fig.4.2(a)]. The adiabatic connection corresponding to s_+ yields eventually the desired population transfer, $|0\rangle \to |s_+(+\infty)\rangle \simeq |1\rangle$.

We remark that population transfer depends only on the presence of a crossing

between Stokes eigenenergies s_+ and s_0 and on the fact that the adiabatic approximation is valid. In this regime the precise shape of the pulses is not relevant. Therefore the protocol is robust against imperfections in the control. From the physical point of view it is worth stressing that the pump pulse triggers AP by a two-photon process. The distinctive feature of our proposal is that this two-photon effective coupling is obtained with both quasi resonant pump and Stokes fields. This ensures large efficiency for rather small pulse duration. We mention that during its switching on Ω_p could in principle trigger unwanted transitions $|0\rangle \to |2\rangle$, which are however suppressed by the Stokes-induced AT splitting and the two-photon resonance condition. A similar phenomenon occurs in standard STIRAP, where it is called the Stokes-induced EIT (electromagnetically induced transparency) phase [54].

Summing up cSTIRAP can be described in the language of Ref. [54] as a five stages protocol, with successive far-detuned, Stokes-induced AT, Stokes-induced EIT, two-photon AP and again far-detuned phases. In what follows we will see that the other important requirement, namely that population of $|2\rangle$ should be minimal at all times, is also fulfilled. This requirement is necessary in order to prevent unwanted decay processes likely to occur in real physical systems, where $|2\rangle$ is often unstable.

We estimate $P_2 = |\langle 2 \rangle \psi|^2$ by adiabatic elimination. The standard procedure formulated in the bare basis yields the state $|\psi_{AE}^0\rangle = c_0 |0\rangle + c_1 |1\rangle$ (see App. 4.A). First order corrections yield a leakage from the subspace $\{|0\rangle, |1\rangle\}$ given by [116]

$$P_2(t) \simeq \left| \frac{\Omega_p c_0 + \Omega_0 c_1}{2\delta_p} \right|^2 \tag{4.6}$$

that can be made very small, as shown in Fig.4.2(b), which also shows that this approximation works very well. A better approximation is obtained by working in the Stokes basis [see App. 4.A and Fig. 4.2(b)], but Eq.(4.6) has a simpler analytic form, allowing to write a figure of merit for the parametric dependence of leakage during the protocol. A simple choice is to consider leakage at the crossing $s_+ = 0$

$$P_2(t_c) \simeq \frac{\delta}{\delta_p} f(\kappa) = \frac{\kappa_\delta - 1}{\kappa_\delta} f(\kappa) \tag{4.7}$$

Here $f(\kappa)$ is a monotonically decreasing function of the ratio of the Rabi peak amplitudes κ. This qualitative behaviour is confirmed by numerical simulations shown in Fig. 4.3, where the efficiency is plotted versus relative magnitude of the amplitudes (κ, left panel) and of the detunings (κ_δ, right panel), both in
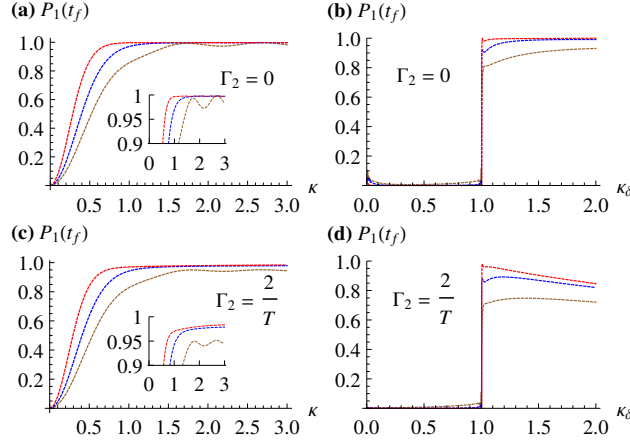
Figure 4.3: Upper panels: STIRAP efficiency vs the relative peak amplitudes of the fields (left panel, where $\kappa_\delta = 1.2$) and to the relative detunings (right panel, where $\kappa = 1$), for various degrees of adiabaticity (curves: $\Omega_0 T = 40$ (red), 20 (blue), 10 (brown) from higher to lower efficiency). For $\kappa_\delta > 1$, and provided adiabaticity is good, the system has a very slight sensitivity to these parameters. Lower panels: sensitivity of the efficiency to unwanted transient population of $|2\rangle$ accounted for by a finite lifetime $\tau_2 =: 1/\Gamma_2$ (cf. Eq.4.8). The insets of panels (a) and (c) are zooms of the corresponding main figures showing how, in the presence of a non-vanishing Γ_2, the efficiency improves with increasing κ.

the absence (top panel) and the in presence (bottom panel) of a finite lifetime $\tau_2 = T/2$ of the intermediate state $|2\rangle$ (see section 4.4 for a model). It is seen that efficiency increases with increasing κ as an effect of a larger avoided crossing at $s_+ = 0$. Moreover increasing κ reduces the transient population of $|2\rangle$, as given by the figure of merit Eq.(4.7). This is seen by comparing the insets of the left panels of Fig. 4.3: the positive slope of the sensitivity in the presence of a finite τ_2 [Fig. 4.3(c)] cannot be explained as an improvement in adiabaticity, since this slope is not present in the ideal case [Fig. 4.3(a)]. Therefore, it can only be caused by a reduction of P_2.

Population transfer occurs only for $\kappa_\delta > 1$ as shown in Fig. 4.3(b),(d). In particular, for $\kappa_\delta = 1$ we have $\delta(t) = 0$ and Eq.(3.2) applies, showing that an always on Stokes field would produce a return of the population to the initial state. For $\kappa_\delta < 1$ the Stokes eigenvalues do not cross, and adiabatic dynamics leads to a final population entirely in $|0\rangle$.

4.4 Sensitivity to parameters

The efficiency of cSTIRAP is not very sensitive to slight deviations of relative amplitudes κ and detunings κ_δ of the pulses, provided adiabaticity is kept. This is shown in Fig. 4.3, results in the lower panels allowing to fix convenient values $\kappa = 1$, $\kappa_\delta = 1.2$ and $\Omega_0 T = 40$, which we will use hereafter.

As in conventional STIRAP [54], the most critical feature is the parametric sensitivity to stray detunings. Here we discuss this issue, which is also responsible for decoherence due to low-frequency noise [43, 48].

The physics is understood recalling the picture of conventional STIRAP, where two kind of errors emerge [101]. "Bad projection" errors, due a bad choice of the pulse shape and timing, may lead to the wrong target state. "Bad adiabaticity" errors induce leakage from the trapped subspace, nonadiabatic transitions surely occurring when the so called "global condition" $\Omega_k T \gg 1$ is not met. Both kinds of errors are also triggered by fluctuations induced by an environment (see Sec.4.5). For cSTIRAP we verified that large enough $\Omega_k T$ again guarantees adiabaticity (Fig. 4.3). In this regime a strong asset of cSTIRAP is that it is not affected by bad projection errors in the far-detuned phases, since final eigenstates in the rotating frame are nondegenerate.

However since the efficiency of cSTIRAP depends on the structure of crossings of the eigenvalues of the Stokes Hamiltonian, it may be affected by stray detunings during the protocol. A further drawback comes from the fact that the state carrying population in cSTIRAP, while taking advantage from destructive interference, it is not an exact dark state as in Eq.(3.2), since the condition $\delta(t) = 0$ does not hold true. This is a potentially important source of error for cSTIRAP since it also may determine a nonvanishing population of $|2\rangle$ at intermediate times. Sensitivity to detunings is conveniently studied by the non-Hermitian Hamiltonian:

$$H(t|\{\delta_k\}) \rightarrow H(t|\{\delta_k\}) + i\frac{\Gamma_2}{2}|2\rangle\langle2| \tag{4.8}$$

Using a sufficiently large $\Gamma_2 > 1/T$ guarantees that transient population of $|2\rangle$ decays elsewhere (e.g. in a continuum), yielding a lack of normalization at the end of the protocol. Therefore the resulting efficiency $P_1(t_f)$ is a figure of merit embedding the requirement that $|2\rangle$ should be never populated.

The Hamiltonian (4.8), where only the dependence on detunings is empha-
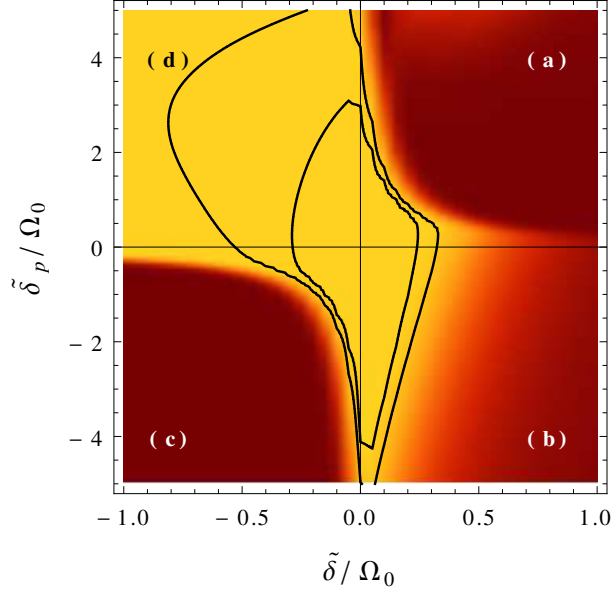
Figure 4.4: The color map describes the efficiency of ideal cSTIRAP, with $\Gamma_2 = 0$ vs fluctuations of the detunings. In the brightest area we have $P_1(t_f) > 0.9$. Lines refer to $\Gamma_2 = 1/T$ and delimit the $P_1(t_f) > 0.9$ (most inner region) and the $P_1(t_f) > 0.8$ areas. We use the same parameters as in Fig. 4.2(b), which guarantee that in absence of fluctuations, $\tilde{\delta}_s = \tilde{\delta}_p = \tilde{\delta} = 0$, adiabaticity of the protocol is strong. The extension of the regions of large efficiency determines the single-photon linewidths (in this case $\Delta\tilde{\delta}_s$) and the two-photon linewidth $\Delta\tilde{\delta}$.

sized, accounts for the effect of stray components by letting

$$\delta_k(t) \to \delta_k(t) + \tilde{\delta}_k, \quad k = s, p$$
$$\delta(t) \to \delta(t) + \tilde{\delta}, \quad \tilde{\delta} := \tilde{\delta}_p - \tilde{\delta}_s \tag{4.9}$$

Stray detunings may describe very slow phase fluctuations (at frequencies $\ll 1/T$) of the driving fields. Physically in solid-state devices they describe energy fluctuations due to coupling to an environment (see Sec.4.5 and Ref. [48]) whose power spectrum has $1/f^\alpha$ behavior [43]. In what follows we describe the detrimental effects they produce and the limitations they determine.

The efficiency of the protocol versus stray detunings is shown in Fig. 4.4. The colour map shows $P_1(t)$ for $\Gamma_2 = 0$ at the end of the protocol, $t = t_f$. Lines refer to finite $\Gamma_2 = 1/T$, which determines a reduced value of $P_1(t_f)$ since a nonvanishing population $P_2(t)$ would decay outside the system. It is seen that the efficiency is large in a whole region around the center of the plot (absence of fluctuations, $\tilde{\delta}_s = \tilde{\delta}_p = \tilde{\delta} = 0$), showing the stability of the protocol. The failure of cSTIRAP

in the region of larger detunings is analyzed in the App. 4.C. Here we mention that in the first and in the third quadrants of Fig. 4.4 failure is due to "bad projection" errors, i.e. the system may evolve along an adiabatic linkage leading to a wrong target state. Instead deep in the second quadrant the problem is "bad adiabaticity" due to an insufficient pump-induced two-photon avoided crossing.

Concerning sensitivity to τ, notice that the convenient delay is implicitly set by the choice of $\Omega_p(t)$ being maximal at the second crossing time, Eq.(4.5). We have checked that in these conditions the protocol is stable against deviations from the delay and the detailed pulse shape used in this chapter, provided they are not too large. Moreover it is worth stressing that the protocol we propose in the "ideal" detunings case, while being physically satisfactory, is not an optimal solution in the mathematical sense. Therefore we expect further improvement by tackling the problem with Optimal Control Theory.

4.5 Decoherence

A further important source of errors in STIRAP is decoherence [48], especially in solid-state artificial atoms. We discuss some qualitative aspect in this section. A key asset of conventional STIRAP is that while spontaneous decay from $|2\rangle$ may be large (decay time larger than the duration of the protocol), the phenomenon is supposed to have small impact as long as $|2\rangle$ is depopulated. This holds true also for cSTIRAP, as seen from the results for $\Gamma_2 \neq 0$ presented in the last Section. Markovian dephasing in STIRAP has been studied in detail [110] and its detrimental effect, namely leakage from the trapped subspace due to the weakening of destructive interference phenomenon, has been elucidated. It has been shown that strong Markovian dephasing is tolerated, as long as it does not affect the two levels of the trapped subspace. More complete studies of the effects of quantum noise in driven systems have pointed out that in solid state implementations of three-level artificial atoms the main effect is due to decay processes within the trapped subspace [48]. Other decoherence channels emerging in the Born-Markov approximation, namely the relation of rates to the detailed spectral density of the environment [86] and the possible drive-induced absorption [48], are less relevant.

On the other hand, unlike their natural counterpart, artificial atoms implemented by solid-state nanodevices suffer from low-frequency noise [43]. This drawback may be compensated by the ease of producing large couplings on chip, the tradeoff between protection and addressability being the central design issue. The effect of low-frequency noise in STIRAP has been discussed in Ref. [99], where

its interplay with Markovian noise and the role of device design were also addressed [48, 117]. The extension of this detailed analysis to cSTIRAP is beyond the scope of this work, but general features pointed out in the above works together with the results of the last section, allow to draw a physical picture which can be used as a guide for device design.

We assume that low efficiency may be determined by by decoherence leading to detrapping from the $\{|0\rangle, |1\rangle\}$ subspace and by failures of the adiabatic approximation also leading to unwanted population of $|2\rangle$. The simplest model encompassing these main features is to account for decay of $|2\rangle$ in a continuum due to quantum noise (Γ_2) and to account for dephasing as due to low-frequency (classical) fluctuations of relevant parameters. That is we consider the Hamiltonian Eq.(3.1) supplemented by the non-Hermitian term appearing in Eq.(4.8), and let $\delta_k(t) \to \delta_k(t) + \tilde{\delta}_k(t)$, for $k = s, p$, and $\Omega_k(t) \to \Omega_k(t) + \tilde{\Omega}_k(t)$, where $\tilde{\delta}_k(t)$ and $\tilde{\Omega}_k(t)$ are classical stochastic processes. In artificial atoms such fluctuations stem physically from noisy external bias fields, which induce fluctuations of the energy spectrum of the device (determining $\tilde{\delta}_k$'s) and of the operator coupling to the field (yielding $\tilde{\Omega}_k$'s). The efficiency is obtained by averaging over such fluctuations $P_1(t|\{\tilde{\delta}_k\}, \{\tilde{\Omega}_k\})$, at the end of the protocol. In cases of interest, as for $1/f$ noise, the average can be estimated in the quasistatic (or static-path) approximation [45, 43]. It amounts to substitute stochastic processes by random variables with a suitable Gaussian distribution, which physically accounts for sample to sample fluctuations of parameters. Results of the last section suggest that stray $\tilde{\Omega}_k$s hardly affect the efficiency, whereas the effect of the distribution of $\tilde{\delta}_k$'s can be important. This effect can be read off in Fig.4.4, which shows that for reasonably small fluctuations there is a region where still large efficiencies are allowed. Successful cSTIRAP requires that fluctuations of energy levels (i.e. detunings) are smaller than the linewidths. In analogy with the analysis of Ref [48] we expect that the condition of large efficiency depends on the bandstructure of the device at the bias point. Indeed depending on the device and on the noise source, fluctuations of the two splittings (detunings) are either correlated or anticorrelated [117], namely they are described by lines with positive or negative slope in Fig. 4.4. A figure of merit is the ratio $\delta_{\frac{1}{2}}/\sigma_\delta$ between the two-photon linewidth of STIRAP, corresponding to the width of the large efficiency region in the proper direction in Fig. 4.4, and the variance σ_δ of the fluctuations of the two-photon detuning.

4.6 Conclusions

In this chapter we have proposed a new protocol which extends conventional STI-RAP. Coherent population transfer is achieved with reduced available control, namely one of the field is kept always on. This procedure is suited for applications in artificial atoms and can be advantageous in integrated atom-cavity systems architectures, where couplings to quantized modes are implemented by non-switchable hardware [118], and may be manipulated in this way for applications to microwave quantum photonics [119]. In this respect it may be useful that cSTIRAP can be repeated cyclically since population histories are invariant when $\delta_k \to -\delta_k$, allowing the protocol to work as well in the reverted detunings configuration.

The protocol leverages on the fact that in the microwave realm external fields have a phase which can be usually controlled better than for sources at optical frequencies. In particular frequency can be modulated more accurately allowing direct time-dependent control of the detunings, instead of the induced Stark shifts used in genuine atomic systems [101]. Moreover in solid-state artificial atoms, e.g. superconductor based, detunings can be independently modulated by external voltages and fluxes.

Manipulation of detunings is the basis of other coherent transfer protocols like RCAP [116]. The essential difference between standard RCAP and cSTIRAP is that, owing to the fact that the Stokes field is always-on, our protocol involves a dressed state in the AP phase (see Sec. 4.3), whereas in the former AP occurs between bare states. Therefore while in RCAP the avoided crossing is due to the two-photon coupling of two far detuned dispersively coupled fields, in cSTIRAP AP takes place via destructively interfering *resonant* fields. This renders more robust the protocol, which achieves large efficiency for rather small pulse duration. On the other hand the analogy with RCAP, as well as the discussion of Sec. 4.5, suggests that also cSTIRAP may be resilient to phase noise and to low-frequency noise in nanocircuits offering advantages in quantum state processing with artificial atoms [80].

STIRAP is also the basis of other protocols as preparation of superpositions [101], transfer of wavepackets [120], manipulation of photons and quantum gates [80], with still unexplored potentialities for quantum information and quantum control. Therefore demonstration of cSTIRAP is a benchmark for a class of multilevel advanced control protocols in artificial atoms.

4.A   Adiabatic elimination of state $|2\rangle$

In order to estimate the population of $|2\rangle$ we start from the usual adiabatic elimination in the bare basis. The Schrödinger equation $i\partial_t |\psi\rangle = H |\psi\rangle$, with the Hamiltonian Eq.(3.1), is written for the components of $|\psi\rangle := \sum_{i=0}^{2} c_i |i\rangle$. Assuming $\dot{c}_2 \simeq 0$ one finds

$$c_2 = -\frac{\Omega_p c_0 + \Omega_s c_1}{2\delta_p} \tag{4.10}$$

This expression of c_2 is substituted in the Schrödinger equation yielding a two-state problem governed by the effective Hamiltonian

$$H_2(t) = \begin{bmatrix} -\frac{\Omega_p^2}{4\delta_p} & -\frac{\Omega_s \Omega_p}{4\delta_p} \\ -\frac{\Omega_s \Omega_p}{4\delta_p} & \delta - \frac{\Omega_s^2}{4\delta_p} \end{bmatrix} \tag{4.11}$$

Now assuming the validity of the adiabatic approximation, c_0 and c_1 are approximately given by the instantaneous eigenvectors of $H_2(t)$. In particular we consider the state corresponding to the preparation $|\psi(t_i)\rangle = |0\rangle$, and we can estimate $P_2 = |c_2|^2$ from Eq. (4.10). The analytic result is shown in Fig. 4.2(b), thin solid line in the inset, and it yields good agreement with the numerical curve. The analytic expression, though easy attainable, is cumbersome. Insight in the parametric dependence can be gained by evaluating leakage at $t = t_c$:

$$P_2(t_c) = \frac{\kappa_\delta - 1}{\kappa_\delta} \frac{(\kappa - \sqrt{\kappa^2 + 4})^2}{4 + (\kappa + \sqrt{\kappa^2 + 4})^2}$$

which is Eq. (4.6). We remind that adiabatic elimination yields coarse grained amplitudes and it is a priori enforced by large single-photon detunings. Remarkably the result obtained from Eq.(4.10) is accurate for the whole procedure, even if in part of the protocol the condition $\delta_p \gg \Omega_k$ is not met. This is due to the fact that the population of $|2\rangle$ is always small, either because the regime is dispersive or because there is destructive interference.

Corrections in the regime where $\delta_p(t) \lesssim \Omega_p, \Omega_s$ can be fully taken into account if adiabatic elimination is carried in the representation of the Stokes eigenstates. We write the Hamiltonian Eq.(3.1) in the basis $\{|0\rangle, |s_+\rangle, |s_-\rangle\}$, given by $|s_\pm\rangle = a_1^\pm |1\rangle + a_2^\pm |2\rangle$. By expressing $|\psi\rangle = c_0 |0\rangle + c_+ |s_+\rangle + c_- |s_-\rangle$ and assuming $\dot{c}_- \simeq 0$, we obtain $c_- = -(\Omega_-/2s_-)c_0$, where $\Omega_\pm = \Omega_p[1 + 4(\delta - s_\mp/\Omega_0)^2]^{-1/2}$. Substituting the Ansatz for c_- into the Schrödinger equation yields an effective
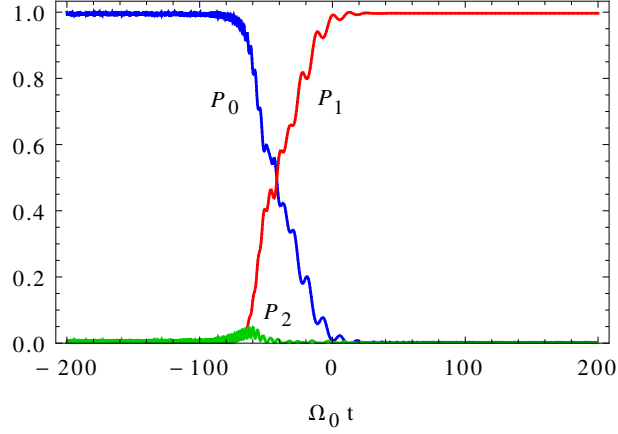
Figure 4.5: Population histories for $\Omega_p(t) =: \Omega_0, \Omega_0 T = 40, h_\delta = 10, \kappa_\delta = 1.2$, $\kappa = 1$ and $\tau_{ch} = 0.6T$.

2×2 Hamiltonian, which in the $\{|0\rangle, |s_+\rangle\}$ basis reads:

$$H_{2s} = \begin{bmatrix} -\frac{\Omega_-^2}{4s_-} & -\frac{\Omega_+}{2} \\ -\frac{\Omega_+}{2} & s_+ \end{bmatrix} \tag{4.12}$$

which yields the leakage to $|2\rangle$ in the form

$$P_2 \simeq |\frac{\Omega_+}{2s_-} c_0\, a_2^- + c_+\, a_2^+|^2 \tag{4.13}$$

As it is seen from Fig. 4.2(b) (dashed line) the result reproduces the numerical solution, but it does not yield a figure of merit as simple as Eq. 4.6.

4.B Always-on pump field

We can seek for a protocol dual to the always-on Stokes field by making the following substitutions, $t_c \to -t_c$, $\delta_p \rightleftarrows \delta_s$, $\Omega_p \rightleftarrows \Omega_s$. The population histories are shown in Fig. 4.5 and differ somehow from those of Sec.4.2. The point is that the system is prepared in $|0\rangle$, which in this case is not an exact eigenstate of the initial Hamiltonian. As a consequence Rabi oscillations of small amplitude appear in both P_0 and P_2. They can be substantially reduced by increasing the initial value of the pump detuning. Stray population may appear in the intermediate state $|2\rangle$ also due to adiabatic population transfer at the avoided crossing, and can be minimized by adjusting parameters as suggested by Eq. 4.6.

4.C   Failure of STIRAP at large detunings

We now analyze the dynamics in the regions of Fig. 4.4 where cSTIRAP fails. As mentioned in Sec. 4.4 when energy levels have infinite lifetime, failure of the protocol is due to two kind of errors, namely "bad adiabaticity" and "bad projection" [54]. While in the former case, the protocol fails because the avoided crossing produced by the fields is insufficient to guarantee adiabaticity, in the latter case the system is projected onto the wrong eigenstate of the Hamiltonian.

Errors mainly occur during the AP near the point at $t = t_c$ where Stokes eigenstates cross. An efficient protocol requires for the probabilities of Landau-Zener transitions between such states that $\gamma_{0 \to s_-} \ll 1$ and $1 - \gamma_{0 \to s_+} \ll 1$, which is not always met for finite stray detunings.

A qualitative picture of how cSTIRAP possibly fails due to stray detunings is offered by the patterns of the instantaneous eigenvalues of the full and of the Stokes Hamiltonians, in the darker regions of the three (a-c) quadrants of Fig. 4.4. Examples of these patterns are plotted in Fig. 4.6(a-c).

In the region deep in quadrant (a) of Fig. 4.4 detunings are such that the first crossings of the Stokes eigenenergies occurs *at positive times*, i.e. when Ω_p is already on [Fig. 4.6(a)]. Therefore $|0\rangle$ and $|s_-\rangle$ mix, originating a sort of initial "bad projection" error. Then the subsequent swap $|s_-\rangle \to |2\rangle$ leads to a wrong target state. Deep in quadrant (b), the protocol suffers from a sort of final "bad projection" error: the second crossing occurs *at negative times*, where $\Omega_p \approx 0$ and the correspondent transition becomes diabatic. This yields $|\psi(t)\rangle \approx |0\rangle$ at all times[2]. Deep in quadrant (c) cSTIRAP fails when the configuration of detunings renders the pump-induced avoided crossing insufficient. In this case the problem is "bad adiabaticity", Zener tunneling inducing unwanted transitions to the state adiabatically evolving towards $|0\rangle$.

Finally, deep in the quadrant (d) the configuration of detunings is such that the two "mixing" phases of the protocol are inverted. Indeed the Stokes-induced AT splitting becomes relevant only *after* the second crossing, which in the ideal case would have produced the two-photon AP. Therefore Ω_p partially injects population into $|2\rangle$. At later times, in the Stokes-AT phase, this population is swapped to $|1\rangle$. Although the final state is correct (cf. the large efficiency in Fig. 4.4), in the presence of decay $\Gamma_2 \neq 0$, occupation of $|2\rangle$ at intermediate times suppresses the efficiency [see Fig. 4.6(d) and the solid lines of Fig. 4.4].

---

[2]In describing the behaviour in the first and third quadrant we rely on the distinction between negative and positive times. This asymmetry roots from the choice of switching on $\Omega_p(t)$ at slightly positive times.
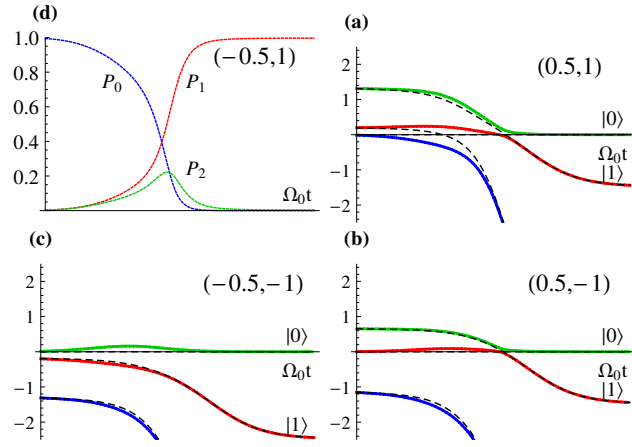
Figure 4.6: (a-c) Instantaneous eigenvalues of the Stokes (dashed lines) and complete (solid lines) Hamiltonians, in the dark regions of quadrants (a-c) of Fig. 4.4, in units of Ω_0. (d) Population histories corresponding to quadrant (d) of Fig. 4.4 for $\Gamma_2 = 0$, showing that, even if $P_1(t_f)$ is nearly one, the protocol suffers of large transient population of $|2\rangle$ (green line). In each panel the label $(\tilde{\delta}/\Omega_0, \tilde{\delta}_p/\Omega_0)$ indicates the value of the stray detunings.

Chapter 5

Coherent manipulation of noise-protected superconducting artificial atoms in the Lambda scheme

We propose a new protocol for the manipulation of a three-level artificial atom in Lambda (Λ) configuration. It allows faithful, selective and robust population transfer analogous to stimulated Raman adiabatic passage (Λ-STIRAP), in last-generation superconducting artificial atoms, where protection from noise implies the absence of a direct pump coupling, as detailed in Sections 2.1.2 and 2.1.3. It combines the use of a two-photon pump pulse with suitable advanced control, operated by a slow modulation of the phase of the external fields, leveraging on the stability of semiclassical microwave drives. This protocol is a building block for manipulation of microwave photons in complex quantum architectures. Its demonstration would be a benchmark for the implementation of a class of multilevel advanced control procedures for quantum computation and microwave quantum photonics in systems based on artificial atoms.[1]

---

[1]The content of this chapter is adjusted, with minor modifications, from P.G. Di Stefano, E. Paladino, T.J. Pope, G. Falci, Coherent manipulation of highly noise-protected artificial atoms in the Lambda scheme, *Phys. Rev. A* 93:051801, 2016.

5.1   Introduction

Advanced control of multilevel quantum systems is a key requirement of quantum technologies [90], enabling tasks like multiqubit or multistate device processing [121, 100, 122] by adiabatic protocols, topologically protected computation [123] or communication in distributed quantum networks[124, 125, 126]. These are currently investigated roadmaps towards the design of fault tolerant hardware, i.e. complex quantum architectures minimizing effects of decoherence [127, 75]. In this scenario artificial atoms are very promising since, compared to their natural counterparts, they allow for a larger degree of integration [118, 128, 129, 35], on-chip tunability, stronger couplings [4] and easier production and detection of signals in the novel regime of microwave quantum photonics [119]. Decoherence due to strong coupling to the solid-state environment [43] is their major drawback. Over the years it has considerably softened [75] yielding last-generation superconducting devices with decoherence times in the range $\sim 1 - 100\,\mu s$ [2, 3, 78].

Combining potential advantages of artificial atoms is by no means straightforward. Protection from decoherence often implies strong constraints to available external control, which pose key challenges when larger architectures are considered [35]. In this chapter we study a simple and paradigmatic example, namely a three-level artificial atom driven by a two-tone electric field in the Lambda configuration [Fig.5.1(a)]. Implementation of this control scheme in last-generation superconducting hardware may in principle benefit from low decoherence, which however is achieved by either biasing the device at the symmetry point (e.g. in flux qudits) or increasing the E_J/E_C ratio (e.g. in the transmon). This is done at the expenses of suppressing the direct coupling of the pump field, and of possible limitations of selectivity in addressing specific transitions. While in chapter 3 we studied how to optimize the design of the Lambda configuration by optimal symmetry breaking, in this chapter we show how to implement an efficient Lambda configuration at symmetry, and we propose a dynamical scheme allowing to operate quantum control. This solves the problem raised in the last decade by several theoretical proposals on the implementation of advanced control by a Lambda-scheme in artificial atoms [98, 130, 56, 80, 55, 100], which still awaits experimental demonstration.

Quantum control via a dynamical Lambda scheme is very important because it may provide a fundamental building block for processing in complex architectures. Indeed adiabatic evolution may be used to trigger two-photon absorption-emission

pumping cycles, which allow for on demand manipulation of individual photons in distributed quantum networks, as proposed in the cavity-QED realm [50, 53]. Demonstrating control by a Lambda configuration in last-generation artificial atoms would extend this scenario to the microwave arena, opening the perspective of performing demanding protocols in highly integrated solid-state quantum architectures [129, 35], which are usually subject to specific design constraints [131]. Examples are adiabatic holonomic quantum computation [52], information transfer and entanglement generation [80, 51, 81] between remote nodes, and other sophisticated control protocols [120].

The Lambda scheme is described by the standard Hamiltonian in the rotating-wave approximation (RWA), which has been given in Eq.(3.1), where we also introduced Rabi frequencies for the pump and Stokes field and the detunings, in particular the two-photon detuning δ. The latter is a very important parameter, since for $\delta = 0$ the system admits an exact dark state given in Eq.(3.2) that allows to observe STIRAP (see Sec. 3.2), a benchmark for multilevel advanced control whose robustness against imperfections and disorder combined with decoherence figures of last generation superconducting artificial atoms may allow to develop new protocols [120, 121] with important applications in hybrid networks, composed of many artificial atoms or microscopic spins interacting with quantized modes [132].

5.2 2+1 STIRAP in superconducting Artificial Atoms

As we thoroughly discussed in chapter 3, Λ-STIRAP could be observed by breaking the symmetry of the device [98, 56], but at the expenses of an increased noise level. Analysis of the case study (Sec. 3.4) of a the Cooper pair box has shown that efficiency, i.e. the final population of the target state $|1\rangle$, does not exceed $\gtrsim 70\%$ (see Fig. 3.3).

In order to design an effective Lambda scheme, i.e. allowing efficient coupling at symmetry, where decoherence times are large, we first replace the direct pump pulse by a two-photon process, which yields overall the "2+1" Lambda scheme [see Fig.5.1(a)]. This configuration is however known to lack robustness against fluctuations of the parameters [133, 134, 135, 53]. To overcome this problem we supplement the "2+1" Lambda scheme by suitable advanced control, which turns out to be the key ingredient for achieving both $\sim 100\%$ population transfer efficiency and robustness. We address two classes of last-generation artificial atoms, based on the "flux-qubit" [77, 2] and on the "transmon" [74, 3] design,
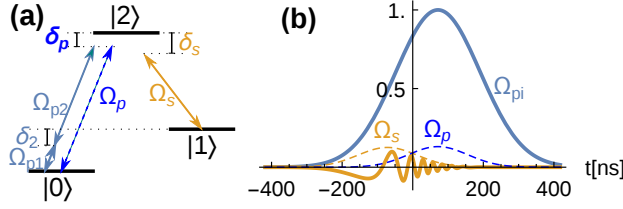
Figure 5.1: (a) A three-level system with splittings $\omega_{ij} := E_j - E_i$ driven by two quasi resonant ac pump (Ω_p) and Stokes (Ω_s) fields, in the usual Lambda scheme ($\omega_p := \omega_{02} - \delta_p$, $\omega_s = \omega_{12} - \delta_s$). In 2+1 STIRAP the pump is operated by two pulses Ω_{pk} at frequencies $\omega_{p1} := \omega_{01} - \delta_2$, $\omega_{p2} = \omega_{12} - \delta_p + \delta_2$ such that $\omega_{p1} + \omega_{p2} = \omega_{02} - \delta_p$. (b) Pulses in conventional STIRAP (dashed lines) in the counterintuitive sequence, i.e. the Stokes pulse is shined before the pump pulse. Real part of the pulses in 2+1-STIRAP (solid lines): here $\Omega_s e^{i\phi_s(t)}$ shows the phase modulated control of Eq.(5.5).

respectively.

We start our analysis from the full Hamiltonian

$$H := H_0 + H_C(t) \tag{5.1}$$

where $H_0 := \sum_j E_j \left| j \right\rangle \left\langle j \right|$ models the undriven artificial atom. The control $H_C = \mathcal{Q} \mathcal{A}(t)$ is operated by a three-tone field $\mathcal{A}(t) = \sum_{m=p1,p2,s} \mathcal{A}_m(t) \cos[\omega_m t - \phi_m(t)]$. It is coupled to the operator $\mathcal{Q}$, corresponding to the electric dipole for natural atoms. In artificial atoms it is, for instance, the charge operator in the transmon [74, 3] or the loop current in the flux qudit [77, 2]. Symmetries in the Hamiltonian H_0 imply that matrix elements $\mathcal{Q}_{ii} = \mathcal{Q}_{02} = 0$. External fields have suitable carrier frequencies (see Fig.5.1(a)) and a slowly varying modulation of the phases $\phi_m(t)$, for $m = s, p1$. Rabi angular frequencies are defined as $\Omega_{p1}(t) := \mathcal{Q}_{01}\mathcal{A}_{p1}(t)$, $\Omega_{p2}(t) := \mathcal{Q}_{12}\mathcal{A}_{p2}(t)$, $\Omega_s(t) := \mathcal{Q}_{12}\mathcal{A}_s(t)$. For simplicity we take $\delta_p = \delta_s = 0$ and equal peak amplitudes Ω_r for both the $\Omega_{pk}(t)$, where $k = 1, 2$, considering Gaussian pulses

$$\Omega_s(t) = \Omega_0 \, e^{-\left(\frac{t+\tau}{T}\right)^2}; \qquad \Omega_{pk}(t) = \Omega_r \, e^{-\frac{1}{2}\left(\frac{t-\tau}{T}\right)^2} \tag{5.2}$$

We use the delay [54] $\tau = 0.6\,T > 0$ which implements the counterintuitive sequence.

5.2.1   2+1 STIRAP in the flux qudit

Our goal is to reproduce Eq.(3.1) as an effective Hamiltonian yielding STIRAP, by properly shaping the control $\{\phi_m(t)\}$. We first consider an artificial atom with a highly anharmonic spectrum, $\omega_{12} \gg \omega_{10}$, where each transition can be selectively addressed. Therefore we can safely neglect the strongly off-resonant $\mathcal{A}_{p1}$ ($\mathcal{A}_{p2}$ and $\mathcal{A}_s$) in $\langle 1|H|2\rangle$ ($\langle 0|H|1\rangle$), and also perform the RWA. The three-level Hamiltonian in the interaction picture reads

$$
\begin{aligned}
H_3 = \frac{1}{2} \big\{ & \Omega_{p1}(t)\, \mathrm{e}^{-i\delta_2 t}\, |0\rangle\,\langle 1| + \big[\Omega_{p2}(t)\, \mathrm{e}^{i[\delta_2 t - \phi_{p2}(t)]} + \\
& + \Omega_s(t)\, \mathrm{e}^{-i\phi_s(t)} \big]\, |1\rangle\,\langle 2| \big\} + \text{h.c.}
\end{aligned}
\tag{5.3}
$$

If the two pump pulses are strongly dispersive, $|\delta_2|/\Omega_r \gg 1$, they implement an effective two-photon $|0\rangle \leftrightarrow |2\rangle$ pulse which does not populate $|1\rangle$ [54]. In this regime we derive an effective Hamiltonian from the Magnus expansion of time-evolution operator corresponding to H_3 [136] (see Appendix B).. The relevant contributions are found up to second order, which captures the coarse-grained dynamics averaged over a convenient time scale Δt such that $\Delta t\, |\delta_2| \gg 1$ but $\Delta t\, \Omega_r, \Delta t/T, \Delta t\, |\dot{\phi}_i(t)| \ll 1$ (see Appendix B). Then in the same rotating frame of Eq.(3.1) we obtain

$$
\begin{aligned}
H_{eff} = & [(\dot{\phi}_{p2} - \dot{\phi}_s) - (S_2 + 2S_1)]\, |1\rangle\,\langle 1| + \\
& + (\dot{\phi}_{p2} + S_2 - S_1)\, |2\rangle\,\langle 2| + \\
& + \frac{1}{2} \big[(\Omega_p\, |0\rangle\,\langle 2| + \Omega_s\, |1\rangle\,\langle 2|\,) + \text{h.c.} \big]
\end{aligned}
\tag{5.4}
$$

where $\Omega_p(t) = -\Omega_{p1}\Omega_{p2}/(2\delta_2)$ is the two-photon effective pump field and $S_k(t) = -\Omega_{pk}^2/(4\delta_2)$ are dynamical Stark shifts. We see that if we define $\delta_p := \dot{\phi}_{p2} + S_2 - S_1$ and $\delta := \dot{\phi}_{p2} - \dot{\phi}_s - (S_2 + 2S_1)$, Eq.(5.4) reproduces Eq.(3.1) identifying the effective Lambda system.

We now look for external control yielding STIRAP. It is convenient to take equal pulse amplitudes in H_{eff}, thereby $\Omega_0 = \Omega_r^2/(2|\delta_2|)$), and the necessary condition for adiabaticity [47] sets the time scale $T > 10/\Omega_0$. We finally adjust the system at both single and two-photon effective resonance by choosing the phase modulation according to

$$
\dot{\phi}_{p2} = S_1 - S_2 \quad ; \quad \dot{\phi}_s = -(S_1 + 2S_2)
\tag{5.5}
$$

This is a key point of our analysis: performing the latter step is crucial since
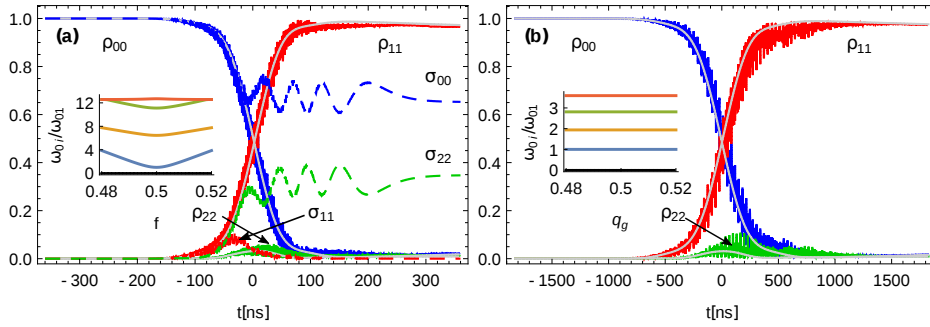
Figure 5.2: Population histories $\rho_{00}(t)$ (blue) $\rho_{11}(t)$ (red) and $\rho_{22}(t)$ (green). (a) For a flux artificial atom biased at the symmetry point $f = 1/2$ (spectrum in the inset), with the phase modulation Eq.5.5. We used $\Omega_r/2\pi = 200$MHz and $\delta_2 = -5\Omega_r$, for the two-photon pump, yielding $\Omega_0 = |\Omega_r/2\delta_2| = 20$MHz. Good adiabaticity, $\Omega_0 T = 15$, is obtained with $T = 0.12\,\mu$s and $\tau = 0.6\,T$. Results refer to the device Ref. [2] and account for leakage and effects of noise. In the absence of phase modulation, population histories σ_{ii} in the absence of decoherence (dashed lines) show no population transfer. (b) Same results for a transmon (spectrum in the inset) with phase modulation Eq. (5.12). Here $\Omega_0 = 3.9\,$MHz from Eq.(5.10), $T = 0.6\,\mu$s and $\tau = 0.6\,T$. For both designs the approximate effective dynamics (gray thin lines above the exact population histories), obtained respectively from Eq.(5.4) and Eq.(5.9), reproduces remarkably well the coarse grained time-evolution.

STIRAP would fail otherwise [see Fig.5.2(a), dashed lines]. Indeed the dynamical Stark shifts $S_k(t)$ are of the same order of the effective coupling $\Omega_p(t)$. Therefore if uncompensated they would determine large stray detunings, in particular $\delta(t) = -(S_2 + 2S_1)$ would destroy the dark state.

The phase modulation in Eq.(5.5) is obtained in closed form as a function of the pulse envelopes $\mathcal{A}_m(t)$ by a simple integration. Inserted in the control of the full Hamiltonian Eq.(5.1) it yields the goal we set, namely $\sim 100\%$ efficiency is recovered [see Fig.5.2(a), solid lines].

An important point is that solutions $\phi_m(t)$ of interest are slowly varying, consistent with our assumption. This is also clear from in Fig.5.1(b), where the modulation of the Stokes pulse for equal Ω_{pi}s, i.e. $S_1 = S_2$, is shown. It is worth stressing the remarkable agreement between the full dynamics and the approximation by H_{eff} (gray lines in Fig.5.2), which we will use later to estimate appropriate figures for Ω_r, Ω_0 and T.

Noise sources coupled via the operator $\mathcal{Q}$ are usually the most detrimental for decoherence. Effects of low-frequency noise from this "port" can be suppressed by designing a Hamiltonian with suitable symmetries, a strategy that has yielded very large decoherence times in last-generation superconducting qubits. On the other hand high-frequency fluctuations from the $\mathcal{Q}$-port are the relevant sources of quantum Markovian noise. Pure dephasing is due to residual non-Markovian noise from sources coupled to operators orthogonal to $\mathcal{Q}$. The impact of noise is studied using a phenomenological picture [45, 43] (see also Sec. 2.2), accounting for both Markovian and non-Markovian relevant noise sources. Markovian quantum noise is described by a "dissipator" $\mathcal{L}_D$ in a Master Equation of the Lindblad form

$$\dot{\rho}(t|\tilde{\mathbf{x}}) = -i[H(\tilde{\mathbf{x}}(t)), \rho(t|\tilde{\mathbf{x}})] + \mathcal{L}_D \rho(t|\tilde{\mathbf{x}}) \tag{5.6}$$

whose solution has to be averaged over a stochastic process $\tilde{\mathbf{x}}(t)$ describing individual realizations of the non-Markovian classical noise. For noise with $\sim 1/f^\alpha$ low-frequency spectrum the leading effect is captured by retaining only the contribution of quasistatic stray bias $\tilde{\mathbf{x}}(t) \to \tilde{\mathbf{x}}$ of the artificial atom [45, 43], with a suitable Gaussian distribution. In this picture stray bias determine fluctuations of energies ΔE_i and of matrix elements $\Delta \mathcal{Q}_{ij}$, which translate respectively in fluctuations of the detunings $\tilde{\delta} = \Delta(E_1 - E_0)$ and $\tilde{\delta}_p = \Delta(E_2 - E_0)$ and of the Rabi frequency $\tilde{\Omega}_0$. Only the former turn out to be important [54, 48], thereby Eq.(5.6) reduces to the structure $\dot{\rho} = i[\rho, H(\delta, \delta_p)] + \mathcal{L}_D \rho$, where detunings undergo correlated fluctuations $(\tilde{\delta}, \tilde{\delta}_p)$ induced by $\tilde{\mathbf{x}}$, the full dynamics emerging from proper

averaging.

In practical cases a single additional port must be considered, with associated stray bias $\tilde{x}$. Then fluctuations have a simple linear correlation $\tilde{\delta}_p(\tilde{x}) = a\,\tilde{\delta}(\tilde{x})$, where a is determined by the parametric dependence of the spectrum on $\tilde{x}$ (See Sec. 5.A for details). In this case experiments characterizing the *qubit* dynamics yield all the needed statistical properties of $(\tilde{\delta}, \tilde{\delta}_p)$, since the standard deviation of $\tilde{\delta}$ is $\sigma_\delta = \sqrt{2}/T_2'$, where $1/T_2' := 1/T_2^* - 1/(2T_1)$ is the qubit non-Markovian pure dephasing rate [43] and T_1 the qubit relaxation time. The multilevel dynamics is obtained by averaging over a Gaussian distribution, $p(\tilde{\delta}) = (2\pi\sigma_\delta^2)^{-1/2}e^{-\tilde{\delta}^2/(2\sigma_\delta^2)}$, the solution $\rho(t|\tilde{\delta}, a\tilde{\delta})$ of Eq.(5.6). We use the Markovian dissipator

$$
\begin{aligned}
\mathcal{L}_D \rho = & -\frac{1}{2T_1}([|1\rangle\langle 1|, \rho] - 2|0\rangle\langle 1|\rho|1\rangle\langle 0|) + \\
& -\frac{k}{2T_1}([|2\rangle\langle 2|, \rho] - 2|1\rangle\langle 2|\rho|2\rangle\langle 1|)
\end{aligned}
\tag{5.7}
$$

accounting for the two allowed transitions in the lowest three levels. We assume that $\mathcal{L}_D$ does not depend explicitly on $\tilde{\mathbf{x}}$, and we retain only spontaneous decay, which is the only relevant process at low enough temperature [48]. The constant $k \simeq [Q_{21}/Q_{10}]^2\, S(E_2 - E_1)/S(E_1 - E_0)$ depends essentially on the design of the device and, in a much weaker way, on the power spectrum $S(\omega)$, which is often ohmic at the relevant frequencies [43].

In Fig. 5.2(a) we present results for the four-junctions SQUID of Ref.[2]. They show that Λ-STIRAP with $\sim 100\%$ efficiency is obtained using $T \simeq 0.12\,\mu$s. We simulate the dynamics for the lowest six states of the full device Hamiltonian H_0, verifying that leakage from the three-level subspace is negligible ($\sum_{j\geq 3} \rho_{jj} < 2 \times 10^{-4}$). For this device relaxation ($T_1 = 12\,\mu$s [2]) and the associated Markovian dephasing are due to flux noise, whereas critical current and charge noise determine non-Markovian fluctuations, yielding the overall $T_2^* = 2.5\,\mu$s. We find the remarkable $\gtrsim 97\%$ efficiency, which is essentially limited by T_1 only.

5.2.2   2+1 STIRAP in the transmon

We now turn to artificial atoms based on the transmon design [137, 74] (see Sec. 2.1.2). Successful implementation of Λ-STIRAP in this class of devices would be very important, since they display the largest decoherence times observed so far [3, 75], and offer the perspective of fabricating highly integrated architectures [129, 35], with a rich arena of applications. These artificial atoms have a nearly harmonic spectrum [inset of Fig.5.3(b)], quantified by $\alpha := \omega_{12} - \omega_{01}$ and

$\beta := \omega_{23} - \omega_{12}$ for the four lowest energy levels. Values of $|\alpha| \simeq |\beta| \lesssim \omega_{01}/10$ ensure very large decoherence times, at the expenses however of limiting selectivity in addressing the desired transitions with strong fields. Harmonicity is a severe drawback for operating STIRAP and indeed the protocol outlined for flux-based artificial atoms would fail in the transmon. In order to find the proper effective Hamiltonian we must: (a) include selected off-resonant terms of the control, relaxing the quasi-resonant approximation; (b) consider explicitly a fourth level $|3\rangle$ since it will determine Stark shifts which must be accounted for. We neglect the coupling to the cavity used in the transmon as a measuring apparatus and at this stage we also assume the RWA, so we consider the Hamiltonian $H = H_3 + \tilde{H}$ in the interaction picture, with extra terms

$$\begin{aligned} \tilde{H} = \Big\{ &\frac{1}{2} \mathcal{A}_{p1} e^{-i(\delta_2+\alpha)t} \big[\mathcal{Q}_{12} |1\rangle \langle 2| + \mathcal{Q}_{23} e^{-i\beta t} |2\rangle \langle 3| \big] \\ &+ \frac{1}{2} \mathcal{A}_{p2} \, e^{i\delta_2 t} \big[\mathcal{Q}_{01} e^{i[\alpha t + \phi_{p2}(t)]} |0\rangle \langle 1| \\ &+ \mathcal{Q}_{23} \, e^{-i[\beta t - \phi_{p2}(t)]} |2\rangle \langle 3| \big] + \text{h.c.} \Big\} \end{aligned}$$

(5.8)

The stray $\tilde{H}$ produces non negligible effects due to the fact that anharmonicities $|\alpha|, |\beta|$ are small and large $\mathcal{A}_{pk}$ are needed to yield a sufficient effective dispersive pump drive. Since $\mathcal{A}_s$ needs not to be large, the corresponding terms can be neglected. A convenient choice of parameters turns out to be $|\delta_2| \gtrsim |\alpha|, |\beta|$. In this regime we obtain the following three-level effective Hamiltonian in the rotating frame

$$\begin{aligned} H_{eff} = &\Big(\frac{\Omega_p}{2} |0\rangle \langle 2| + \frac{\Omega_s}{2} |1\rangle \langle 2| + \text{h.c.} \Big) \\ &+ \sum_{k, i \neq j} S_{ji}^k |i\rangle \langle i| + \dot{\phi}_{p2} |1\rangle \langle 1| + (\dot{\phi}_{p2} - \dot{\phi}_s) |2\rangle \langle 2| \end{aligned}$$

(5.9)

where the effective pump coupling is now

$$\Omega_p = -\frac{\Omega_{p1}\Omega_{p2}}{4\delta_2} \frac{\alpha}{\alpha + \delta_2}$$

(5.10)

and the dynamical Stark shifts of level j due to the coupling to level i under the action of the pk field is given by

$$S_{ij}^k(t) := \left| \frac{\mathcal{A}_{pk}(t)\mathcal{Q}_{ij}}{2} \right|^2 \left(\frac{1}{\omega_{ij} - \omega_{pk}} + \frac{1}{\omega_{ij} + \omega_{pk}} \right)$$

(5.11)

This antisymmetric form for $i \leftrightarrow j$ accounts also for Bloch-Siegert shifts, which are however small in all cases treated in this chapter. Notice that Eq.(5.9) includes three levels since levels $i > 2$ only yield Stark shifts. We again let $\delta_p = \delta = 0$, thereby in order to obtain large STIRAP efficiency we modulate phases according to

$$\dot{\phi}_{p2} = \sum_{k,j} (S_{j0}^k - S_{j2}^k) \; ; \quad \dot{\phi}_s = \sum_{k,j} (S_{j1}^k - S_{j2}^k) \tag{5.12}$$

If we now use this modulation in the full Hamiltonian Eq.(5.1) we recover $\sim 100\%$ efficiency [see Fig. 5.2(b)]. Again the full dynamics is remarkably well approximated by the Magnus expansion. Results refer to the transmon of Ref.[3] and account for both leakage and effects of noise. Coherence is again essentially limited by $T_1 = 70\,\mu$s, thereby noise has negligible effects, also allowing for multiple STIRAP-like cycles.

Notice that Eq.(5.10) implies that the effective peak Ω_p saturates to the value $-\alpha/2(\delta_2/\Omega_r)^2$, for increasing Ω_r at constant $\delta_2/\Omega_r \gg 1$ [see Fig.5.3(a)]. For this reason the duration of the protocol for the transmon $[T = 0.6\,\mu$s in Fig.5.2(b)] is larger than for the flux-based artificial atom. More generally, shining larger external fields to shorten the protocol is useful only to some extent [see Fig.5.3(a)], but in devices with the largest coherence times this is not a limitation.

Robustness of the protocol is a crucial issue, since the success of conventional STIRAP lies in the striking insensitivity to small variations of control parameters. In the early proposal of "2+1" $\Lambda-$STIRAP, lack of efficiency due to the stray dynamical Stark-shift was cured by using fields with a small static two-photon detuning [133, 134, 135], but unfortunately the resulting protocol was not robust [53]. Instead our control scheme is tailored to guarantee the same robustness of conventional STIRAP. In Fig.5.3(b) we show sensitivity against fluctuations of the detunings of phase modulated STIRAP in the trasmon, which is potentially the most unfavourable case. For the example shown, frequency fluctuations of the microwave fields $\lesssim 1\,$MHz still guarantee $\gtrsim 95\,\%$ efficiency. This important result would be hardly attainable for natural atoms driven at optical frequencies [133, 134, 135, 53], where the available phase control is limited. In addition phase modulated 2+1 STIRAP is naturally resilient to non-Markovian noise inducing slow fluctuations of the energy splittings. This corresponds to fluctuating detunings, correlated as $\tilde{\delta}_p = 2\,\tilde{\delta}$ in the transmon of Ref. [3]. The part of this line contained in the high efficiency region of the $(\tilde{\delta}, \tilde{\delta}_p)$ plane corresponds to $T_2' \sim 1\,\mu$s, which sets a figure for the resilience of the protocol to non Markovian dephasing. Quite interestingly a suitably asymmetric drive with
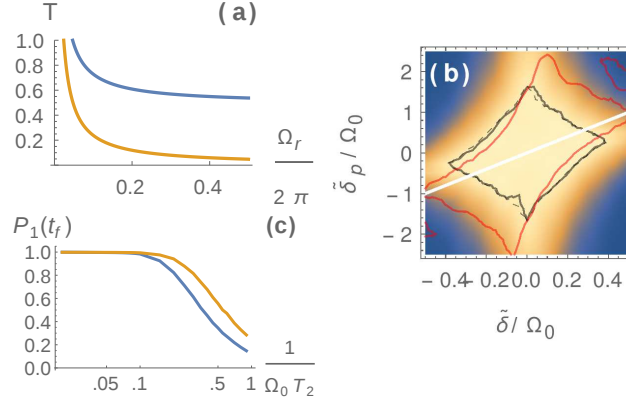
Figure 5.3: Parametric robustness of the protocol. (a) Effective duration of the protocol $T = 15/\Omega_0$ (μs units) vs $\Omega_r/2\pi$ (GHz units) for the transmon of Ref. [3] (Eq.(5.10), upper curve) and for the flux-qudit of Ref.[2] (limit $\alpha \gg \delta_2$, lower curve), at fixed $|\delta_2|/\Omega_r = 5$. (b) Efficiency versus stray detunings $\tilde{\delta}, \tilde{\delta}_p$ for the transmon design, showing the robustness of the protocol Eq.(5.12). The solid black inner curve encloses the region of efficiency $> 95\%$; results of the approximation H_{eff}, Eq.(5.9) are also reported (dashed curve) which show again the remarkable accuracy of the effective theory. The white straight line $\tilde{\delta}_p = 2\tilde{\delta}$ represents the correlated quasitatic fluctuations of the stray detunings. The red outer curve encloses the $> 95\%$ efficiency area for $r = 2$: it is seen that robustness along the line further increases using $r > 1$. (c) Efficiency vs T_2 for the transmon, $r = 1$ (lower line) and $r = 2$ (upper line).

ratio $r := \mathrm{Max}[\Omega_p(t)]/\mathrm{Max}[\Omega_s(t)] > 1$ enlarges the stability region in a way that low-frequency correlated noise affecting the device is dynamically decoupled [see also Fig.5.3(c)].

5.3 Conclusions

In summary we have shown how to design reliable multilevel control in Lambda configuration by 2+1 STIRAP. The key ingredient is a new control scheme which uses pulses with suitable slowly-varying modulated phases, Eqs.(5.5,5.12). We obtained a unique strategy allowing to operate with last generation artificial atoms, where symmetries enforce selection rules preventing a resonant pump field to be coupled directly. It can be easily implemented in such devices with available microwave electronics [58], yielding $\sim 100\%$ efficiency. It is worth stressing that phase control is necessary to guarantee the important property of robustness to the same level of conventional STIRAP.

We finally mention that STIRAP has been very recently observed in the so

called Ladder configuration [138, 139], which is more easily implemented in last-generation artificial atoms. It involves a two-photon absorption process, whereas Λ-STIRAP implements a coherent absorption-emission cycle. This latter is a fundamental building block for advanced control in highly integrated architectures, thereby it would have an impact on applications. Phase control exalts in a natural way the advantages of last-generation superconducting artificial atoms, where it opens new perspectives for advanced quantum control. Our work may be extended in these directions using optimal control theory tools.

5.A   Noise figures evaluation and model

In evaluating the dynamics of the artificial atoms, we made use of the model of Sec. 2.2. An emerging important qualitative issue, as we shall argue below, is that noisy three-level dynamics is fully characterized by decoherence in the "trapped" (or qubit) subspace only, plus information on the Hamiltonian of the device alone, a results also obtained conventional STIRAP [48]. Indeed stray bias due to low-frequency noise determine fluctuations of energies ΔE_i and of matrix elements $\Delta \mathcal{Q}_{ij}$. They translate respectively in fluctuations of the detunings $\delta = \Delta E_1 - \Delta E_0$ and $\delta_p = \Delta E_2 - \Delta E_0$ and in fluctuations of the Rabi frequency $\tilde{\Omega}_0$. The sensitivity to such parameters has been extensively studied [54]: while fluctuations $\tilde{\Omega}_0$ are irrelevant for STIRAP, fluctuations of detunings are important. Therefore the relevant open system dynamics turns out to be described by a Lindblad Master Equation with the structure $\dot{\rho} = i[\rho, H(\delta, \delta_p)] + \mathcal{L}_D \rho$ where H depends on fluctuations (δ, δ_p) induced by stray bias $\tilde{\mathbf{x}}$. In Fig. 5.3(b) we plot the efficiency of the protocol vs stray (δ, δ_p): efficiency is large if fluctuations do not let the system diffuse out of the central diamond region. In particular, the protocol is critically sensitive to fluctuations of the two-photon detuning δ, i.e. of the "qubit" splitting $E_1 - E_0$.

Concerning quantum noise, $\mathcal{L}_D \rho$ includes in principle the various decay rates and associated excitation and secular dephasing processes, but in practice again the "qubit" spontaneous decay only has to be accounted for, i.e. the only relevant term turns out to be $\mathcal{L}_D \rho = -\frac{1}{2T_1}([\sigma_+\sigma_-, \rho] - 2\sigma_-\rho\sigma_+)$ where $1/T_1$ is the spontaneous decay rate of the qubit, and the Lindblad operators are the corresponding lowering and raising operators $\sigma_- = \sigma_+^\dagger = |0\rangle\langle 1|$. Indeed selection rules suppress $2 \leftrightarrow 0$ processes, whereas we have estimated the decay rate $\Gamma_{2\to 1} = k/T_1$, where $k = O(1)$ depends on features of the device, and directly checked that in the devices of interest it had no impact on the results. This is due to the fact that $|2\rangle$
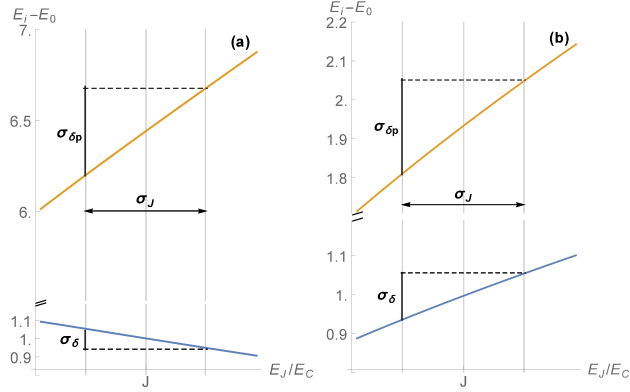
Figure 5.4: Bohr frequencies $E_1 - E_0$ (lower coloured curve) and $E_2 - E_0$ vs E_J/E_C (upper coloured curve) around a bias point J for a flux qudit (a) and a transmon (b). It is seen that Bohr frequencies vary linearly with respect to the fluctuating parameter E_J/E_C. Variances σ_δ and σ_{δ_p} are indicated in correspondence of a noise variance σ_J. Correlation of detuning fluctuations, i.e. $\delta_p = a\delta$, is determined through $a = [\partial(E_2 - E_0)/\partial(E_J/E_C)]/[\partial(E_1 - E_0)/\partial(E_J/E_C)]$, where the derivative is evaluated at the bias point J.

is depopulated when STIRAP is successful. The same holds true for field induced absorption, since Ω_s (Ω_{pk}) act when $|1\rangle$ ($|0\rangle$) are depopulated. Notice finally that we did not include in the dissipator extra pure dephasing terms since they are accounted for by the average over non-Markovian quasistatic fluctuations.

We now briefly discuss how figures of noise can be extracted from experiments on qubits, referring to the flux qudit of Ref. [2]. The dominant source of decoherence is flux noise. The low-frequency part of its spectrum $S_\Phi(\omega)$, though, has minimal effect since at the symmetry point $f = 1/2$, energy fluctuations are *quadratic* in the small corresponding stray bias $\tilde{x}_1(t) = \tilde{f}(t)$. Instead its high-frequency components determine the qubit $T_1 = 12\,\mu$s and the rate $\Gamma_{2\to1}$. For this latter we estimated $k = [Q_{21}/Q_{10}]^2 \, [S_\Phi[(E_2 - E_1)/\hbar]/S_\Phi[(E_1 - E_0)/\hbar] \lesssim 1$, taking for $S_\Phi(\omega)$ the linear behavior observed for quantum noise [2], and verified that it does not affect the dynamics. Subdominant noise sources for flux qudits are critical current and charge noise. They do not produce relaxation at the symmetry point, but they are the main source of non-Markovian pure dephasing. The induced energy fluctuations are *linear* in the corresponding stray bias $\tilde{\mathbf{x}}(t)$ (see Fig.5.4), determining Gaussian suppression of the qubit coherence [43]. The power spectrum $S_\mathbf{x}(\omega) \sim 1/\omega$ has been measured from the qubit dynamics, over several frequency decades [2]. Therefore we can safely use the SPA result for the qubit coherences decay $\propto \mathrm{e}^{-\sigma_\delta^2 t^2/2}$ and extract from the measured non-Markovian

qubit pure dephasing rate $1/T_2' := 1/T_2^* - 1/(2T_1)$ the variance $\sigma_\delta = \sqrt{2}/T_2'$ of the two-photon detuning in STIRAP. Fluctuations of δ_p, i.e. of $E_2 - E_0$, are easily found from the parametric dependence on the external bias of the calculated spectrum of the device (see Fig.5.4). Notice that since each source of noise induces a single stray bias $\tilde{x}_i$, fluctuations of detunings are correlated. For highly noise-protected devices subdominant noise sources induce fluctuations $\delta_p = a\delta$. The constant a depends on the band structure of the device (see Fig. 5.4) and in particular $a = -4.5$ in the flux qudit of Ref. [2] refers to critical current and charge noise.

Similar considerations hold for the transmon of Ref. [3]. In the transmon $a \simeq 2$ and $k \simeq 2$. Low-frequency charge noise is suppressed by both symmetry and the presence of the big shunt capacitance that reduces sensitivity to charge fluctuations. Subdominant noise as flux and critical current noise lead to pure dephasing $1/T_2'$, which is very small.

Numerics have been carried out through a Montecarlo quantum jump approach accounting for Markovian noise, by averaging over 10^4 trajectories. Non-Markovian noise has been taken into account by a further average: we impose $\delta_p = a\delta$ and sample δ from its Gaussian distribution for each trajectory. Variances we used are $\sigma_\delta = 4.1 \times 10^{-3} \, \Omega_0 = -0.22 \, \sigma_{\delta_p}$ for flux qubit ($\Omega_0 = 20 \, \text{MHz}$) and $\sigma_\delta = 2 \times 10^{-4} \, \Omega_0 = 0.5 \, \sigma_{\delta_p}$ in the transmon. By inspection of Fig.5.3(b) it is clear that STIRAP in highly noise-protected devices is robust against such low frequency fluctuations.

Chapter 6

Ultrastrong coupling probed by Coherent Population Transfer

We propose a protocol to achieve dynamic detection of Ultra Strong Coupling effects between an artificial atom and a mode of a resonator by means of coherent population transfer. Following results from the recent literature [140, 141], we study a Lambda configuration and propose a STIRAP protocol. We show that, in spite of high transfer efficiency attainable, the Lambda configuration allows transfer paths not uniquely imputable to the Ultra Strong Coupling regime. We address this issue by considering a Vee configuration and show how high efficiencies can be non ambiguously linked to breakdown of the Rotating Wave Approximation. Simulations with state of the art flux qutrits are shown and possible sources of imperfections in experiments are addressed.[1]

6.1   Introduction

Understanding light-matter interaction and the fundamental physics behind it is fundamental for the development of new quantum technologies. Strong coupling between atoms and electromagnetic modes, as described by the Jaynes-Cummings (JC) model of quantum optics [142], has been observed in several physical systems. In particular, for solid-state artificial atom architectures [118, 75, 35], small cavity volumes and large dipoles make easy to engineer values of the light-matter coupling constant $g \sim 1\%$ of the cavity angular frequency ω_c and the atomic

---

[1]The content of this chapter has been adjusted, with minor modifications, from A. Ridolfo, P.G. Di Stefano, E. Paladino and G. Falci, Ultrastrong coupling probed by Coherent Population Transfer, in preparation.

relevanto Bohr frequency ε. Coupling is large enough to determine strong coupling, i.e. to overcome decoherence rates of both the cavity and the artificial atom, $g > \kappa, \gamma$ [137, 36, 118]. Fabrication techniques have recently allowed to go beyond, entering the regime of ultrastrong coupling (USC) [143], where $g \sim \omega_c, \varepsilon$ [144]. In this regime the so called rotating wave approximation (RWA) breaks down, and light and matter experience non-perturbative physics previously unexplored experimentally. So far spectroscopic signatures of the breakdown of the RWA, as the Bloch-Siegert shift, have been detected in superconducting [4, 145, 146, 147] and semiconducting [144, 148, 149] systems. In the recent literature, dynamical detection of USC by spontaneous emission pumping (SEP) [140] and by Raman oscillations [141] have been proposed. This is also the subject of this work, where we propose that coherent amplification of population transfer by STIRAP [47, 54] could be a unique strategy to achieve a "smoking gun" dynamical signature of USC in state-of the art solid-state systems. Despite several dynamics effects have been predicted [143, 150] and interesting applications as the parametric generation of nonclassical states have been foreseen [151], control in time beyond the RWA is still little developed [148]. Demonstration of coherent dynamics in the USC regime would be a benchmark for advances in quantum control in the USC regime, with appealing perspectives in the field of dynamical quantum phase transitions [152].

The USC regime between a two-level atom, with states $\{|g\rangle, |e\rangle\}$ and energy spitting ε, and a quantized mode is described by the Rabi Hamiltonian

$$
\begin{aligned}
H_{R2} = {} & \varepsilon \, |e\rangle \langle e| + \omega_c \, a^\dagger a + g \big(a^\dagger \, |g\rangle \langle e| + a \, |e\rangle \langle g| \big) \\
& + g \big(a \, |g\rangle \langle e| + a^\dagger \, |e\rangle \langle g| \big)
\end{aligned}
\tag{6.1}
$$

The JC Hamiltonian results from neglecting the last "counterrotating" term, which can be done if $g, |\varepsilon - \omega_c| \ll \varepsilon, \omega_c$, as in atomic physics. Architectures of artificial atoms and quantized modes can be fabricated with larger $g/\omega_c \sim 0.1 - 1$, entering the USC regime described by the complete H_{R2}. The counterrotating term induces signatures in the spectrum $\{E_j\}$ such as the Bloch-Siegert shift [see Fig. 6.1(a)], which has been spectroscopically detected in experiments. The structure of the eigenstates can be drastically altered by USC, since the typical JC states with doublets of definite number of excitations, are mixed by the couterrotating term. Therefore eigenstates of H_{R2} have the generic form $|\Phi_j\rangle = \sum_{n=0}^{\infty} c_{jn} \, |ng\rangle + d_{jn} \, |ne\rangle$, with the only constraint that the parity of the number of excitations is well defined (see Sec. 2.1.4). In particular, the ground state $|\Phi_0\rangle$, which in the JC model is factorized in the zero photon state and the
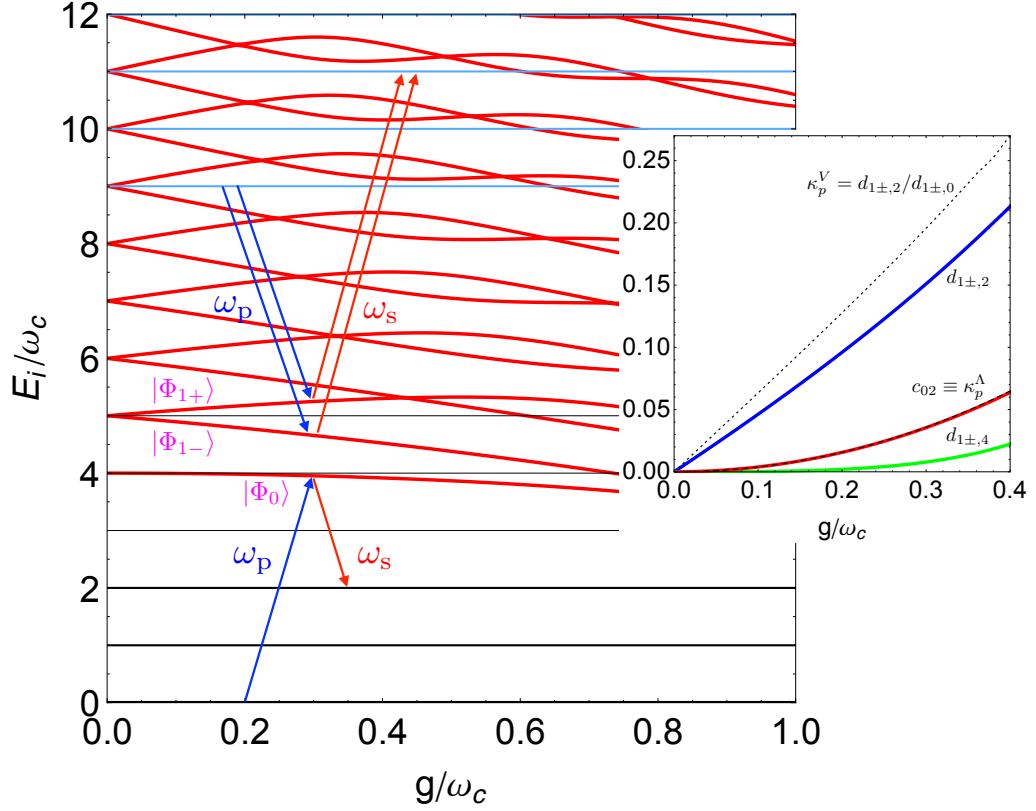
Figure 6.1: (color online) Spectrum $\{E_i\}$ of the Rabi Hamiltonian Eq.(6.1) at resonance $\varepsilon = \omega_c$, from strong coupling to the USC regime (thik red lines): for small g/ω_c energies are linear in g, as in the JC model, deviations from linearity yield the Bloch-Siegert shift, marking the USC regime. Thin black lines refer to factorized states $|n\,a\rangle$ of the cavity with an ancillary atomic level, Eq.(6.2) at a lower energy $\epsilon_a =: -\varepsilon'$; two of these states are coupled to $|\Phi_0\rangle$ by resonant pump (ω_p) and Stokes (ω_s) lasers in Lambda configuration. Thin dashed black lines represent extra levels when $|a\rangle$ has higher energy $\epsilon_a = \varepsilon + \varepsilon'$, and the possible driving schemes in the Vee configuration. In the inset, amplitudes of the eigenstates $|\Phi_j\rangle$ of the Rabi model relevant for our work, $c_{02}(g) = \langle 2g|\Phi_0\rangle$ and $d_{1\pm,2} = \langle 2\,e|\Phi_{1\pm}\rangle$, The quantities $\kappa_p^{\Lambda,V}$ represent the attenuation of the external pump field, needed to attain the range of best efficiency and robustness of STIRAP.

atomic ground state $|0\,g\rangle$, acquires components with a finite number of photons, corresponding to non-vanishing c_{0n} for n even and d_{0n} for n odd. Proposals of dynamical detection of USC [140, 141] leverage on this property. A third ancillary atomic level $|a\rangle$ is considered, at a lower energy $-\varepsilon' < 0$, and assuming that the corresponding transitions are far detuned $\varepsilon' \gg \omega_c$ the Hamiltonian becomes

$$H_0 = -\varepsilon'\,|a\rangle\,\langle a| + H_{R2} + \omega_c\,a^\dagger a \otimes |a\rangle\,\langle a| \tag{6.2}$$

In SEP [54] population is pumped from $|0a\rangle$ to $|\Phi_0\rangle$, which may decay in $|2a\rangle$, due to the finite overlap $c_{02} = \langle 2g|\Phi_0\rangle \neq 0$. This is impossible in the presence of JC coupling only, thereby detection of this channel, uniquely leaving two photons in the cavity, is a "smoking gun" of USC [140]. This process has however very low efficiency, since in most of the present implementations of USC architectures c_{02} is very small, and the transfer probability depends on $|c_{02}|^2$. In this paper we propose to amplify coherently this channel implementing population transfer by STIRAP [54, 53]. Contrary to SEP, STIRAP is based on quantum interference, allowing to reach the desired target state with efficiency $\sim 100\%$.

6.2   Λ-STIRAP

The artificial atom is driven by a two-tone external control field, $W(t) = \sum_{k=p,s} \mathscr{W}_k(t) \cos \omega_k t$, with slowly varying envelopes $\mathscr{W}_k(t)$. For illustrative purposes we assume that the artificial atom's spectrum is highly anharmonic $\varepsilon' \gg \varepsilon$ and take $\omega_k \sim \varepsilon'$. Therefore the control mainly addresses the lowest atomic states, and it is effectively described by

$$H_c(t) = W(t) \left(|a\rangle \langle g| + |g\rangle \langle a| \right)$$
$$= W(t) \sum_{nj} c_{jn} \left(|n\,a\rangle \langle \Phi_j| + |\Phi_j\rangle \langle n\,a| \right).$$

If we choose $\omega_p \approx E_0 + \varepsilon'$ and $\omega_s \approx E_0 + \varepsilon' - 2\omega_c$, and assume not too strong fields $\mathscr{W}_k \ll \omega_k$, and not too large g, then H_c further simplifies yielding the so called Lambda scheme [47, 54]

$$H_c^\Lambda(t) = \frac{\Omega_p(t)}{2} \mathrm{e}^{i\omega_p t} |0\,a\rangle \langle \Phi_0| + \frac{\Omega_s(t)}{2} \mathrm{e}^{i\omega_s t} |2\,a\rangle \langle \Phi_0| + \mathrm{h.c.}$$

where $\Omega_p = c_{00}\mathscr{W}_p$ and $\Omega_s = c_{02}\mathscr{W}_s$ are the Rabi frequencies associated to the pump and Stokes fields respectively. Under these assumptions the relevant dynamics is restricted to three levels, and it is described by the projected $H_3 = -\varepsilon' |0a\rangle \langle 0a| + (2\omega_c - \varepsilon') |2a\rangle \langle 2a| + E_0 |\Phi_0\rangle \langle \Phi_0| + H_c^\Lambda(t)$, which is the standard Hamiltonian for Λ-STIRAP[47, 54]. Preparing the system in $|0a\rangle$ and shining two pulses of width T in the counterintuitive sequence (the Stokes pulse *before* the pump pulse) yields $\sim 100\%$ population transfer to $|2a\rangle$. This effect results from the adiabatic evolution of a dark state, stabilized by destructive interference of the drives. Adiabaticity is obtained using large pulse areas $\max_t[\Omega_k(t)]T > 10$ for both fields. In particular, since T is limited by the dephasing time T_2, STIRAP requires appreciable USC mixing $c_{02}(g)$ to yield a large enough Stokes Rabi
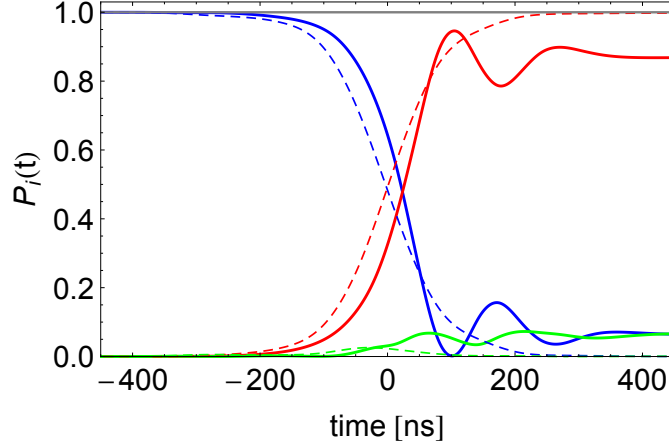
Figure 6.2: Coherent population transfer by STIRAP between $|0a\rangle$ (blue curves) and $|2a\rangle$ (red curves), via the virtual intermediate state $|\Phi_0\rangle$ (green curves), as a result of USC. Here we used a conservative value $g/\omega_c = 0.25$, $\varepsilon = \omega_c$, $\varepsilon' = 4\omega_c$ and figures of the external control $\Omega_0 = \omega_c/10$ and $\kappa_p\Omega_0 T = 20$. Using $\varepsilon/(2\pi) = 6$GHz, figures typical of flux qubits [4, 2]. For this simulation 19 states were enough and we considered coupling of the control field to all the $|a\rangle - |g\rangle$ transitions, and additional stray coupling also to the $|g\rangle - |e\rangle$ transitions. Coherent population transfer of $\sim 80\%$ is obtained (solid lines), due to partially autocompensated dynamical Stark shifts. Complete population transfer (dashed lines) can be achieved by an extra phase modulation, similar to the one shown in chapter 5, or by a suitable extra tone in $W_s(t)$. The virtual intermediate level is almost never occupied and no leakage from the three-level subspace occurs.

frequency Ω_s. In the USC regime STIRAP reaches the state $|2a\rangle$ with nearly unit probability, irrespective on g, whereas if mixing is insufficient there is no channel for population transfer to $|2a\rangle$. Therefore detection of $n = 2$ photons in the cavity after the pulse sequence is a "smoking" gun for USC.

Efficiency is larger if pulses are such that the peak Rabi frequencies are approximately equal, i.e. $\max_t[\Omega_s(t)] = \max_t[\Omega_p(t)] =: \Omega_0$ [54]. To this end, the pump field should be attenuated $\mathscr{W}_p = \kappa_p\mathscr{W}_s$, where $\kappa_p \sim c_{02}/c_{00}$. Compared to the small efficiency of SEP, STIRAP achieves unit probability provided the coupling exceeds a threshold depending on $c_{02}(g)$, thus coherently amplifying the USC channel. This effect is moreover very robust against parametric fluctuations, which is the property making STIRAP so successful in molecular physics. The key sensitivity to the two-photon detuning, $\delta = 2\omega_c - (\omega_p - \omega_s)$, still allows efficient population transfer if fluctuations are smaller than a fraction of Ω_0.

The three-level analysis must be generalized to account for the multilevel

nature of the system. No leakage from the three-level subspace occurs since the intermediate $|\Phi_0\rangle$ is almost never occupied (see Fig. 6.1). On the other hand, the control field $W(t)$ couples also to off-resonant transitions, and may produce dynamical Stark shifts [153] in view of the fact that STIRAP may require a large Stokes field $\mathscr{W}_s$. In fact the direct shift of the $a-g$ splitting determines a stray two-photon detuning $\delta(t)$ which may suppress the transfer efficiency. Fortunately the multilevel structure mitigates this effect since the dynamical Stark shifts outside the three-level subspace, tends to compensate the direct $a-g$ shift. We studied this problem considering up to 40 levels and a control field with the structure $H_c(t) = W(t)[(|g\rangle\langle a| + (1/\eta)|e\rangle\langle g|) + \text{h.c.}]$, which describes the experimentally relevant case of a ladder type "dipole" coupling to the artificial atom, also reflecting an unwanted coupling to the $g \to e$ transition. η here is the ratio between the corresponding dipole matrix elements, i.e. $\eta := \mathcal{Q}_{ea}/\mathcal{Q}_{eg}$. Results in Fig.(6.2) show that experimentally detectable population transfer is achieved also in this non-ideal case. Moreover dynamical Stark shifts can be fully compensated by appropriately crafted control, either using an additional phase modulation [153] of the fields or by adding a suitable off-resonant tone to the Stokes pulse. Of course by increasing the coupling g a large $\mathscr{W}_s$ is not needed any more and no stray detuning is induced.

6.2.1   Problems with the Lambda scheme

Coming to implementation in state-of the art physical systems one has to tackle two further problems. First of all a reliable scheme for detecting the two-photons left in the cavity is needed, which is prohibitive for THz photons as those involved in systems based on semiconductor quantum wells. Instead in superconducting artificial atoms architectures GHz-photons are produced, which can be detected with state of the art circuit-QED measurement technology. Subtile issues in photon detection in the USC regime [154] do not affect the measurement scheme with the uncoupled ancillary level $|a\rangle$. The multilevel nature of superconducting artificial atoms offers moreover a natural way to implement the proposed design. However, in real hardware the cavity is always dispersively coupled also to other transitions of the three-level artificial atom, and in particular those involving $|a\rangle$. This has a severe impact on the information gained by the simple protocol we discussed. Indeed *all* the proposals [140, 141] based on the Lambda scheme, do not allow unambiguous dynamical detection of USC in present day hardware. We will first elucidate this problem, and then we will illustrate the solution, introducing

a different STIRAP scheme showing that it provides a unique dynamical test for USC.

We consider the relevant case of a single additional stray coupling $g' = \eta g$ of the cavity to the artificial atom $a - g$ transition. The key point is that this stray coupling may open a new channel for the two-photon target state already in the RWA. Therefore detecting the cavity in the two photon state at the end of the protocol is *not* a "smoking gun" for USC anymore, as illustrated in Fig. 6.3. Insight is gained by using perturbation theory in the counterrotating g term of the Rabi Hamiltonian and in the stray g' coupling, taken in the RWA. It is seen that $|\Phi_0\rangle$ acquires a component onto $|1a\rangle$ while $|2a\rangle$ gains a component onto $|1g\rangle$, which are coupled by the Stokes field. Therefore the Rabi frequency becomes, to lowest order in g'

$$\Omega_s(t) \approx \left[c_{02} - \frac{\sqrt{2}g'^2}{(\varepsilon' - \omega_c)^2 - g'^2} \right] \mathcal{W}_s(t) . \tag{6.3}$$

The additional term indicates that a new path for population transfer opens, which interfere distructively with the USC channel, or may allow to reach the target state also for $c_{02} = 0$, i.e. when USC is absent. Notice that in any of the above cases, in practice two photons are detected in the final state, since the correction to $|2a\rangle$ due to g' is very small. Therefore STIRAP probes selectively the USC channel only if the correction in Eq.(6.3) is so small that we can choose T such that adiabatic population transfer is ensured only by the USC channel. This necessary condition can be quantified in the perturbative regime as

$$A := \frac{1}{2\eta^2} \left| \frac{\alpha^2 - (g/\varepsilon)^2}{2 - (g/\varepsilon)^2} \right| \gg 1 \tag{6.4}$$

where $\alpha := \varepsilon'/\epsilon - 1$ is the anharmonicity of the artificial atom spectrum. Notice that the two competing contributions to $\Omega_s(t)$ enter both at order g^2 the condition Eq.(6.4), which is then non trivial, and indeed it turns out that it is not met by any currently available superconducting artificial atom. Indeed, while exhibiting the largest figures of USC so far, architectures based on the flux (or persistent current) qubit [4] lack of selectivity because the stray coupling is way too strong, $\eta \gg 1$. A smaller $\eta \approx 1/\sqrt{2}$ is found in circuit QED architectures based on the transmon [74] design, which nowadays exhibit the lowest decoherence rates. However, long coherence times require small anharmonicity, $|\alpha| \lesssim 0.1$, and again selectivity is not met. Fig. 6.3 shows that selecting the USC channel only is not possible even for much more favourable figures than in state-of.the art devices.
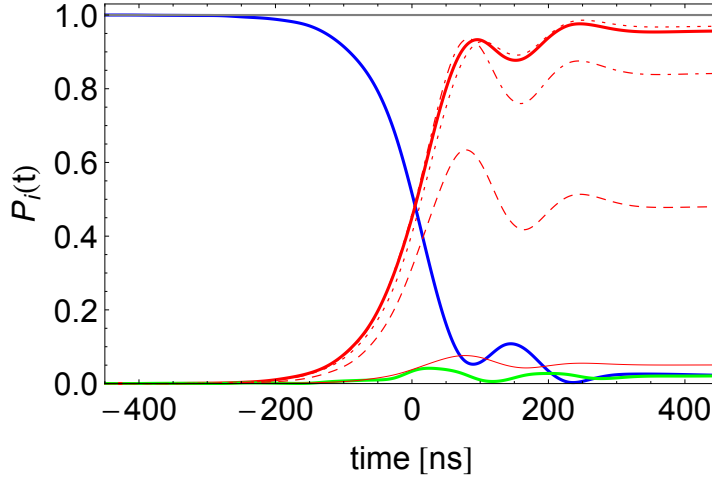
Figure 6.3: Population histories for Lambda system mimicking a favourable situation in realistic devices with $\varepsilon' = 4\varepsilon$ and $g = 0.25\omega_c$. Thick solid lines are the results for $g' = 0$ with the same color legend of Fig. 6.1. The additional red lines are the populations of the target state with values of $g' = 0.1\omega_c$ (dotted line), $g' = 0.2\omega_c$ (dot-dash line), $g' = 0.25\omega_c$ (dashed line) and $g' = 0.3\omega_c$ (solid thin line). We see how the additional channel introduced by stray $a - g$ coupling destructively interferes with the USC path, thereby determining an efficiency drop for increasing values of g'. For $g' = 0.25$ and $g = 0$ population transfer (not shown here) occurs only through the JC stray coupling even in absence of USC.

Summing up present day hardware based on semiconductors or superconductors does not allow dynamical detection of USC in the Lambda scheme.

6.3   VEE STIRAP

We now show that the above limitations can be uniquely bypassed by STIRAP in the vee (V) configuration. This is the central result of the work reported in this chapter. We consider the standard configuration of a flux qubit, the lowest energy doublet being coupled to a cavity in the USC regime. The second excited state of the artificial atom is used as the ancillary level $|a\rangle$. The Hamiltonian is now

$$H_0 = H_{AA} + H_1 + \omega_c\, a^\dagger a \qquad (6.5)$$

where $H_{AA} = \varepsilon\,|e\rangle\,\langle e| + (2 + \alpha)\varepsilon\,|a\rangle\,\langle a|$ describes the flux artificial atom, supposed to operated at an external flux bias $\Phi_x = \Phi_0/2$, $\Phi_0 = h/(2e)$ being the flux quantum. This makes H_{AA} symmetric with respect to fluctuations of Φ_x and minimizes decoherence. The corresponding selection rule forbids the

$g - a$ transitions, therefore the full coupling to the cavity reads $H_1 = g(a + a^\dagger)[(|g\rangle\langle e| + \eta|e\rangle\langle a|) + \text{h.c.}]$. We consider resonant coupling to the cavity, $\varepsilon = \omega_c$, and a control field operated via the magnetic flux coupling to both atomic transitions with $H_c(t) = W(t)[(|e\rangle\langle a| + (1/\eta)|e\rangle\langle g|) + \text{h.c.}]$. By choosing a two-tone field with proper frequencies we can exploit two-photon processes, via one of the intermediate states $|\Psi_{1\pm}\rangle$, being the two lowest excited states of the Hamiltonian (6.5). We first neglect the stray coupling of the $e - a$ transition to the cavity. Then $|\Psi_{1\pm}\rangle$ are the eigenstates of the Rabi Hamiltonian (6.1) $|\Phi_{1\pm}\rangle = d_{1\pm,0}|0e\rangle + c_{1\pm,1}|1g\rangle + d_{1\pm,2}|2e\rangle + c_{1\pm,3}|3g\rangle + \dots$, with eigenvalues $E_{1\pm}$. They reduce to the first JC doublet $|\varphi_{1\pm}\rangle = (|0e\rangle \pm |1g\rangle)/\sqrt{2}$ when the counterrotating term is switched off. Population transfer $|0a\rangle \to |2a\rangle$ by V-STIRAP requires, as before, a two-tone external field $W(t)$, but in this case we must choose $\omega_p = (1 + \alpha)\varepsilon - E_{1\pm} - \delta_p$ and $\omega_s = (3 + \alpha)\varepsilon - E_{1\pm} - \delta_s$. Insight is gained by projecting onto the three-level subspace $\text{span}\{|0a\rangle, |2a\rangle, |\Phi_{1\pm}\rangle\}$, which yields an effective three-level Hamiltonian, the control term being

$$\begin{aligned} H_c^v(t) = &\frac{\Omega_p(t)}{2}e^{-i\omega_p t}|0\,a\rangle\langle\Phi_{1\pm}| + \\ &+ \frac{\Omega_s(t)}{2}e^{-i\omega_s t}|2\,a\rangle\langle\Phi_{1\pm}| + \text{h.c.} \end{aligned} \tag{6.6}$$

with peak Rabi frequencies $\Omega_p = d_{1\pm,0}\mathscr{W}_p$ and $\Omega_s = d_{1\pm,2}\mathscr{W}_s$. In the absence of counterrotating terms $d_{1\pm,0} = \langle 0e|\Phi_{1\pm}\rangle = 1/\sqrt{2}$ and $d_{1\pm,2} = \langle 2e|\Phi_{1\pm}\rangle = 0$, thereby population transfer to $|2a\rangle$ occurs only in the USC regime.

We now evaluate the impact of stray couplings. To this end we first notice that the vee configuration in flux qubits offers both advantages of large anharmonicity $\alpha \geq 3$, and small ratio between the relevant "ladder" matrix elements, $\eta \approx 1/3$. It turns out that, contrary to the Lambda scheme, V-STIRAP provides unambiguous evidence of the USC regime. This is clear in Fig. 6.4, where we simulated the dynamics the the full Hamiltonian (6.5), using parameters of real devices, showing that population transfer efficiency $\sim 100\%$ is achieved in the USC regime of the $g - e$ coupling. On the contrary, if the counterrotating part is switched off only Rabi oscillations occurr between the exact eigenvalue $|0a\rangle \to |\Psi_{0a}\rangle$ and $|\Psi_{1\pm}\rangle$, which are due to the stray g', whereas population of the target state $|\Psi_{2a}\rangle$ is always zero. This shows that V-STIRAP selects the USC channel.

Even more than the favorable configuration of the spectrum, the striking selectivity of V-STIRAP stems from the fact that the stray coupling *does not open a new path* for population transfer in lowest order, as was the case for Eq.(6.3).

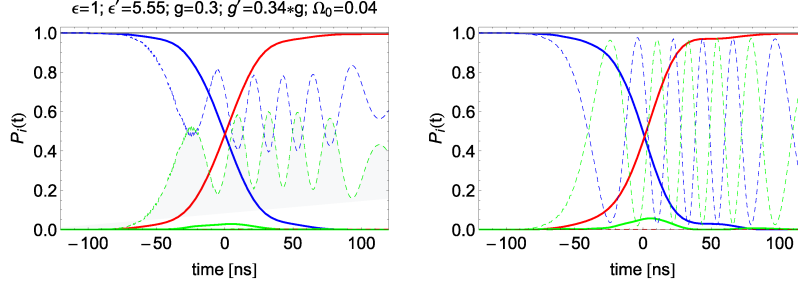$\epsilon = 1;\ \epsilon' = 5.55;\ g = 0.3;\ g' = 0.34*g;\ \Omega_0 = 0.04$

Figure 6.4: Population histories for the Vee scheme. STIRAP using $|\Phi_{1+}\rangle$ [(a), green curves] and $|\Phi_{1-}\rangle$ [(b), green curves] as linkage states is studied, yielding similar results. Solid lines are for $g = 0.3\omega_c$, $g' = g/3$, $\Omega_0 = 0.04\omega_c$, $\epsilon' = 5.55\epsilon$. Dashed lines are obtained in the RWA approximation, where no Stokes coupling is possible, henceforth only Rabi oscillations between $|0a\rangle$ and $|\Phi_{1\pm}\rangle$ can be observed.

Indeed no component of $|\Psi_{1\pm}\rangle$ on $|na\rangle$ appears at lowest order in perturbation theory, implying that leading corrections to the control Hamiltonian (6.6) due to the stray coupling g' can be ignored. In view of this observation V-STIRAP via $|\Psi_{1\pm}\rangle$ appears as a unique dynamical probe. The detection of two photons at the end of the protocol is a "smoking gun" of USC, since as before, the probability that in the final state $|\Psi_{2a}\rangle$ other values are detected is negligible, $\sim [\eta\, g/(\alpha\varepsilon)]^2 \approx 10^{-2}(g/\omega_c)^2$.

Notice that since $d_{1\pm 2}(g) > c_{0\,2}(g)$ (see. inset of Fig. 6.1), coupling the external field is much easier for V-STIRAP. Therefore sufficient adiabaticity is attained with weaker Stokes fields $\mathscr{W}_s$ and/or require shorter pulse length T. This softens the problem of stray dynamical Stark shifts, which indeed are not apparent in the simulation of Fig. 6.4. They also allow for protocols of shorter duration (compare the time axes of Fig.6.4 and Fig.6.3).

6.4   Preparation and decoherence

The protocol above we assumed that the state $|0a\rangle$ could be prepared. If $g = 0$, the artificial atom and the cavity are decoupled and $|a\rangle$ can be prepared from the ground state $|g\rangle$ by standard pulse sequences [155]. However if $g \neq 0$ the ground state is $|\Phi_0\rangle$ and the above procedure prepares a state containing an even number of photons with probability $\propto |c_{02}(g)|^2$. This is very small for not so large g, where on the other hand $d_{1\pm 2}(g)$ is large enough to guarantee almost complete population transfer by V-STIRAP, with some harmless lack of accuracy. More accurate preparation protocols may be designed [138].

Concerning decoherence, we observe that STIRAP is essentially sensitive to fluctuations in the "trapped" subspace span$\{|0e\rangle, |2e\rangle\}$ and rather insensitive to all the other decay or dephasing processes affecting the system [48]. Efficient population transfer is obtained if $T < 1/\Gamma$, where Γ is the decoherence rate in the "trapped" subspace. In high-quality devices is roughly given by the sum of the cavity decay rate κ of the and the decay rate $\gamma_{a \to e}$ of the ancillary level. In the best devices available at present these rates are very small, allowing for T of several dozens of μs. In devices used for USC spectroscopy the cavity has a much smaller quality factor, but there should be no fundamental tradeoff between large g and decoherence cavity alone, allowing the fabrication of devices exploiting the coherent dynamics in the USC regime. Alternatively large effective couplings $g_{eff} \sim \sqrt{N}g$ could be attained by using few weakly coupled artificial atoms, in the standard design allowing for $> \mu$s decoherence times. We simulated the dynamics for $N = 4$ artificial atoms, and we reproduced results of Fig.(6.4) using half of the value of g. We also checked robustness of the protocol with respect to inhomogeneities of the individual couplings of artificial atoms and against the possible presence of stray cavity modes at multiple frequencies.

6.5 Conclusions

In conclusion, we studied dynamical detection of the USC regime of light-matter superpositions. An ancillary level is used as a probe, and the coherent amplification of a USC-specific channel for population transfer, which yields a characteristic two-photon state in the cavity. Ideally this is a unique signature of the violation of the conservation of the number of excitations due to the counterrotating term in the Rabi Hamiltonian Eq.(6.1). We show how to implement such design in state of the art devices and introduce STIRAP in Vee configuration as a uniquely selective tool to demonstrate unambiguously dynamics due to USC. Flux qubits, besides being the physical systems with the largest figures of $g/\omega_c > 1$ fabricated so far, also offer the ideal quantum hardware.

Amongst other protocols in the Lambda scheme, where population transfer is obtained by SEP or by inducing Raman oscillations, STIRAP is in principle superior beacuse of it allows $\sim 100\%$ efficiency and it is remarkably robust against the many and uncontrolled parametric fluctuations. What makes coherent population transfer unique is the possibility to operate in Vee configuration, which is resilient to the presence of stray couplings between the cavity and the artificial atom, inevitable in a solid state architecture. While in Lambda configuration

stray couplings provide new not USC-specific paths to population transfer, this does not happen for V-STIRAP and population transfer is a "smoking gun" for USC. Moreover external fields in V-STIRAP couple more strongly with the system, allowing for easier and faster control.

Concerning experiments, we remark that the whole population history for the Fock state $|n = 2\rangle$ of the cavity (practically equal to the population of the target state in Fig. 6.4) can be measured. Thus more evidence can be provided of the presence of USC than the final detection of two photons. At the same time detection of USC is sufficiently assessed even if the population history is mesasured only for a part of the protocol. Also adiabaticity sould not be fully enforced, since some transient population of the intermediate state can be tolerated. Therefore the requirement for the experiment are softened, expecially as far as decoherence is concerned.

Chapter 7

Non-equilibrium thermodynamics of continuously measured quantum systems

We propose a fully operational framework to study the non-equilibrium thermodynamics of a quantum system S that is coupled to a detector D whose state is continuously monitored, allowing to single out individual quantum trajectories of S. In particular, we focus on detailed fluctuation theorems and characterize the entropy production of the system. We establish fundamental differences with respect to the thermodynamic of unmonitored, unitarily evolved systems. We consider the paradigmatic example of circuit-QED, where superconducting qubits can be coupled to a continuously monitored resonator and show numerical simulations using state of the art experimental parameters.[1]

7.1   Introduction

The origin of dynamic irreversibility and the emergence of the arrow of time from the microscopic foundations of quantum mechanics have attracted significant interest in the past few years [61, 156, 71]. In particular, recent efforts in the field of non-equilibrium quantum thermodynamics resulted in the characterization of irreversibility in terms of fluctuation theorems [65] and entropy production [70].

   The standard formulation of non-equilibrium thermodynamic quantities uses

---

[1]The content of this chapter has been adjusted, with minor modifications, from P.G. Di Stefano, J.J. Alonso, E. Lutz, G. Falci and M. Paternostro, Non-equilibrium thermodynamics of continuously measured quantum systems, in preparation.

explicitly time-gated multi-measurement strategies [65]. Notwithstanding the success encountered by such formulations in describing the thermodynamic implications of non-equilibrium processes all the way down to the quantum domain [71], such requirements are very difficult to be met in practice. Indeed, the common experimental configurations typically involve the continuous interaction between a system and a measurement apparatus. Such interaction can result in either strong projective measurements of the state of the quantum system at hand, or only the acquisition of partial information on it. Recently, a theoretical framework for the analysis of stochastic thermodynamics of weakly monitored quantum systems was put forward [157, 166].

Here we make further steps along the lines of defining a fully operational framework for stochastic thermodynamics of continuously monitored systems by considering the case of a (dynamical) detector coupled to a system of interest and being continuously monitored. This situation adheres perfectly with the configurations typically engineered and encountered in a wide range of experiments. In particular, circuit-QED systems embody a very suitable platform, where the system is typically provided by a set of superconducting information carriers, while the field of a stripline resonator plays the role of the continuously monitored dynamical detector [30]. This offers a virtually ideal scenario for the study of stochastic thermodynamics of continuously monitored systems, and the investigation of the deviates from the time-gated approach that has dominated the field to date. In particular, our work sets the theoretical context for the experimental analysis of irreversibility in the non-equilibrium dynamics of a driven superconducting device as quantified by the irreversible entropy production, and the test of the continuous-monitoring version of fundamental fluctuation theorems.

7.2 Non-equilibrium thermodynamics of closed quantum systems

The typical setting for a non-equilibrium thermodynamics experiment in closed quantum systems is the following: a system S of Hamiltonian $H_S(\lambda_t) = \sum \epsilon_k(\lambda_t) |n^{\lambda_t}\rangle \langle n^{\lambda_t}|$ is initially (time $t = 0$) in equilibrium with its environment at inverse temperature β, i.e. $\rho_S(0) = \rho_0$, where we defined the Gibbs state $\rho_t = \mathrm{e}^{-\beta H_S(\lambda_t)}/\mathcal{Z}_t$ with $\mathcal{Z}_t = \mathrm{Tr}[\mathrm{e}^{-\beta H_S(t)}]$ the partition function. It is then brought out of equilibrium by the application of an external force protocol λ_t parametrized in the time interval $[0, \tau]$. In the closed quantum systems scenario, it is assumed that in $[0, \tau]$ the system is effectively detached from its environment and that S

evolves unitarily through the time-evolution operator $U_{t_1,t_2} := \mathcal{T} e^{-i \int_{t_1}^{t_2} dt' \ H(\lambda_{t'})}$, where $\mathcal{T}$ is the time-ordering operator. The non-equilibrium work performed on the system is usually defined [158] as a stochastic variable W whose single realizations $\epsilon_m(\tau) - \epsilon_n(0)$ are weighted by the probability of observing a $|n^{\lambda_0}\rangle \to |m^{\lambda_\tau}\rangle$ transition due to the application of the force protocol. Identifying $p(m^\tau, n^0) = \mathrm{Tr}[\Pi_m^\tau \mathcal{U}_{\tau,0} \Pi_n^0 \rho_0 \Pi_n^0 \mathcal{U}_{\tau,0}^\dagger]$, where $\Pi_k^t = |k^{\lambda_t}\rangle \langle k^{\lambda_t}|$, as the probability for such a transition to occur, one may define the work distribution as $p_F(W) = \sum_{m^\tau, n^0} p(m^\tau, n^0)\delta(W - \epsilon_m(\tau) + \epsilon_n(0))$. In order to address irreversibility, the corresponding *backward* work distribution is usually considered, where the force protocol is reversed in time. One then looks at the probability of the backward transition $\Theta |m^{\lambda_\tau}\rangle \to \Theta |n^{\lambda_0}\rangle$, Θ being the time-reversal operator, with initial statistics given by the Gibbs state $\tilde{\rho}_\tau = \Theta \rho_\tau \Theta^\dagger$ at time $t = \tau$ when the backwards protocol $\tilde{\lambda}_t = \lambda_{\tau-t}$ is applied. In considering the backwards protocol, we will assume that the Hamiltonian of the systems obeys a time-reversal symmetry of the form $\Theta H_S(\lambda_t)\Theta^\dagger = \epsilon_\lambda H_S(\lambda_{\tau-t})$ where $\epsilon_\lambda = \pm 1$. We call $p_B(W)$ the corresponding backward work distribution and state the Crooks fluctuation theorem [67]

$$p_F(W)/p_B(-W) = \exp[\beta(W - \Delta F)], \tag{7.1}$$

where we used the free energy difference $\Delta F = -1/\beta \log(\mathcal{Z}_\tau/\mathcal{Z}_0)$. By integrating over W one gets the celebrated Jarzynski identity $\langle e^{-\beta(W-\Delta F)}\rangle = 1$, which entails the second law through the Jensen inequality $\langle \sigma \rangle \geq 0$, where the irreversible entropy production $\sigma = \beta(W - \Delta F)$ has been defined.

7.3 Quantum stochastic thermodynamics: a Circuit-QED implementation

The closed quantum systems paradigm is in contrast with the approach of classical stochastic thermodynamics. In the latter, work realizations are described in terms of trajectories of a classical system in the phase space. In this section, we propose an implementation of a non-equilibrium thermodynamics experiment using the framework of quantum *stochastic* thermodynamics [166]. We thus exploit the formalism of quantum trajectories considering a system that is continuously monitored during its evolution through the coupling with a detector D. By doing so, we are able to single out individual quantum trajectories and characterize irreversibility in a way that is compatible with the classical picture. Despite methodological similarities, though, we point out that important differences arise
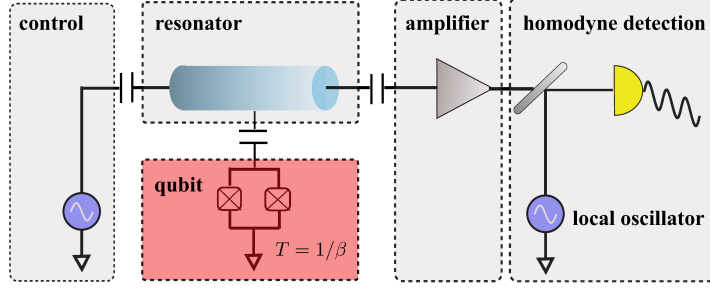
Figure 7.1: Setup for a circuit QED implementation. A superconducting qubit is coupled to a resonator, through which it is measured and controlled. Measurement is performed by means of continuous homodyne observation of the amplified cavity field. A strong local oscillator provides a second amplification stage producing an output current $I(t)$ encoding information about qubit and resonator.

due to the back-action of quantum measurement on the system state.

We specifically address the platform typical of circuit-QED implementations, as as the one depicted in Fig. 7.1. We thus consider a superconducting qubit, e.g. a transmon [74], coupled to a microwave resonator in the strong dispersive coupling regime. The latter is used both to drive (thus acting as a forcing mechanism) and to measure the qubit [30]. Recently, continuous monitoring in circuit-QED has been successfully employed to observe single quantum trajectories of a transmon qubit [159, 34, 160, 161] and quantum jumps [162]. We have reviewed the weak, diffusive regime of quantum trajectory theory for the Circuit-QED system in Sec. 2.2.1.

We shall regard the qubit as our system of interest S and the resonator as the detector D. The $S + D$ system is driven by a "forcing" field oscillating at frequency $\omega(t)/2\pi$ and almost resonant with the qubit frequency $\omega_0/2\pi$, and by a "measurement" field having angular frequency ω_d that is, for simplicity, assumed exactly resonant with the resonator frequency $\omega_c/2\pi$. Qubit and resonator will be dispersively coupled, i.e. $g \ll \Delta$, where g is the strength of the coupling and $\Delta = \omega_0 - \omega_c$ is the cavity-qubit detuning. We will also assume $g \ll \omega_{0,c}$, i.e. we will be outside the so-called ultra-strong coupling[4], as it is the case in most of the implementations reported so far in literature. The Hamiltonian of the total system can be split as

$$H = H_S + H_D + H_{\text{int}} \tag{7.2}$$

where we defined the detector Hamiltonian $H_D = \omega_0 \, a^\dagger a + \epsilon_d \, (a e^{i\omega_d t} + a^\dagger e^{-i\omega_d t})$, a being the annihilation operator for the resonator field, and the interaction Hamiltonian is $H_{\text{int}} = \chi \sigma_z a^\dagger a$, where σ_i are the usual Pauli operators. Here $\chi = g^2/\Delta$

is an effective coupling in the dispersive regime determining a Stark shift of the cavity frequency conditional on the qubit state, which is the physical mechanism for the qubit detection. The dispersive regime also implies weak coupling between qubit and field, allowing us to separately define energies. The system Hamiltonian H_S can be split into

$$H_S = H_0 + H_{\lambda_t} \tag{7.3}$$

where $H_0 = \omega_0 \sigma_z/2$ is the bare Hamiltonian of the qubit and $H_{\lambda_t} = \delta\omega_0(t)\sigma_z/2 + \Omega(t)\cos(\varphi(t))\sigma_x$ is the time-dependent contribution that implements the force protocol. In circuit-QED, the available control that can be exploited in order to manipulate the system breaks down into independent tunability of both the qubit frequency $\delta\omega_0(t)$, achieved through the application of a time-dependent magnetic field in the SQUID loop of the device, and the parameters of the external microwave field, i.e. the amplitude $\Omega(t)$ and phase $\varphi(t)$.

The conditional stark shift H_{int} allows for the the state of the qubit to be mapped onto a quadrature of the field. In our model this has been set to be the in-phase quadrature X_0, where we defined the quadrature of phase ϕ as $X_\phi = (ae^{i\phi} + a^\dagger e^{-i\phi})/\sqrt{2}$. Continuous monitoring can thus be done through homodyne measurements of the field leaking out of the resonator at rate κ [89]. The homodyne photocurrent resulting from the mixing of the cavity field with a strong local oscillator tuned on the phase of the quadrature X_0 is therefore continuously observed inducing quantum back-action on the $S + D$ system. The evolution of the system over a single quantum trajectory will be thus conditional on the measured photocurrent. In order to describe the dynamics of the system, we slice the time interval $[0, \tau]$ into small but finite time intervals $\delta t = t_{j+1} - t_j$ with $0 < t_1 < t_2 < ... < t_N < \tau$. Here, δt is chosen to be much smaller than the shortest time-scale of the problem, so that we can approximate $\mathcal{U}_{t_i, t_{i+1}} \simeq \mathbb{1} - iH\delta t$. The effect of a measurement can be modelled through the positive operator valued measurement (POVM) L_x, such that $\int dx L_x^\dagger L_x = \mathbb{1}$, where x refers to the average value of the homodyne photocurrent over δt. In the small time interval δt, the overall dynamics of the system can be effectively factorized into two independent contributions given by unitary evolution and measurement. Defining the operators $\mathcal{O}_{t_i} = L_{I(t_{i+1})}\mathcal{U}_{t_i, t_{i+1}}$, the evolution of the system, conditional to the observation of the average photocurrent stream $I = \{I(0), I(t_1), ..., I(t_k)\}$, is

therefore given by

$$\rho_{D+S}(t_k) = \frac{(\overleftarrow{\prod}_{i<k}\mathcal{O}_{t_i})\rho_{D+S}(0)(\overrightarrow{\prod}_{i<k}\mathcal{O}_{t_i}^\dagger)}{\mathrm{Tr}[(\overleftarrow{\prod}_{i<k}\mathcal{O}_{t_i})\rho_{D+S}(0)(\overrightarrow{\prod}_{i<k}\mathcal{O}_{t_i}^\dagger)]}, \tag{7.4}$$

where the arrows imply time ordering. In the homodyne measurement scheme for circuit-QED, measurement operators are given by $L_x = [1-\frac{1}{2}\kappa a^\dagger a \delta t + x\sqrt{\kappa}\delta t]\sqrt{p_o(x)}$, where $p_o(x) = \exp(-\delta t x^2)/\sqrt{\delta t/2\pi}$ is the ostensible [87] probability density of obtaining the result x for the homodyne photocurrent. We should point out that additional decoherence terms may add up in the dynamics of the system, caused by relaxation and dephasing of the qubit. We did not include those terms in our analysis since, as it will be argued later, decoherence rates are small enough in present technology to have a negligible effect in the time scale relevant to the experiment.

The statistics of the qubit alone is, in general, given by partial tracing over the detector degrees of freedom. Nonetheless, in the limit of a sufficiently weak measurement, i.e. when the average number of photon is $\bar{n} = (\epsilon_d/\kappa)^2 \ll 1$, $\chi \ll \kappa$ and the driving is weak, i.e. $\Omega \ll \kappa$, the qubit and the detector develop negligible entanglement [83] and the dynamics of the S can be factorized from the dynamics of D. The qubit density matrix at time t_k will be therefore given by (see Sections 2.2.1 and 7.A)

$$\rho_S(t_k) = \frac{(\overleftarrow{\prod}_{i<k}\mathcal{Q}_{t_i})\rho_S(0)(\overrightarrow{\prod}_{i<k}\mathcal{Q}_{t_i}^\dagger)}{\mathrm{Tr}[(\overleftarrow{\prod}_{i<k}\mathcal{Q}_{t_i})\rho_S(0)(\overrightarrow{\prod}_{i<k}\mathcal{Q}_{t_i}^\dagger)]} \tag{7.5}$$

where $\mathcal{Q}_{t_i} = M_{I(t_{i+1})}e^{-i\int_{t_i}^{t_{i+1}} dt H_S(t)}$ and the POVM operators for the qubit alone are given by

$$M_x = \sqrt{P_0(x)}\,|0\rangle\,\langle 0| + \sqrt{P_1(x)}\,|1\rangle\,\langle 1|. \tag{7.6}$$

Here we defined the probability distributions $P_j(x) = e^{-i\delta t/2(x+(-1)^j\sqrt{\Gamma_d})^2}$ [163] (see, also, Section 7.A), with the measurement rate given by $\Gamma_d = 16\chi^2\bar{n}/\kappa$.

During its evolution, the system will experience transformations in its internal energy $U(t) = \mathrm{Tr}[\rho_S H_S]$. The infinitesimal variation $dU(t_i) = \delta W_i + \delta Q_i$ of the latter can be split into a unitary and a back-action term, i.e.

$$\delta W_i = \mathrm{Tr}[\rho_S(t_i)\,dH(t_i)], \ \ \delta Q_i = \mathrm{Tr}[H(t_i)\,d\rho_S(t_i)], \tag{7.7}$$

where the discretized differential is $dX(t_i) = X(t_{i+1}) - X(t_i)$. Correspondingly, we will define work and heat as $W(t) = \sum_{t_i<t}\delta W_i$ and $Q(t) = \sum_{t_i<t}\delta Q_i$. Notice

that the above definition of work is fundamentally different from the usual one for closed systems. In the latter case, as mentioned above, work realizations are determined as differences between eigenvalues of the final and initial Hamiltonian. For a system is continuously monitored, on the other hand, work can be defined at the single trajectory level as a time-dependent stochastic process. This is similar, in spirit, to the approach of classical stochastic thermodynamics [64] with the fundamental difference that, while in classical physics a trajectory in phase space can be monitored without disturbing its dynamics, measurement back action plays a fundamental role in quantum systems, generating the heat term Q. The latter has been given a straightforward interpretation in Refs. [157, 166] as the amount of work an external daemon would need to contribute in order to counter quantum back action.

We are now concerned with the characterization of irreversibility for this system, which can be done by means of detailed fluctuation theorems. The probability of observing a particular single trajectory in the Hilbert space, though, cannot be defined, as it was the case for closed systems, only through its end points. The stochastic evolution of the system's state have, in fact, to be taken into account. From Eq. (7.5), we see that a single trajectory can be fully characterized if we also take into account the measured current $I(t)$. The probability of observing a trajectory starting from $|n^0\rangle$ and ending in $|m^\tau\rangle$ while measuring $I(t)$ is then given by

$$p_F(m^\tau, I(t), n^0) = \text{Tr}[\Pi_{m^\tau}(\overleftarrow{\prod_i} \mathcal{Q}_{t_i})\Pi_{n^0}\rho_0\Pi_{n^0}(\overrightarrow{\prod_i} \mathcal{Q}_{t_i}^\dagger)] \tag{7.8}$$

In the spirit of the detailed fluctuation theorem of Eq. (7.1), we will again consider a backwards trajectory starting in $\Theta|m^\tau\rangle$ and ending in $\Theta|n^0\rangle$ where the time-reversal force protocol is applied together with the time-reversal POVM operators $\tilde{M}_x$. Employing the operators $\tilde{\mathcal{Q}}_{t_i} = \mathcal{U}_{t_i, t_{i+1}}[\tilde{\lambda}(t)]\tilde{M}_{\tilde{I}(t_{i+1})}$, where $\tilde{M}_{\tilde{I}(t)} = \theta M_{I(\tau-t)}^\dagger\theta^\dagger$ are the time-reversed measurement operators, we define the probability of the backward trajectory as

$$p_B(n^0, \tilde{I}(t), m^\tau) = \text{Tr}[\tilde{\Pi}_{n^0}(\overleftarrow{\prod_i} \tilde{\mathcal{Q}}_{t_i})\tilde{\Pi}_{m^\tau}\tilde{\rho}_\tau\tilde{\Pi}_{m^\tau}(\overrightarrow{\prod_i} \tilde{\mathcal{O}}_{t_i}^\dagger)], \tag{7.9}$$

where $\tilde{\Pi}_k = \Theta\Pi_k\Theta^\dagger$ and $\tilde{\rho}_\tau = \Theta\rho_\tau\Theta^\dagger$. It has been shown in Ref. [68] that one

can state a generalized detailed fluctuation theorem as

$$\frac{p_F(m^\tau, I(t), n^0)}{p_B(n^0, \tilde{I}(t), m^\tau)} = e^{\beta(\Delta U_{nm} - \Delta F)}, \tag{7.10}$$

where the internal energy difference is defined as $\Delta U_{nm} = \epsilon_m(\tau) - \epsilon_n(0)$. We should point out that, in general, with such a notion of time reversal, p_B is not a proper probability distribution, i.e. $\int p_B(n^0, \tilde{I}(t), m^\tau)\mathcal{D}I \neq 1$, where $\mathcal{D}I$ is a measure for the path integral. The normalization condition holds if and only if $\int \mathrm{d}x\, M_x M_x^\dagger = \mathbb{1}$, which is indeed the case for the reduced dynamics for the qubit, where the measurements operators are hermitian. The probability distribution of the internal energy can then be written as

$$p(\Delta U) = \sum_{m,n} \int \mathcal{D}I\, p_F(m^\tau, I(t), n^0)\delta(\Delta U - \Delta U_{nm}), \tag{7.11}$$

which immediately gives $\langle e^{-\sigma} \rangle = 1$. Here, the entropy production $\sigma = \beta(W + Q - \Delta F)$ allows again to derive the second law of thermodynamics $\langle \sigma \rangle \geq 0$ by virtue of Jensen inequality. Notice that the heat term [166] is a unique feature of quantum back-action, and has thus no equivalent neither in the closed quantum system case, nor in the classical stochastic thermodynamics case.

In order to numerically simulate our results, we made use of parameters borrowed from state of the art technology [159]. In particular, we considered an architecture involving transmon with $\omega_0/2\pi = 4$ GHz, a leaking rate of the resonator at $\kappa/2\pi = 10$ MHz and coupling constant $\chi/2\pi = -0.5$ MHz. We also set the amplitude of the measurement field so to have, as in Ref. [159], an average number $\bar{n} = 2(\epsilon_d/\kappa)^2 = 0.4$ of photons in the cavity. These parameter yield a measurement rate $\Gamma_d/2\pi = 160$KHz, which gives a measurement time [89] $t_m = 1/(2\Gamma_d) \simeq 500$ns, which is usually much smaller than energy relaxation and pure dephasing times for a state-of-the-art transmon ($T_1 \sim T_2^* \gtrsim 10\mu$s). This enabled us to neglect energy relaxation and dephasing in our model.

We considered a force protocol in which the frequency of the qubit and the amplitude of the field are both quenched, i.e.

$$\delta\omega_0(t) = \Delta\omega\,\theta(t - \frac{\tau}{2}), \quad \Omega(t) = \Omega_0\,\theta(t - \frac{\tau}{2}), \tag{7.12}$$

where we used values $\Delta\omega/2\pi = 400$MHz and $\Omega_0/2\pi = 1$MHz, while we kept the external drive frequency constant, i.e. $\dot{\varphi}(t) =: \omega = \omega_0 + \Delta\omega$.

In Fig. 7.2 we plot the results of our simulations. Fig. 7.2(a) shows how the
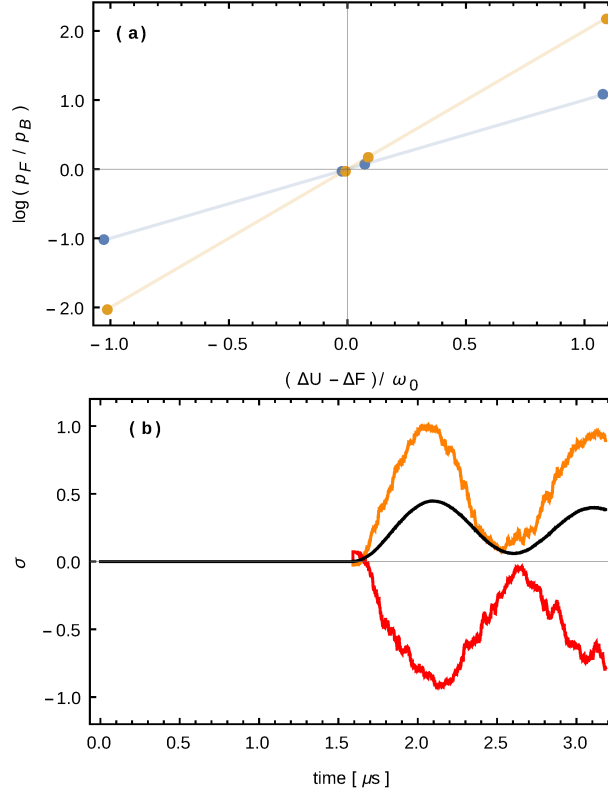
Figure 7.2: Numerical results for the protocol of Eq.(7.12). (a) Logarithmic representation of the detailed fluctuation theorem of Eq. (7.10). Here we used $\beta = 1/\omega_0$ (blue curve) and $\beta = \omega_0$. (b) Entropy production trajectories (coloured curves) for $\beta = 1/\omega_0$ showing how negative entropy production trajectories can observed. The mean entropy production (black curve), though, is always non negative.

detailed fluctuation theorem of Eq. (7.10) can be tested. In particular, we plot the Equation $\log p_F/p_B = -\beta(\epsilon_m(\tau) - \epsilon_n(0) - \Delta F)$, which is tested by showing how the slope of the interpolation lines in Fig. 7.2(a) equals β. In particular, we employed values $\beta = 1/\omega_0$ (blue curve) and $\beta = 2/\omega_0$ (orange curve). In Fig. 7.2 (b) we show trajectories for the entropy production (colored lines) together with the mean entropy production (black line). We notice how, while the mean entropy production is non-negative as required by the second law of thermodynamics, stochastic thermodynamics attained through continuous monitoring of a small quantum system, such as a transmon, allows to observe *negative* entropy production trajectories, in striking contrast with what one experiences in the macroscopic world.

7.4   Conclusions

We proposed a fully operational framework for the exploration of stochastic quantum thermodynamics. We have shown how detailed fluctuation theorems verification and measurement of witnesses of irreversibility such as the entropy production are easily accessed in circuit-QED architectures. Finally, we have shown how high quality experiments can be set up in existing labs employing state of the art technology.

7.A   Derivation of the dynamical equations

In the present appendix, in order to simplify the notation, we shall refer to the system's state as ρ and to its Hamiltonian as $H := 1/2\delta\omega\sigma_z + \Omega(t)\sigma_x$. In section 2.2.1 we studied the theory of continuously monitored systems in circuit-QED and, in particular, reported in Eq. (2.53) the dynamics of the qubit alone when negligible entanglement is developed with the resonator. Our purpose here is to derive Eq. (7.5).

For numerical simulations and in order to take into account the finite bandwidth of the electronics in the circuit, a discretized version of Eq.(2.53) must be employed, reading

$$
\begin{aligned}
\rho_{00}(t + \delta t) = \rho_{00}(t) + (&-2H_{01}Im\{\rho_{01}\} \\
&+ 2\sqrt{\Gamma_d}\rho_{00}\rho_{11}(I - \sqrt{\Gamma_d}\langle\sigma_z\rangle))\delta t \\
\rho_{01}(t + \delta t) = \rho_{01}(t) + (&iH_{00}\rho_{01} + iH_{01}(\rho_0 0 - \rho_{11}) \\
&- \sqrt{\Gamma_d}(\rho_{00} - \rho_{11})(I - \sqrt{\Gamma_d}\langle\sigma_z\rangle) - \frac{\Gamma_d}{2}\rho_{01})\delta t
\end{aligned}
\tag{7.13}
$$

where δt is a small, but finite, time interval such that $\delta t \ll 1/H_{01}, \Gamma_d$ and the current $I := \frac{1}{\delta t}\int_t^{t+\delta t} dt' \; I_h(t')$ has been introduced and I_h is the full spectrum homodyne current introduced in Sec. 2.2.1. Notice that I can be written as $I := \langle\sigma_z\rangle + \bar{\xi}$, $\bar{\xi}$ being now gaussian distributed with standard deviation $\delta t^{-1/2}$. The probability distribution for I will then be

$$
P(I) = \sqrt{\frac{\delta t}{2\pi}}\mathrm{e}^{-\frac{\delta t}{2}(I - \sqrt{\Gamma_d}\langle\sigma_z\rangle)^2}
\tag{7.14}
$$

We shall now show how the dynamics can be approximated, up to the order one in δt, with Eq. (7.5) in the main text. When a current sample I is measured, the

conditional evolution over a single time step is given by:

$$\rho(t+\delta t) = \frac{U_{t,t+\delta t} M_I \rho(t) M_I^\dagger U_{t,t+\delta t}^\dagger}{U_{t,t+\delta t} M_I \rho(t) M_I^\dagger U_{t,t+\delta t}^\dagger} \tag{7.15}$$

where M_I have been given in Eq. (7.6) in the main text. At first we are going to assume $H = 0$, i.e. $U_{t,t+\delta t} = \mathbb{1}$. Adding the unitary term will be then straightforward. In the measurement basis, Eq. (7.15) can be written as

$$\rho_{00}(t+\delta t) = \frac{\rho_{00}(t)P_0(I)}{\rho_{00}(t)P_0(I)+\rho_{11}(t)P_1(I)}$$
$$\rho_{01}(t+\delta t) = \frac{\rho_{01}(t)\sqrt{P_0(I)P_1(I)}}{\rho_{00}(t)P_0(I)+\rho_{11}(t)P_1(I)} \tag{7.16}$$

notice that, for $\delta t^{-1} \gg \Gamma_d$ the mixture distribution on the denominator is indistinguishable from Eq. (7.14), i.e. $P(I) \simeq \rho_{00}P_0(I) + \rho_{11}P_1(I)$. Substituting this expression into Eq.(7.16) and using $\bar{\xi} = I - \sqrt{\Gamma_d}\langle\sigma_z\rangle$ we get

$$\rho_{00}(t+\delta t) = \rho_{00}(t)e^{-\delta t\frac{(\bar{\xi}-q_1)^2}{2}}e^{\delta t\frac{\bar{\xi}^2}{2}}$$
$$\rho_{01}(t+\delta t) = \rho_{01}(t)\sqrt{e^{-\delta t\frac{(\bar{\xi}-q_0)^2}{2}}e^{-\delta t\frac{(\bar{\xi}-q_1)^2}{2}}e^{\delta t\frac{\bar{\xi}^2}{2}}} \tag{7.17}$$

where we defined $q_i := -2\sqrt{\Gamma_d}\rho_{ii}$. Expanding up to second order in q_1 and q_2 and approximating $\bar{\xi}^2 = \delta t$ [87] gives Eq. (7.13) with $H = 0$. Introducing now the unitary term through Eq.(7.15) and expanding up to the leading order in δt can be easily shown to reproduce the full structure of Eq. (7.13), therefore justifying our model.

Chapter 8

Conclusions

In this work we have discussed how advanced control techniques can be applied to superconducting qubits. In particular, we discussed techniques for population transfer in Lambda systems like conventional STIRAP, cSTIRAP and 2+1-STIRAP. We have shown that almost unit transfer efficiency can be achieved with present technology devices. Our work paves the way towards several applications in quantum technologies, such as holonomic quantum computation, secure quantum communication between distant nodes and highly non-classical microwave radiation manipulation.

We have shown how Ultra Strong Coupling effects can be dynamically amplified and detected using STIRAP. This can be achieved in state of the art flux qutrits in a robust and efficient way uniquely showing features of non-classical light-matter coupling, such as non conservation of excitations number.

We have, finally, proposed an experimental implementation to study how irreversibility and the arrow of time arise at the quantum level. We have shown how stochastic thermodynamics can be used to show the validity of fluctuation theorems and to witness irreversibility by means of the entropy production.

Appendix A

Quantum circuit theory

Our goal is to find a systematic procedure for writing the quantum Hamiltonian of a general non-dissipative electric circuit. In order to do this, it is convenient to write the circuit dynamical equations in terms of charges and fluxes rather than the usual currents and voltages. Charges and fluxes, as we shall see, will serve as conjugate coordinates for the Hamiltonian formalism. Our discussion will be mainly based on the work of Devoret [164]. More recently, the quantum theory of electrical circuits has been reviewed in Ref. [72].

A.1 Circuit theory in terms of fluxes and charges

We formally describe a lumped elements circuit as a connected graph whose branches are two-terminal electrical components characterized by two variables, namely the branch current and the branch voltage. For each branch b, we define branch fluxes Φ_b and branch charges Q_b as:

$$\Phi_b(t) = \int_{-\infty}^{t} dt' v_b(t') \tag{A.1}$$

$$Q_b(t) = \int_{-\infty}^{t} dt' i_b(t') \tag{A.2}$$

where v_b and i_b are, respectively, branch voltage and current of b. Each branch has a constitutive relation, named *branch relation*, connecting currents and voltages. This relation is not necessarily algebraic: it can in fact be differential. Depending on the form of the branch relation, circuital elements are classified as resistive, capacitive or inductive. A resistor is a component who exhibits an algebraic relation (or *characteristic*) in the i_b/v_b plane, capacitors and inductors

have characteristics, respectively, in the Q_b/v_b and in the Φ_b/i_b, i.e.

$$v_r = \phi(i_r); \quad v_c = f(Q_b); \quad i_l = g(\Phi_l). \tag{A.3}$$

The instantaneous power flowing in such elements is given by the product of the current times the voltage: $p_b(t) = v_b i_b = v_b \dot{Q}_b = \dot{\Phi}_b i_b$. So we can write the energy of a capacitor as:

$$h_c(Q_b) = \int_0^{Q_b} dQ f(Q) \tag{A.4}$$

Analogously for an inductor:

$$h_l(\Phi_b) = \int_0^{\Phi_b} d\Phi f(\Phi) \tag{A.5}$$
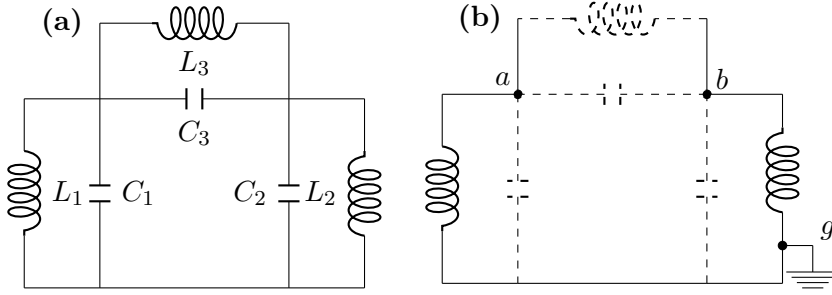
A.1.1 Kirchhoff's laws and cut-set analysis

Figure A.1: (a) Example of a non-dissipative reactive circuit. (b) The same circuit where we emphasized the tree (solid branches) and the links (dashed branches).

Branch fluxes and charges can't be taken as conjugate variables, since they are not independent. Kirchhoff's laws of currents and voltages must, in fact, be satisfied. That is, the algebraic sum of currents arriving at a node n and the algebraic sum of voltages in a loop l must both be zero. In terms of fluxes and charges, for any loop l and for any node n, the Kirchhoff's laws can be restated as follows:

$$\sum_{all\ b\ around\ l} \Phi_b = \tilde{\Phi}_l \tag{A.6}$$

$$\sum_{all\ b\ arriving\ at\ n} Q_b = \tilde{Q}_n \tag{A.7}$$

The set of all Kirchhoff's laws for a circuit is not, in general, a set of linearly independent equation. The problem to find a complete set of independent equations

have is solved using different methods like node analysis, loop analysis or mesh analysis. In the following we will make use of *cut-set analysis*.

First, we have to introduce node variables. Unlike branch variables, node variables depend on a particular description of the topology of the circuit. We will use the following. One node, say g, is chosen as a reference *ground* node. The others are referred to as *active nodes*. The graph $\mathcal{G}$ representing the circuit is divided into a *tree* $\mathcal{T}$ and a set $\mathcal{L}$ of *links*: $\mathcal{G} = \mathcal{T} \cup \mathcal{L}$. $\mathcal{T}$ is formed choosing a set of branches such that $\mathcal{T}$ contains every node and for each node n a unique path in $\mathcal{T}$ exists connecting n to g. The remaining branches are in $\mathcal{L} := \mathcal{G}$ $\mathcal{T}$. In the following we will refer to the example of fig. A.1.1, that we borrowed from Ref. [164]. It can be shown that for each branch $b \in \mathcal{L}$ only one loop $l(b)$ exists that contains b and no other branches in $\mathcal{L}$. These loops are usually called *fundamental loops* [165]

We can now define the *node flux* Φ_n of the node n as the time integral of the sum of the voltages of the branches connecting g to n, namely:

$$\Phi_n = \sum_b S_{nb} \Phi_b \tag{A.8}$$

where S_{nb} is 1, -1 or 0 depending on whether b is in the path connecting g to n with the proper orientation (within the convention chosen for the signs of the branch voltages), with the opposite orientation or it is not present. Conversely, we can write the flux of the branch b connecting nodes n and n' in terms of the node fluxes Φ_n and $\Phi_{n'}$. Attention must be paid in including the *static fluxes* $\tilde{\Phi}_{l(b)}$ corresponding to the fundamental loops of the links.

$$\Phi_{b \in \mathcal{T}} = \Phi_n - \Phi_{n'} \tag{A.9}$$

$$\Phi_{b \in \mathcal{L}} = \Phi_n - \Phi_{n'} + \tilde{\Phi}_{l(b)} \tag{A.10}$$

Each $b \in \mathcal{T}$ is associated to a *fundamental cut-set*. We define a fundamental cut-set as follows. Let us remove $b_t \in \mathcal{T}$ from $\mathcal{T}$. The tree will now be composed of two unconnected parts, say $\mathcal{A}$ and $\mathcal{B}$, identified by two set of nodes. The links connecting the nodes of $\mathcal{A}$ to the nodes of $\mathcal{B}$, together with b_t, form the fundamental cut-set. It can be shown [165] that the set of the Kirchhoff's current laws at the fundamental cut-sets, expressed in the branch fluxes, is a set of linearly independent linear differential equations.

A.2   Lagrangian formalism for electric circuits

Let us refer to the circuit of fig A.1.1(b) where we have emphasized the tree (solid line) and the links (dashed lines). Equating the current of the capacitors to the current of the inductors, each expressed in terms of the branch variables yields:

$$C_1\ddot{\Phi}_{C_1} + C_3\ddot{\Phi}_{C_3} = \frac{\Phi_{L_1}}{L_1} + \frac{\Phi_{L_3}}{L_3} \tag{A.11}$$

$$C_2\ddot{\Phi}_{C_2} - C_3\ddot{\Phi}_{C_3} = \frac{\Phi_{L_2}}{L_2} - \frac{\Phi_{L_3}}{L_3} \tag{A.12}$$

If we now express the branch variables Φ_{C_i}, Φ_{L_i} in terms of node variables Φ_a and Φ_b we find:

$$C_1\ddot{\Phi}_a + C_3(\ddot{\Phi}_a - \ddot{\Phi}_b) = \frac{\Phi_a}{L_1} + \frac{\Phi_a - \Phi_b + \tilde{\Phi}}{L_3} \tag{A.13}$$

$$C_2\ddot{\Phi}_b - C_3(\ddot{\Phi}_a - \ddot{\Phi}_b) = \frac{\Phi_b}{L_2} - \frac{\Phi_a - \Phi_b + \tilde{\Phi}}{L_3} \tag{A.14}$$

Equations A.13 and A.14 are the Eulero-Lagrange equations for a Lagrangian obtained subtracting the magnetic energy of the inductors from the electric energy of the capacitors, namely:

$$\begin{aligned}
\mathcal{L} =&K - U = \\
=& \frac{C_1\dot{\Phi}_a^2}{2} + \frac{C_2\dot{\Phi}_b^2}{2} + \frac{C_3(\dot{\Phi}_a - \dot{\Phi}_b)^2}{2} - \left[\frac{\Phi_a^2}{2L_1} + \frac{\Phi_b^2}{2L_2} + \frac{(\Phi_a - \Phi_b)^2}{2L_3}\right]
\end{aligned} \tag{A.15}$$

Node fluxes, thus, play the role of *generalized coordinates* in classical Lagrangian mechanics.

A.3   Hamiltonian formalism for electric circuits

In order to derive the Hamiltonian of the circuit of Fig. A.1.1, we define the conjugate momenta as:

$$q_n = \frac{\partial\mathcal{L}}{\partial\dot{\Phi}_n} \tag{A.16}$$

If we look at eq. A.15, we immediately identify q_a and q_b as the algebraic sum of the charges stored at nodes a and b respectively. Hence, node charges are the momenta conjugated to the node fluxes. The Hamiltonian is obtained by the

usual Legendre transformation:

$$
\begin{aligned}
H =& \sum_n q_n \dot{\Phi}_n - \mathcal{L} = \\
=& \frac{1}{C_1 C_2 + C_1 C_3 + C_2 C_3} \left[\frac{(C_2 + C_3) q_a^2}{2} + \frac{(C_1 + C_3) q_b^2}{2} + \frac{C_3 (q_a - q_b)^2}{2} \right] \\
& + \frac{\Phi_a^2}{2L_1} + \frac{\Phi_b^2}{2L_2} + \frac{(\Phi_a - \Phi_b)^2}{2L_3}
\end{aligned}
\tag{A.17}
$$

A.4 Quantization of the model

Quantization of the model is obtained by promoting the canonically conjugated variables appearing in the Hamiltonian of Eq.(A.17) to operators in a Hilbert space:

$$
\Phi_i \rightarrow \hat{\Phi}_i
$$

$$
q_i \rightarrow \hat{q}_i
$$

satisfying the canonical commutation relation, i.e.:

$$
[\hat{\Phi}_i, \hat{q}_j] = i \delta_{ij} \hbar
\tag{A.18}
$$

where δ_{ij} is the Kronecker delta.

Writing the expression of the classical Hamiltonian in terms of these operators yields the quantum Hamiltonian. For the circuit of Fig. A.1.1 we thus find:

$$
\begin{aligned}
\hat{H} =& \frac{1}{C_1 C_2 + C_1 C_3 + C_2 C_3} \left[\frac{(C_2 + C_3) \hat{q}_a^2}{2} + \frac{(C_1 + C_3) \hat{q}_b^2}{2} + \frac{C_3 (\hat{q}_a - \hat{q}_b)^2}{2} \right] \\
& + \frac{\hat{\Phi}_a^2}{2L_1} + \frac{\hat{\Phi}_b^2}{2L_2} + \frac{(\hat{\Phi}_a - \hat{\Phi}_b)^2}{2L_3}
\end{aligned}
\tag{A.19}
$$

The procedure highlighted so far is completely general for non-dissipative systems. Summing up, it consists in writing the Lagrangian in terms of the flux nodes by subtracting the magnetic energy to the electrostatic energy, then Legendre transforming to a classical Hamiltonian and quantizing via canonical quantization. It can be applied also in the presence non-linear elements such as Josephson junctions, i.e. non-linear inductors whose magnetic energy is given by Eq.(2.2).

Appendix B

Magnus Expansion and Average Hamiltonian Theory

We consider a time-dependent Hamiltonian $H(t)$. Our goal is to find an effective Hamiltonian $\tilde{H}(t)$ capturing the dynamics on a coarse grained scale, defined by the small but finite time interval Δt. To this end we write

$$U(t + \Delta t; t) = \mathcal{T} e^{-i \int_t^{t+\Delta t} dt' H(t')} = \prod_{k=1}^{\overleftarrow{n}} e^{-i H_k \, \delta t_k} \qquad \text{(B.1)}$$

where we consider $n \to \infty$ time slices δt_k with $\sum_{k=1}^n \delta t_k = \Delta t$ and define $H_k := H(t_k)$ with t_k belonging to the k-th time slice. Moreover $\mathcal{T}$ is the time-ordering operator for the continuous case, while the arrow stands for time-ordering in the discretized one. By repeated application of the Campbell-Baker-Hausdorff relation

$$e^A e^B = \exp\{A + B + \frac{1}{2}[A, B] + ...\} \qquad \text{(B.2)}$$

we can write $U(t + \Delta t; t) = e^{-i \tilde{H}_{\Delta t}(t) \Delta t}$, where $\tilde{H}_{\Delta t}(t)$ is given up to second order by

$$\tilde{H}_{\Delta t}(t) = \frac{1}{\Delta t} \int_t^{t+\Delta t} dt' H(t') - \frac{i}{2\Delta t} \int_t^{t+\Delta t} dt' \int_t^{t'} dt'' [H(t'), H(t'')] \qquad \text{(B.3)}$$

In many cases this expression can be approximated by a Δt independent one, i.e. $\tilde{H}_{\Delta t}(t) \simeq \tilde{H}(t)$. The resulting averaged $U(t + \Delta t; t) = e^{-i \tilde{H}(t) \Delta t}$ allows to approximate $U(t, t_0) \approx \mathcal{T} e^{-i \int_{t_0}^t dt' \tilde{H}(t')}$. In this way, $\tilde{H}(t)$ is identified as an effective Hamiltonian capturing the dynamics in a coarse grained fashion, which is the main result of *average Hamiltonian theory*.

We now refer explicitly to the problem of finding the effective Hamiltonians of Eqs.(5.4) and (5.9). We carried out calculations in the interaction picture defined by H_0 [see Eq.(5.1)]. In our case each component of the pump pulse is far detuned from each transition, allowing us to take $\Delta t \delta_{ij}^k \gg 1$, where $\delta_{ij}^k :=$ $|\omega_{ij} - \omega_{pk}|$. Since $\Omega_r, |\dot{\phi}_{pk'}(t)|, 1/T \ll \delta_{ij}^k$, we are allowed to choose Δt such that $\Delta t/T, \Delta t\Omega_r, \Delta t|\dot{\phi}_{p2,s}(t)| \ll 1$. Then the effective Hamiltonians Eqs. (5.4) and (5.9) are obtained from Eq. (B.3) by bringing out of the integrals all the slowly varying terms and subsequently neglecting terms of order $(\delta_{ij}^k \Delta t)^{-1}$ or higher, so that Δt will not appear in $\tilde{H}$. The physical quantities that this procedure yields are Stark shifts in the diagonal elements and amplitudes for two-photon processes in the off-diagonal elements of $\tilde{H}$.

Appendix C

2+1 STIRAP with an always-on pump coupling

In chapter 4 we studied a technique tailored to circuit-QED architectures, were hardware limitations impose the non modulability of the coupling. In chapter 5, on the other hand, we saw how a 2+1-photon version of conventional STIRAP can be employed with artificial atoms biased at symmetry points with almost unit efficiency. While in chapter 5 we made use of gaussian pulses [see Fig.5.1(b)], in this appendix we briefly show how a good transfer efficiency can be achieved by employing an always-on field as one of the two fields composing the two-photon pump. This has obvious applications to circuit-QED architectures with the resonator dispersively coupled to the artificial atom.

We will, thereby, employ a gaussian shaped Ω_{p1} and an always-on Ω_{p2}. We will, then, consider a gaussian Ω_s as in chapter 5 and use the phase-modulation of Eq.(5.5). For simplicity, we will only consider the anharmonic case of the flux qudit, where the three-level approximation is possible. We plot the result in Fig.C.1(b), while in Fig.C.1(a) we give the results for the gaussian pulses for comparison.

We notice that, while the effective Hamiltonian Eq.(5.3) is invariant if we change $p1 \leftrightarrow p2$, protocols with always-on Ω_{p1} are less faithful, since the constant field produces small Rabi oscillations between $|0\rangle$ and $|1\rangle$ at the beginning of the protocol, when $|0\rangle$ is populated. Instead the always-on Ω_{p1} scheme works better for the time-reversed protocol.
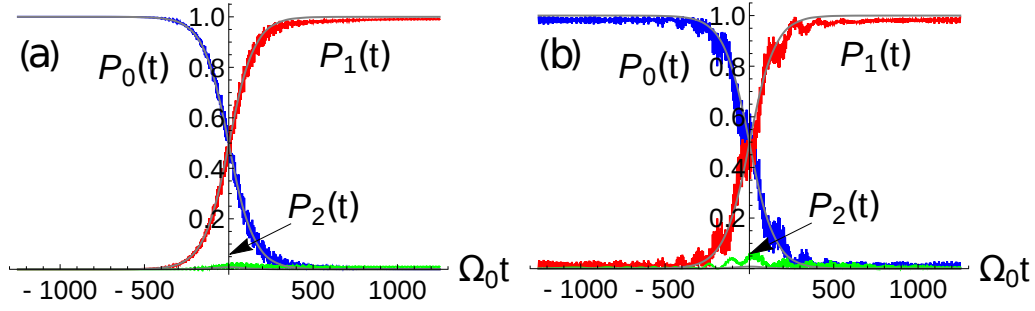
Figure C.1: (a) Populations histories vs $\Omega_0 t$ of the 2+1 STIRAP protocol (coloured lines), for always-on Ω_{p2}. Gray lines are the populations of the effective Hamiltonian Eq. (5.4), capturing very well the coarse-grained dynamics. Here $\text{Max}[\Omega_{s,p}(t)]T = 50$ (b) The protocol with always-on Ω_{p1} with the same figures, proves to be less faithful.

Bibliography

[1] G. Ithier, E. Collin, P. Joyez, P. Meeson, D. Vion, D. Esteve, F. Chiarello, A. Shnirman, Y. Makhlin, J. Schriefl, and G. Schön. Decoherence in a superconducting quantum bit circuit. *Phys. Rev. B*, 72:134519, 2005.

[2] J. Bylander, S. Gustavsson, F. Yan, F. Yoshihara, K. Harrabi, G. Fitch, D.G. Cory, Y. Nakamura, J.-S. Tsai, and W.D. Oliver. Noise spectroscopy through dynamical decoupling with a superconducting flux qubit. *Nature Phys.*, 7:565–570, 2011.

[3] C. Rigetti, J.M. Gambetta, S. Poletto, B. L. T. Plourde, J. M. Chow, A. D. Córcoles, J. A. Smolin, S. T. Merkel, J. R. Rozen, G. A. Keefe, M. B. Rothwell, M. B. Ketchen, and M. Steffen. Superconducting qubit in a waveguide cavity with a coherence time approaching 0.1 ms. *Phys. Rev. B*, 86:100506, 2012.

[4] T. Niemczyk, F. Deppe, H. Huebl, F. Menzel, E.P.and Hocke, M.J. Schwarz, J.J. Garcia-Ripoll, D. Zueco, T. Hümmer, E. Solano, A. Marx, and R. Gross. Circuit quantum electrodynamics in the ultrastrong-coupling regime. *Nature Phys.*, 6:772–776, 2010.

[5] C. Neill, P. Roushan, M. Fang, Y. Chen, M. Kolodrubetz, Z. Chen, A. Megrant, R. Barends, B. Campbell, B. Chiaro, A. Dunsworth, E. Jeffrey, J. Kelly, J. Mutus, P. J. J. O'Malley, C. Quintana, D. Sank, A. Vainsencher, J. Wenner, T. C. White, A. Polkovnikov, and J. M. Martinis. Ergodic dynamics and thermalization in an isolated quantum system. *Nature Phys.*, 12:1037–1041, 2016. Letter.

[6] S. Sheldon, E. Magesan, J. M. Chow, and J. M. Gambetta. Procedure for systematically tuning up cross-talk in the cross-resonance gate. *Phys. Rev. A*, 93:060302, 2016.

[7] J. M. Chow, J. M. Gambetta, A. W. Cross, S. T, Merkel, C. Rigetti, and M. Steffen. Microwave-activated conditional-phase gate for superconducting qubits. *New J. Phys.*, 15:115012, 2013.

[8] S. Poletto, J. M. Gambetta, S. T. Merkel, J. A. Smolin, J. M. Chow, A. D. Córcoles, G. A. Keefe, Mary B. Rothwell, J. R. Rozen, D. W. Abraham, C. Rigetti, and M. Steffen. Entanglement of two superconducting qubits in a waveguide cavity via monochromatic two-photon excitation. *Phys. Rev. Lett.*, 109:240505, 2012.

[9] See, for example, https://www.gov.uk/government/uploads/system/uploads/attachment_data/file/470243/InnovateUK_QuantumTech_CO004_final.pdf

[10] D. Deutsch. Quantum theory, the Church-Turing principle and the universal quantum computer. *Proceedings of the Royal Society of London A: Mathematical, Physical and Engineering Sciences*, 400:97–117, 1985.

[11] P. W. Shor. Polynomial-time algorithms for prime factorization and discrete logarithms on a quantum computer. *SIAM J. Comput.*, 26:1484–1509, 1997.

[12] Lov K. Grover. A fast quantum mechanical algorithm for database search. In *Proceedings of the Twenty-eighth Annual ACM Symposium on Theory of Computing STOC '96* (ACM New York), p. 212–219, 1996.

[13] P. Rebentrost, M. Mohseni, and S. Lloyd. Quantum support vector machine for big data classification. *Phys. Rev. Lett.*, 113:130503, 2014.

[14] S. Lloyd, M. Mohseni, and P. Rebentrost. Quantum principal component analysis. *Nature Phys.*, 10:631–633, 2014.

[15] D. Risté, M. P. da Silva, C. A. Ryan, A. W. Cross, J. A. Smolin, J. M. Gambetta, J. M. Chow, and B R. Johnson. Demonstration of quantum advantage in machine learning, *arXiv:1512.06069*.

[16] R. P. Feynman. Simulating physics with computers. *Int. J. Theor. Phys.*, 21:467–488, 1982.

[17] S. Lloyd. Universal quantum simulators. *Science*, 273:1073–1078, 1996.

[18] R. Babbush, P. J. Love, and A. Aspuru-Guzik. Adiabatic quantum simulation of quantum chemistry. *Sci. Rep.*, 4:6603, Oct 2014.

[19] J. Roßnagel, O. Abah, F. Schmidt-Kaler, K. Singer, and E. Lutz. Nanoscale heat engine beyond the Carnot limit. *Phys. Rev. Lett.*, 112:030602, Jan 2014.

[20] E. Torrontegui, S. Ibáñez, S. Martínez-Garaot, M. Modugno, A. del Campo, D. Guéry-Odelin, A. Ruschhaupt, Xi Chen, and J. G. Muga. Shortcuts to adiabaticity. *Adv. in At. Mol. and Opt. Phys.*, 62:117–169, 2013.

[21] A. del Campo, J. Goold, and M. Paternostro. More bang for your buck: Super-adiabatic quantum engines. *Sci. Rep.*, 4:6208, 2014.

[22] V. Giovannetti, S. Lloyd, and L. Maccone. Advances in quantum metrology. *Nat. Photon.*, 5:222–229, 2011.

[23] W. H. Zurek. Decoherence, einselection, and the quantum origins of the classical. *Rev. Mod. Phys.*, 75:715–775, 2003.

[24] J. M. Raimond, M. Brune, and S. Haroche. Manipulating quantum entanglement with atoms and photons in a cavity. *Rev. Mod. Phys.*, 73:565–582, 2001.

[25] J. I. Cirac and P. Zoller. Quantum computations with cold trapped ions. *Phys. Rev. Lett.*, 74:4091–4094, 1995.

[26] D. Loss and D. P. DiVincenzo. Quantum computation with quantum dots. *Phys. Rev. A*, 57:120–126, 1998.

[27] Jonathan A. Jones. Quantum computing with NMR. *Prog. Nucl. Magn. Reson. Spectrosc.*, 59:91–120, 2011.

[28] J. R. Weber, W. F. Koehl, J. B. Varley, A. Janotti, B. B. Buckley, C. G. Van de Walle, and D. D. Awschalom. Quantum computing with defects. *Proceedings of the National Academy of Sciences*, 107:8513–8518, 2010.

[29] B. E. Kane. A silicon-based nuclear spin quantum computer. *Nature*, 393:133–137, 1998.

[30] A. Blais, R.-S. Huang, A. Wallraff, S. M. Girvin, and R. J. Schoelkopf. Cavity quantum electrodynamics for superconducting electrical circuits: An architecture for quantum computation. *Phys. Rev. A*, 69:062320, 2004.

[31] M.H. Devoret, A. Wallraff, and J.N. Martinis. Superconducting qubits: a short review. *arXiv:cond-mat/0411174*.

[32] Y. Makhlin, G. Schön, and A. Shnirman. Quantum-state engineering with josephson-junction devices. *Rev. Mod. Phys.*, 73:357–400, 2001.

[33] Y. Nakamura, Yu. A. Pashkin, and J. S. Tsai. Coherent control of macroscopic quantum states in a single-cooper-pair box. *Nature*, 398:786–788, 1999.

[34] N. Roch, M. E. Schwartz, F. Motzoi, C. Macklin, R. Vijay, A. W. Eddins, A. N. Korotkov, K. B. Whaley, M. Sarovar, and I. Siddiqi. Observation of measurement-induced entanglement and quantum trajectories of remote superconducting qubits. *Phys. Rev. Lett.*, 112:170501, 2014.

[35] T. Brecht, W. Pfaff, C. Wang, Y. Chu, L. Frunzio, M. H. Devoret, and R. J. Schoelkopf. Multilayer microwave integrated quantum circuits for scalable quantum computing. *Npj Quantum Information*, 2:16002, 2016.

[36] F. Plastina and G. Falci. Communicating josephson qubits. *Phys. Rev. B*, 67:224514, 2003.

[37] A. A. Houck, H. E. Tureci, and J. Koch. On-chip quantum simulation with superconducting circuits. *Nat. Phys.*, 8:292–299, 2012.

[38] H. T. Quan, Y. D. Wang, Yu-xi Liu, C. P. Sun, and F. Nori. Maxwell's demon assisted thermodynamic cycle in superconducting quantum circuits. *Phys. Rev. Lett.*, 97:180402, 2006.

[39] B. Vlastakis, G. Kirchmair, Z. Leghtas, S. E. Nigg, L. Frunzio, S. M. Girvin, M. Mirrahimi, M. H. Devoret, and R. J. Schoelkopf. Deterministically encoding quantum information using 100-photon schrödinger cat states. *Science*, 342:607–610, 2013.

[40] R. Barends, J. Kelly, A. Megrant, A. Veitia, D. Sank, E. Jeffrey, T. C. White, J. Mutus, A. G. Fowler, B. Campbell, Y. Chen, Z. Chen, B. Chiaro, A. Dunsworth, C. Neill, P. O/'Malley, P. Roushan, A. Vainsencher, J. Wenner, A. N. Korotkov, A. N. Cleland, and John M. Martinis. Superconducting quantum circuits at the surface code threshold for fault tolerance. *Nature*, 508(7497):500–503, 2014.

[41] A. Yu. Kitaev. *Quantum Error Correction with Imperfect Gates*, pages 181–188. Springer US, Boston, MA, 1997.

[42] J. Kelly, R. Barends, A. G. Fowler, A. Megrant, E. Jeffrey, T. C. White, D. Sank, J. Y. Mutus, B. Campbell, Yu Chen, Z. Chen, B. Chiaro, A. Dunsworth, I.-C. Hoi, C. Neill, P. J. J. O/'Malley, C. Quintana, P. Roushan, A. Vainsencher, J. Wenner, A. N. Cleland, and John M. Martinis. State preservation by repetitive error detection in a superconducting quantum circuit. *Nature*, 519:66–69, 2015.

[43] E. Paladino, Y.M. Galperin, G. Falci, and B.L. Altshuler. $1/f$ noise: implications for solid-state quantum information. *Rev. Mod. Phys.*, 86:361–418, 2014.

[44] G. Falci, A. D'Arrigo A. Mastellone, and E. Paladino. Low-frequency noise characterization in charge-based coherent nanodevices. *Open Sys. and Inf. Dyn.*, 13:323–332, 2006.

[45] G. Falci, A. D'Arrigo, A. Mastellone, and E. Paladino. Initial decoherence in solid state qubits. *Phys. Rev. Lett.*, 94:167002, 2005.

[46] E. Paladino, L. Faoro, G. Falci, and R. Fazio. Decoherence and $1/f$ noise in josephson qubits. *Phys. Rev. Lett.*, 88:228304, 2002.

[47] K. Bergmann, H. Theuer, and B.W. Shore. Coherent population transfer among quantum states of atoms and molecules. *Rev. Mod. Phys.*, 70:1003–1025, 1998.

[48] G. Falci, A. La Cognata, M. Berritta, A. D'Arrigo, E. Paladino, and B. Spagnolo. Design of a lambda system for population transfer in superconducting nanocircuits. *Phys. Rev. B*, 87:214515, Jun 2013.

[49] M. Mücke, J. Bochmann, C. Hahn, A. Neuzner, C. Nölleke, A. Reiserer, G. Rempe, and S. Ritter. Generation of single photons from an atom-cavity system. *Phys. Rev. A*, 87:063805, 2013.

[50] T. Wilk, S. C. Webster, A. Kuhn, and G. Rempe. Single-atom single-photon quantum interface. *Science*, 317:488–490, 2007.

[51] C.-P. Yang, S.-I Chu, and S. Han. Quantum information transfer and entanglement with squid qubits in cavity qed: A dark-state scheme with tolerance for nonuniform device parameter. *Phys. Rev. Lett.*, 92:117902, 2004.

[52] D. Möller, L. B. Madsen, and K. Mölmer. Quantum gates and multiparticle entanglement by Rydberg excitation blockade and adiabatic passage. *Phys. Rev. Lett.*, 100:170504, 2008.

[53] K. Bergmann, N. V. Vitanov, and B. W. Shore. Perspective: Stimulated raman adiabatic passage: The status after 25 years. *Jour. Chem. Phys.*, 142:170901, 2015.

[54] N.V. Vitanov, M. Fleischhauer, B.W. Shore, and K. Bergmann. Coherent manipulation of atoms and molecules by sequential laser pulses. *Adv. in At. Mol. and Opt. Phys.*, 46:55–190, 2001.

[55] J. Siewert, T. Brandes, and G. Falci. Advanced control with a cooper-pair box: Stimulated raman adiabatic passage and fock-state generation in a nanomechanical resonator. *Phys. Rev. B*, 79:024504, 2009.

[56] J. Siewert, T. Brandes, and G. Falci. Adiabatic passage with superconducting nanocircuits. *Opt. Commun.*, 264:435 – 440, 2006.

[57] G. Falci, P.G. Di Stefano, A. Ridolfo, A. D'Arrigo, G.S. Paraoanu, E. Paladino, Advanced control of superconducting architectures in the Lambda scheme, *Fortschr. Phys.*, 10.1002/prop201600077.

[58] M. Pechal, L. Huthmacher, C. Eichler, S. Zeytinoğlu, A. A. Abdumalikov, S. Berger, A. Wallraff, and S. Filipp. Microwave-controlled generation of shaped single photons in circuit quantum electrodynamics. *Phys. Rev. X*, 4:041010, 2014.

[59] J. Goold, M. Huber, A. Riera, L. del Rio, and P. Skrzypczyk. The role of quantum information in thermodynamics—a topical review. *J. Phys. A*, 49:143001, 2016.

[60] J. Millen and A. Xuereb. Perspective on quantum thermodynamics. *New J. Phys.*, 18(1):011002, 2016.

[61] M. Campisi and P. Hänggi. Fluctuation, dissipation and the arrow of time. *Entropy*, 13:2024, 2011.

[62] J. Eisert, M. Friesdorf, and C. Gogolin. Quantum many-body systems out of equilibrium. *Nature Phys.*, 11:124–130, 2015.

[63] O. Abah, J. Roßnagel, G. Jacob, S. Deffner, F. Schmidt-Kaler, K. Singer, and E. Lutz. Single-ion heat engine at maximum power. *Phys. Rev. Lett.*, 109:203006, 2012.

[64] U. Seifert. Stochastic thermodynamics, fluctuation theorems and molecular machines. *Rep. Prog. Phys.*, 75:126001, 2012.

[65] P. Campisi, P. Hänggi, and P. Talkner. *Colloquium* : Quantum fluctuation relations: Foundations and applications. *Rev. Mod. Phys.*, 83:771–791, 2011.

[66] M. Esposito, U. Harbola, and S. Mukamel. Nonequilibrium fluctuations, fluctuation theorems, and counting statistics in quantum systems. *Rev. Mod. Phys.*, 81:1665–1702, 2009.

[67] G. E. Crooks. Entropy production fluctuation theorem and the nonequilibrium work relation for free energy differences. *Phys. Rev. E*, 60:2721–2726, 1999.

[68] G. Watanabe, B. P. Venkatesh, P. Talkner, M. Campisi, and Peter Hänggi. Quantum fluctuation theorems and generalized measurements during the force protocol. *Phys. Rev. E*, 89:1–8, 2014.

[69] G. Manzano, J. M. Horowitz, and J. M. R. Parrondo. Nonequilibrium potential and fluctuation theorems for quantum maps. *Phys. Rev. E*, 92:032129, 2015.

[70] Sebastian Deffner and Eric Lutz. Nonequilibrium entropy production for open quantum systems. *Phys. Rev. Lett.*, 107:140404, Sep 2011.

[71] T. B. Batalhão, A. M. Souza, R. S. Sarthour, I. S. Oliveira, M. Paternostro, E. Lutz, and R. M. Serra. Irreversibility and the arrow of time in a quenched quantum system. *Phys. Rev. Lett.*, 115:190601, 2015.

[72] U. Vool and M. H. Devoret. Introduction to quantum electromagnetic circuits, *arXiv:1610.03438*.

[73] J.J. Sakurai. *Modern quantum mechanics*. Addison Wesley, 1993.

[74] J. Koch, T. Yu, J. Gambetta, A. Houck, D. Schuster, J. Majer, Alexandre Blais, M. Devoret, S. Girvin, and R. Schoelkopf. Charge-insensitive qubit design derived from the cooper pair box. *Phys. Rev. A*, 76, 2007.

[75] M. Devoret and R. J. Schoelkopf. Superconducting circuits for quantum information: An outlook. *Science*, 339:1169, 2013.

[76] T. P. Orlando, J. E. Mooij, L. Tian, C. H. van der Wal, L. S. Levitov, S. Lloyd, and J. J. Mazo. Superconducting persistent-current qubit. *Phys. Rev. B*, 60:15398–15413, 1999.

[77] C.H. van der Wal, A.C.J. ter Haar, F.K. Wilhelm, R.N. Schouten, C.J.P.M. Harmans, T.P. Orlando, S. Lloyd, and J.E. Mooij. Quantum superposition of macroscopic persistent-current states. *Science*, 290:773–777, 2000.

[78] M. Stern, G. Catelani, Y. Kubo, C. Grezes, A. Bienfait, D. Vion, D. Esteve, and P. Bertet. Flux qubits with long coherence times for hybrid quantum circuits. *Phys. Rev. Lett.*, 113:123601, 2014.

[79] L. DiCarlo, J. M. Chow, J. M. Gambetta, Lev S. Bishop, B. R. Johnson, D. I. Schuster, J. Majer, A. Blais, L. Frunzio, S. M. Girvin, and R. J. Schoelkopf. Demonstration of two-qubit algorithms with a superconducting quantum processor. *Nature*, 460:240–244, 2009.

[80] L. F. Wei, J. R. Johansson, L. X. Cen, S. Ashhab, and Franco Nori. Controllable coherent population transfers in superconducting qubits for quantum computing. *Phys. Rev. Lett.*, 100:113601, 2008.

[81] Z. Kis and E. Paspalakis. Arbitrary rotation and entanglement of flux squid qubits. *Phys. Rev. B*, 69:024510, 2004.

[82] S. Haroche and J. M. Raimond. *Exploring the Quantum: Atoms, Cavities, and Photons.* Oxford Univ. Press, 2006.

[83] A.N. Korotkov. Quantum Bayesian approach to circuit QED measurement. *arXiv:1111.4016*.

[84] H.-P. Breuer and F. Petruccione. *The theory of open quantum systems.* Oxford Univ. Press, 2007.

[85] Claude Cohen-Tannoudji, Jacques Dupont-Roc, and Gilbert Gryndberg. *Atom-Photon Interactions: Basic Processes and Applications.* Wiley, 1998.

[86] E. Geva, R. Kosloff, and J. L. Skinner. On the relaxation of a 2-level system driven by a strong electromagnetic field. *J. Chem. Phys.*, 102:8541–8561, 1995.

[87] H. M. Wiseman and G. J. Milburn. *Quantum Measurement and Control.* Cambridge Univ. Press, 2014.

[88] H. M. Wiseman and G. J. Milburn. Quantum theory of field-quadrature measurements. *Phys. Rev. A*, 47:642–662, 1993.

[89] J. Gambetta, A. Blais, M. Boissonneault, A. A. Houck, D. I. Schuster, and S. M. Girvin. Quantum trajectory approach to circuit qed: Quantum jumps and the zeno effect. *Phys. Rev. A*, 77:012112, 2008.

[90] M. A. Nielsen and I. L. Chuang. *Quantum Computation and Quantum Information: 10th Anniversary Edition.* Cambridge Univ. Press, 2011.

[91] A.N. Korotkov. Selective quantum evolution of a qubit state due to continuous measurement. *Phys. Rev. B*, 63:1–15, 2001.

[92] M. A. Sillanpää, J. Li, K. Cicak, F. Altomare, J. I. Park, R. W. Simmonds, G. S. Paraoanu, and P. J. Hakonen. Autler-Townes effect in a superconducting three-level system. *Phys. Rev. Lett.*, 103:193601, 2009.

[93] J. Li, G.S. Paraoanu, K. Cicak, F. Altomare, J.I. Park, R.W. Simmonds, M.A. Sillanpää, and P.J. Hakonen. Dynamical Autler-Townes control of a phase qubit. *Sci. Rep.*, 2:645, 2012.

[94] A. A. Abdumalikov, O. Astafiev, A. M. Zagoskin, Yu. A. Pashkin, Y. Nakamura, and J. S. Tsai. Electromagnetically induced transparency on a single artificial atom. *Phys. Rev. Lett.*, 104:193601, 2010.

[95] R. Bianchetti, S. Filipp, M. Baur, J. M. Fink, C. Lang, L. Steffen, M. Boissonneault, A. Blais, and A. Wallraff. Control and tomography of a three level superconducting artificial atom. *Phys. Rev. Lett.*, 105:223601, 2010.

[96] W. R. Kelly, Z. Dutton, J. Schlafer, B. Mookerji, T. A. Ohki, J. S. Kline, and D. P. Pappas. Direct observation of coherent population trapping in a superconducting artificial atom. *Phys. Rev. Lett.*, 104:163601, 2010.

[97] A. Kuhn, M. Hennrich, T. Bondo, and G. Rempe. Controlled generation of single photons from a strongly coupled atom-cavity system. *Appl. Phys. B*, 69:373–377, 1999.

[98] Yu-xi Liu, J. Q. You, L. F. Wei, C. P. Sun, and Franco Nori. Optical selection rules and phase-dependent adiabatic state control in a superconducting quantum circuit. *Phys. Rev. Lett.*, 95:087001, 2005.

[99] G. Falci, M. Berritta, A. Russo, A. D'Arrigo, and E. Paladino. Effects of low-frequency noise in driven coherent nanodevices. *Phys. Scr.*, 2012:1402–4896, 2012.

[100] J. Q. You and Franco Nori. Atomic physics and quantum optics using superconducting circuits. *Nature*, 474:589 – 597, 2011.

[101] N. V. Vitanov, B. W. Shore T. Halfmann, and K. Bergmann. Laser-induced population transfer by adiabatic passage techniques. *Annu. Rev. Phys. Chem.*, 52:763, 2001.

[102] T. Duty, D. Gunnarsson, K. Bladh, and P. Delsing. Coherent dynamics of a josephson charge qubit. *Phys. Rev. B*, 69:140503, 2004.

[103] D. Vion, A. Aassime, A. Cottet, P. Joyez, H. Pothier, C. Urbina, D. Esteve, and M. H. Devoret. Manipulating the quantum state of an electrical circuit. *Science*, 296:886–889, 2002.

[104] A. Wallraff, D. I. Schuster, A. Blais, L. Frunzio, R. S. Huang, J. Majer, S. Kumar, S. M. Girvin, and R. J. Schoelkopf. Strong coupling of a single photon to a superconducting qubit using circuit quantum electrodynamics. *Nature*, 421:162–167, 2004.

[105] F. Charello, E. Paladino, M. G. Castellano, C. Cosmelli, A. D'Arrigo, G. Torrioli, and G. Falci. Superconducting qubit manipulated by fast pulses: experimental observation of distinct decoherence regimes. *New J. Phys.*, 14:023031, 2012.

[106] E. Paladino, A. D'Arrigo, A. Mastellone, and G. Falci. Decoherence times of universal two-qubit gates in the presence of broad-band noise. *New J. Phys.*, 13:1367–2630, 2011.

[107] E. Paladino, A. Mastellone, A. D'Arrigo, and G. Falci. Optimal tuning of solid-state quantum gates: A universal two-qubit gate. *Phys. Rev. B*, 81:052502, 2010.

[108] R. Lo Franco, A. D'Arrigo, G. Falci, G. Compagno, and E. Paladino. Entanglement dynamics in superconducting qubits affected by local bistable impurities. *Phys. Scr.*, 2012:1402–4896, 2012.

[109] R. Lo Franco, A. D'Arrigo, G. Falci, G. Compagno, and E. Paladino. Preserving entanglement and nonlocality in solid-state qubits by dynamical decoupling. *Phys. Rev. B*, 90:054304, 2014.

[110] P. A. Ivanov, N.V. Vitanov, and K. Bergmann. Effect of dephasing on stimulated Raman adiabatic passage. *Phys. Rev. A*, 70:063409, 2004.

[111] A. Kuhn, M. Hennrich, and G. Rempe. Deterministic single-photon source for distributed quantum networking. *Phys. Rev. Lett.*, 89:067901, 2002.

[112] J. Klein, F. Beil, and T. Halfmann. Experimental investigations of stimulated raman adiabatic passage in a doped solid. *Phys. Rev. A*, 78:033416, 2008.

[113] K. V. R. M. Murali, Z. Dutton, W. D. Oliver, D. S. Crankshaw, and T. P. Orlando. Probing decoherence with electromagnetically induced transparency in superconductive quantum circuits. *Phys. Rev. Lett.*, 93:087003, Aug 2004.

[114] M. Baur, S. Filipp, R. Bianchetti, J. M. Fink, M. Göppl, L. Steffen, P. J. Leek, A. Blais, and A. Wallraff. Measurement of Autler-Townes and Mollow transitions in a strongly driven superconducting qubit. *Phys. Rev. Lett.*, 102(24):243602, Jun 2009.

[115] C. Cohen-Tannoudji. Dark resonances from optical pumping to cold atoms and molecules. *Kosmos, revue de la Société Suédoise de Physique*, 2009.

[116] I. R. Solá, V. S. Malinovsky, Bo Y. Chang, J. Santamaria, and K. Bergmann. Coherent population transfer in three-level λ systems by chirped laser pulses: Minimization of the intermediate-level population. *Phys. Rev. A*, 59:4494–4501, 1999.

[117] P. G. Di Stefano, E. Paladino, A. D'Arrigo, B. Spagnolo, and G. Falci. Design of a lambda configuration in artificial coherent nanostructures. *Rom. J. Phys.*, 60:676–685, 2015.

[118] R. J. Schoelkopf and S. M. Girvin. Wiring up quantum systems. *Nature*, 451:664, 2008.

[119] Y. Nakamura and T. Yamamoto. Breakthroughs in photonics 2012: Breakthroughs in microwave quantum photonics in superconducting circuits. *IEEE Photon. J.*, 5:2, 2013.

[120] P. Král, I. Thanopulos, and M. Shapiro. Colloquium: Coherently controlled adiabatic passage. *Rev. Mod. Phys.*, 79:53–77, 2007.

[121] N. Timoney, I. Baumgart, M. Johanning, A. F. Varon, M. B. Plenio, A. Retzker, and Ch. Wunderlich. Quantum gates and memory using microwave-dressed states. *Nature*, 476:185–U83, 2011.

[122] B. P. Lanyon, M. Barbieri, M. P. Almeida, T. Jennewein, T. C. Ralph, K. J. Resch, G. J. Pryde, A. O'Brien, J. L. Gilchrist, and A. G. White. Simplifying quantum logic using higher-dimensional hilbert spaces. *Nature Phys.*, 5:124–140, 2009.

[123] J.K. Pachos. *Introduction to Topological Quantum Computation.* Cambridge Univ. Press, 2012.

[124] H.J. Kimble. The quantum internet. *Nature*, 453:1023–1030, 2008.

[125] A. D'Arrigo, R. Lo Franco, G. Benenti, E. Paladino, and G. Falci. Recovering entanglement by local operations. *Ann. Phys.*, 350:211–224, 2014.

[126] A. Orieux, A: D'Arrigo, G. Ferranti, R. Lo Franco, G. Benenti, E. Paladino, G: Falci, F. Sciarrino, and P. Mataloni. Experimental on-demand recovery of entanglement by local operations within non-markovian dynamics. *Sci. Rep.*, 5:8575, 2015.

[127] T. D. Ladd, F. Jelezko, R. Laflamme, Y. Nakamura, C. Monroe, and J. L. O'Brien. Quantum computers. *Nature*, 464:08812, 2010.

[128] P. Macha, G. Oelsner, J.-M. Reiner, M. Marthaler, S. A., G. Sch on, U. Hübner, H.-G. Meyer, E. Il'ichev, and A. V. Ustinov. Implementation of a quantum metamaterial using superconducting qubits. *Nature Commun.*, 5:5146, Oct 2014.

[129] H. R. Mohebbi, O. W. B. Benningshof, I. A. J. Taminiau, G. X. Miao, and D. G. Cory. Composite arrays of superconducting microstrip line resonators. *Jour. Appl. Phys.*, 115:094502, 2014.

[130] M. Mariantoni, M. J. Storcz, F. K. Wilhelm, W. D. Oliver, A. Emmert, A. Marx, R. Gross, H. Christ, and E. Solano. On-chip microwave fock states and quantum homodyne measurements. *arXiv:cond-mat/0509737v2.*

[131] P. G. Di Stefano, E. Paladino, A. D'Arrigo, and G. Falci. Population transfer in a lambda system induced by detunings. *Phys. Rev. B*, 91:224506, 2015.

[132] Z.-L. Xiang, S. Ashhab, J.Q. You, and F. Nori. Hybrid quantum circuits: Superconducting circuits interacting with other quantum systems. *Rev. Mod. Phys.*, 85:623, 2013.

[133] L. P. Yatsenko, S. Guérin, T. Halfmann, K. Böhmer, B. W. Shore, and K. Bergmann. Stimulated hyper-Raman adiabatic passage. i. the basic problem and examples. *Phys. Rev. A*, 58:4683–4690, 1998.

[134] S. Guérin, L. P. Yatsenko, T. Halfmann, B. W. Shore, and K. Bergmann. Stimulated hyper-raman adiabatic passage. ii. static compensation of dynamic stark shifts. *Phys. Rev. A*, 58:4691–4704, 1998.

[135] K. Böhmer, T. Halfmann, L. P. Yatsenko, B. W. Shore, and K. Bergmann. Stimulated hyper-raman adiabatic passage. iii. experiment. *Phys. Rev. A*, 64:023404, 2001.

[136] J. S. Waugh, L. M. Huber, and U. Haeberlen. Approach to high-resolution NMR in solids. *Phys. Rev. Lett.*, 20:180–182, 1968.

[137] A. Wallraff, D. I. Schuster, A. Blais, L. Frunzio, R.-S. Huang, J. Majer, S. Kumar, S. M. Girvin, and R. J. Schoelkopf. Strong coupling of a single photon to a superconducting qubit using circuit quantum electrodynamics. *Nature*, 431:162–167, 2004.

[138] K.S. Kumar, A. Vepsäläinen, S. Danilin, and G.S. Paraoanu. Stimulated Raman adiabatic passage in a three-level superconducting circuit. *Nature Commun.*, 7:10628, 2016.

[139] H. K. Xu, C. Song, W. Y. Liu, G. M. Xue, F. F. Su, H. Deng, Ye Tian, D. N. Zheng, Siyuan Han, Y. P. Zhong, H. Wang, Yu-xi Liu, and S. P. Zhao. Coherent population transfer between uncoupled or weakly coupled states in ladder-type superconducting qutrits. *Nature Commun.*, 7:11018, 2016.

[140] R. Stassi, A. Ridolfo, O. Di Stefano, M. J. Hartmann, and S. Savasta. Spontaneous conversion from virtual to real photons in the ultrastrong-coupling regime. *Phys. Rev. Lett.*, 110:243601, 2013.

[141] Jin-Feng Huang and C. K. Law. Photon emission via vacuum-dressed intermediate states under ultrastrong coupling. *Phys. Rev. A*, 89:033827, 2014.

[142] S. Haroche and J.-M. Raimond. *Exploring the Quantum.* Oxford Univ. press, 2006.

[143] C. Ciuti, G. Bastard, and I. Carusotto. Quantum vacuum properties of the intersubband cavity polariton field. *Phys. Rev. B*, 72:115303, 2005.

[144] A. A. Anappara, S. De Liberato, A. Tredicucci, C. Ciuti, G. Biasiol, L. Sorba, and F. Beltram. Signatures of the ultrastrong light-matter coupling regime. *Phys. Rev. B*, 79:201303, 2009.

[145] P. Forn-Díaz, J. Lisenfeld, D. Marcos, J. J. García-Ripoll, E. Solano, C. J. P. M. Harmans, and J. E. Mooij. Observation of the Bloch-Siegert shift in a qubit-oscillator system in the ultrastrong coupling regime. *Phys. Rev. Lett.*, 105:237001, 2010.

[146] P. Forn-Díaz, J.J. García-Ripoll, B. Peropadre, M.A. Yurtalan, J.-L. Orgiazzi, R. Belyansky, C.M. Wilson, and A. Lupascu. Ultrastrong coupling of a single artificial atom to an electromagnetic continuum in the nonperturbative regime *Nature Phys.*, 2016. doi:10.1038/nphys3905.

[147] F. Yoshihara, T. Fuse, K. Kakuyanagi, S. Saito, and K. Semba. Superconducting qubit–oscillator circuit beyond the ultrastrong-coupling regime *Nature Phys.*, advance online publication, 2016. doi:10.1038/nphys3906.

[148] G. Günter, A. A. Anappara, J. Hees, G. Sell, G. Biasiol, L. Sorba, S. De Liberato, C. Ciuti, A. Tredicucci, A. Leitenstorfer, and R Huber. Sub-cycle switch-on of ultrastrong light–matter interaction. *Nature*, 458:178–181, 2009.

[149] G. Scalari, C. Maissen, D. Turcinkova, D. Hagenmüller, S. De Liberato, C. Ciuti, C. Reichl, D. Schuh, W. Wegscheider, M. Beck, and J. Faist. Ultrastrong coupling of the cyclotron transition of a 2d electron gas to a thz metamaterial. *Science*, 335:1323–1326, 2012.

[150] S. De Liberato, C. Ciuti, and I. Carusotto. Quantum vacuum radiation spectra from a semiconductor microcavity with a time-modulated vacuum rabi frequency. *Phys. Rev. Lett.*, 98:103602, 2007.

[151] S. Ashhab and F. Nori. Qubit-oscillator systems in the ultrastrong-coupling regime and their potential for preparing nonclassical states. *Phys. Rev. A*, 81:042311, 2010.

[152] R. H. Dicke. Coherence in spontaneous radiation processes. *Phys. Rev.*, 93:99–110, 1954.

[153] P. G. Di Stefano, E. Paladino, T. J. Pope, and G. Falci. Coherent manipulation of noise-protected superconducting artificial atoms in the lambda scheme. *Phys. Rev. A*, 93:051801, 2016.

[154] A. Ridolfo, M. Leib, S. Savasta, and M. J. Hartmann. Photon blockade in the ultrastrong coupling regime. *Phys. Rev. Lett.*, 109:193602, 2012.

[155] M. J. Peterer, S. J. Bader, X. Jin, F. Yan, A. Kamal, T. J. Gudmundsen, P. J. Leek, T. P. Orlando, W. D. Oliver, and S. Gustavsson. Coherence and decay of higher energy levels of a superconducting transmon qubit. *Phys. Rev. Lett.*, 114:010501, 2015.

[156] Christopher Jarzynski. Equalities and inequalities: Irreversibility and the second law of thermodynamics at the nanoscale. *Annu. Rev. Condens. Matter Phys.*, 2:329–351, 2011.

[157] J. J. Alonso, E. Lutz, and A. Romito. Thermodynamics of Weakly Measured Quantum Systems. *Phys. Rev. Lett.*, 116:080403, 2016.

[158] P. Talkner, E. Lutz, and P. Hänggi. Fluctuation theorems: Work is not an observable. *Phys. Rev. E*, 75:050102, 2007.

[159] K. W. Murch, S. J. Weber, C. Macklin, and I. Siddiqi. Observing single quantum trajectories of a superconducting quantum bit. *Nature*, 502:211–214, 2013.

[160] R. Vijay, C. Macklin, D. H. Slichter, S. J. Weber, K. W. Murch, R. Naik, A. N. Korotkov, and I. Siddiqi. Stabilizing rabi oscillations in a superconducting qubit using quantum feedback. *Nature*, 490:77–80, 2012.

[161] M. Hatridge, S. Shankar, M. Mirrahimi, F. Schackert, K. Geerlings, T. Brecht, K. M. Sliwa, B. Abdo, L. Frunzio, S. M. Girvin, R. J. Schoelkopf, and M. H. Devoret. Quantum back-action of an individual variable-strength measurement. *Science*, 339:178–181, 2013.

[162] R. Vijay, D. H. Slichter, and I. Siddiqi. Observation of quantum jumps in a superconducting artificial atom. *Phys. Rev. Lett.*, 106:110502, 2011.

[163] W. Feng, P. Liang, L. Qin, and X.-Q. Li. Exact quantum bayesian rule for qubit measurements in circuit qed. *Sci. Rep.*, 6:20492, 2016.

[164] M. H. Devoret. in *Quantum fluctuations (Les Houches Session LXIII)*. Edited by S. Reynaud, E. Giscobino and J. Zinn-Justin, 1997.

[165] C.A. Desoer and E.S. Kuh. *Basic circuit theory*. McGraw-Hill, 1969.

[166] C. Elouard, D. Herrera-Martí, M. Clusel and A. Auffèves The role of quantum measurement in stochastic thermodynamics, *arXiv:1607.02404.*